

**X-ray Telescope Foil Optics:
Assembly, Metrology, and Constraint**

by

Craig Richard Forest

B.S., Mechanical Engineering, Georgia Institute of Technology (2001)

Submitted to the Department of Mechanical Engineering
in partial fulfillment of the requirements for the degree of

Master of Science in Mechanical Engineering

at the

MASSACHUSETTS INSTITUTE OF TECHNOLOGY

May 2003

© Massachusetts Institute of Technology 2003. All rights reserved.

Author
Department of Mechanical Engineering
May 9, 2003

Certified by
Mark L. Schattenburg
Principal Research Scientist
Thesis Supervisor

Certified by
Alexander H. Slocum
Professor, Mechanical Engineering
Thesis Supervisor

Accepted by
Ain A. Sonin
Chairman, Department Committee on Graduate Students

X-ray Telescope Foil Optics: Assembly, Metrology, and Constraint

by

Craig Richard Forest

Submitted to the Department of Mechanical Engineering
on May 9, 2003, in partial fulfillment of the
requirements for the degree of
Master of Science in Mechanical Engineering

Abstract

This thesis will describe progress made at the MIT *Space Nanotechnology Laboratory* towards the realization of the NASA *Constellation-X* mission. This x-ray telescope mission, with its design incorporating thin segmented foil optics, presents many mechanical engineering challenges. The assembly, measurement, and technique for holding these thin, floppy optics have been investigated. Not only is this work applicable to the manufacture and assembly of the optics for an x-ray telescope, metrology and assembly of thin, transparent optics is a current challenge in the manufacture of flat panel displays, photomasks in the semiconductor industry, and glass substrates for computer hard disks.

The assembly of optic foils to one millionth of a meter accuracy and repeatability is demonstrated. The tool used to accomplish this task reinforces previous proof-of-concept data and makes great strides towards proving mass production assembly technology for space flight modules containing tens of optic foils.

A Shack-Hartmann metrology tool has been designed and built to study the shape of these thin foils. This deep-ultraviolet (deep-UV) optical instrument has an angular resolution of $0.5 \mu\text{rad}$, angular dynamic range of $350 \mu\text{rad}$, and view area of $142 \times 142 \text{ mm}^2$. The deep-UV wavelengths are particularly useful for studying transparent substrates such as glass which are virtually opaque to wavelengths below 260 nm.

Theoretical studies examine thin foil deformation due to external disturbances such as gravity, friction, vibration, and thermal expansion. This work has led to the design of a device with two rotational and two translational degrees of freedom which can kinematically hold the foils for accurate and repeatable metrology.

Thesis Supervisor: Mark L. Schattenburg
Title: Principal Research Scientist

Thesis Supervisor: Alexander H. Slocum
Title: Professor, Mechanical Engineering

Acknowledgments

I would like to generously thank the many people and organizations that have assisted and supported this research. My co-advisors, Mark Schattenburg and Alex Slocum, have been absolutely essential to the success of this work. From early-morning creative brainstorming sessions to endless manuscript revisions, these individuals have provided unflagging support.

I am grateful for the support of the students, staff, and facilities from the MIT *Space Nanotechnology Laboratory*. The assistance of Yanxia Sun, Mireille Akilian, Paul Konkola, Carl Chen, Juan Montoya, Ralf Heilmann, Michael McGuirk, Chulmin Joo, Glen Monnelly, Nat Butler, and Chih-Hao Chang is much appreciated. Important contributions to this thesis were provided by undergraduates Guillaume Vincent, JoHanna Przybylowski, and Alexandre Lamure as well. I would also like to thank Ed Murphy and Bob Fleming for their generous assistance on many occasions.

The assembly truss segment of research would not have been possible without team members Matthew Spenko and Yanxia Sun. Weekly feedback from the Fall 2001 MIT Precision Machine Design class including instructors Alex Slocum and Martin Culpepper is gratefully acknowledged. Developing the Shack-Hartmann metrology system involved many people including, from Wavefront Sciences, Daniel Neal, Craig Armstead, Ron Rammage, and Jim Roller. From MIT, generous assistance was received from Michael McGuirk and George Barbastathis. Other key industry contributions came from Patrick Moschitto (Schott), Bob Scannel (SORL), Ken McKay (TMC), Ryan Renner (OptoSigma), and Kevin Lian (Lambda Research Optics).

On a more personal note, Laura Major has provided everything from a butt-kicking to a hug to get me through the obstacles and celebrate the successes. My parents' support of my educational endeavors has always been vital to their initiation and completion.

Financial support for this work was provided by NASA Grants NAG5-5271 and NCC5-633 and the National Science Foundation Graduate Research Fellowship Program.

Contents

1	Introduction	25
1.1	Segmented foil optics	26
1.2	Current work	28
1.3	Thin optic applications in other fields	32
2	Foil optic assembly truss	35
2.1	Functional requirements	35
2.2	Optic foils	36
2.3	Previous assembly research	38
2.3.1	Assembly procedure	38
2.3.2	Microcombs	40
2.3.3	First-generation assembly truss	43
2.4	Design process	50
2.5	From conceptual designs to selection	52
2.5.1	Error budget theory	52
2.5.2	Preliminary error budgets	57
2.5.3	Cost/performance analysis	65
2.6	Final design	67
2.6.1	Reference flat	67
2.6.2	Kinematic couplings	68
2.6.3	Flight module	68
2.6.4	Flexure bearing assembly	69
2.7	Microcomb contact with reference flat, experimental	80

2.8	Repeatability testing	83
2.9	Accuracy testing	86
2.10	Final error budget	89
2.11	Discussion and conclusions	90
3	Shack-Hartmann surface metrology system	93
3.1	Introduction	94
3.1.1	Metrology technology candidates, research review	95
3.1.2	Justification for Shack-Hartmann technology selection	101
3.2	System design overview	102
3.3	Detailed design	104
3.3.1	Arc lamp	104
3.3.2	Spectral filter	105
3.3.3	Spatial filter	109
3.3.4	Beam splitter	110
3.3.5	Laser source discussion	112
3.3.6	Power considerations	113
3.3.7	Wavefront sensor	115
3.4	Performance evaluation	122
3.4.1	Test optic surface mapping	122
3.4.2	Repeatability and accuracy	125
3.5	Conclusions	126
4	Deformation and constraint of thin optics	129
4.1	Environmental concerns	130
4.1.1	Gravity sag	130
4.1.2	Vibration	136
4.1.3	Thermal considerations	137
4.2	Mounting effects	140
4.2.1	Constraint locations	140
4.2.2	Friction	142

4.3	Foil optic fixture design	144
4.3.1	Functional requirements	144
4.3.2	Design	146
4.4	Conclusions	147
A	Assembly truss angle-to-linear displacement conversion	149
A.1	Derivation	149
B	Conceptual designs for the assembly truss	153
C	Assembly truss error budgets	161
C.1	Preliminary error budgets for stack and air-bearing concepts	161
C.2	Final design error budget	164
D	Force sensor calibration curves	171

List of Figures

1-1	The Chandra x-ray telescope optic configuration consists of hyperbolic and parabolic shaped optics to focus the incoming radiation. These monolithic optics are heavy and expensive to manufacture.	26
1-2	Thin foil coated with gold, as in those used for the Astro-E telescope mission.	27
1-3	A quadrant composed of 168 nested foil mirrors. The radial bars are oriented perpendicularly to the foils, holding them in place.	27
1-4	The arrangement of the Astro-E telescope. The diameter of the cylinder is 40 cm and the mass is 40 kg.	28
1-5	Packing configurations for x-ray imaging systems. As the x-rays approach the telescope, they “see” the optics from this perspective. A segment of the Kirkpatrick-Baez (K-B) design can be duplicated and densely packed for more collecting area.	29
1-6	Model of a K-B optic flight module. An additional module would focus the cross axis to give the grid appearance in Figure 1-5c. Each holds 30 parabolic and 30 hyperbolic foils; only 6 are shown.	30
1-7	Reflection gratings disperse the x-rays into their constituent wavelengths for spectroscopy analysis.	30
2-1	Warp is measured by placing the glass on a flat table without external mechanical constraints. S-shaped glass does not meet quality control specifications if dimensions a and $b > \text{warp tolerance}/2$. Warp tolerance is $600 \mu\text{m}$ for a $400 \mu\text{m}$ thick foil. (Schott Glas)	37

2-2	Model of the silicon foil used for experimentation with assembly truss.	38
2-3	Assembly procedure. Foils are first held loosely in the flight module. The flight module is then inserted into the precision assembly truss. The foils are aligned and bonded to the flight module. The assembly truss is removed and reused to align the foils in another flight module.	39
2-4	Foils are forced into alignment by the spring microcombs against the reference microcombs. The reference microcombs are registered against the reference flat surface.	40
2-5	Side view of microcombs installed in the assembly tooling (<i>left</i>) and a dummy foil pinched in between them (<i>right</i>).	41
2-6	Scanning electron microscope (SEM) images of silicon spring (<i>left</i>) and reference (<i>right</i>) microcomb teeth.	41
2-7	The spring comb design ensures that foils of varying thickness can all be pushed up against the reference comb teeth.	42
2-8	Reference and spring microcomb dimensions used for previous assembly research.	43
2-9	First-generation of the assembly truss technology utilizing the microcomb design for foil alignment. A single flat plate is installed (<i>left</i>). Close up of the spring and reference comb constraining the aligned foil (<i>right</i>).	44
2-10	The parts of the first-generation assembly truss are assembled in an open structural loop to facilitate metrology of the optics. The reference flat and microcombs establish the metrology frame. The microcombs' function is illustrated with an optic foil (<i>inset</i>).	45
2-11	The autocollimator provides measurement of the angles ϕ_A or ϕ_B . These angles represent the deviation from zero in pitch only (yaw reading also gathered) from the planar reference flat if the autocollimator is zeroed from the flat. Drift of the autocollimator reading with time must be accounted for as well.	46

2-12	Design Process chart. The functional requirements, strategies, physics, risks, and countermeasures are also shown. Highlighted rows indicate selected design routes. The physics concerns were too broad to cite specific references.	51
2-13	The Pugh chart qualitatively identifies concept strengths and weaknesses. From this chart, the (1) vertical air-bearing design and (2) stack design were pursued further.	52
2-14	The stack design (<i>left</i>) and the vertical air-bearing design (<i>right</i>). The reference frame, CS_R , is located at the center of the reference flat. Coordinate system CS_1 is located at the interface between the microcomb and the reference flat. Coordinate system CS_2 is at the interface between the microcomb tooth and optic foil. In the preliminary error budget, we will consider the structural loop from the reference frame to CS_2 for both concepts.	53
2-15	Details of the stack concept are shown. This notation will be used in the error budget calculations.	58
2-16	Schematic of original reference comb (<i>left</i>) and redesigned comb (<i>right</i>). The error in the position of the comb's tooth is a function of its non-perpendicularity to the reference flat. In the original design, the comb's contact point with the flat is not aligned with the foil contact point in the direction of the comb's axis. The separation between these lines of contact is magnified by $\sin \theta_X$. This term vanishes when the separation equals zero in the redesigned comb.	65
2-17	The redesigned microcomb eliminates Abbe error. The comb/flat contact point (location of CS_1) is collinear with the comb/foil contact point (location of CS_2). Compare this reference comb's dimensions with the previous generation of reference comb in Figure 2-8 on page 43.	65

2-18	The cost/performance schematic illustrates that the theoretical marginal performance improvement for the air-bearing concept may not be worth the additional cost as compared to the stack design. The cost grows exponentially as the desired random error approaches zero; part tolerances during manufacture would drive this behavior.	66
2-19	Foil optic assembly truss. The flight module is not inside of the assembly tool for this picture. Tests on this assembly truss were performed with only three comb sets instead of six as manufactured. Six will be necessary to distort a cylindrical foil into parabolic or hyperbolic shapes, but only three are necessary to locate a plane.	67
2-20	The reference flat is shown in relation to the assembly truss.	68
2-21	The kinematic coupling ball and vee-block components are shown. These were located at nine distinct locations on the truss to repeatably orient the reference flat, cover, and flight module.	69
2-22	Flight module containing optic foils is shown. This prototype module is designed to hold thirty foils and fit into the assembly truss.	70
2-23	Cross-section view of an optic foil being glued to a coarse comb. This procedure is performed inside the assembly truss after the foils are in their aligned positions.	70
2-24	The flexure bearing assembly contains microcombs, flexure bearings, force sensors, and micrometers.	71
2-25	The mathematical model for the flexure bearing assembly. Before contact with the reference flat occurs, $k_{\text{hertz}} = 0$. After contact, this term is non-zero and not constant with force.	72
2-26	Separating the flexure bearing model into two parts permits the evaluation of the transmission ratio between the micrometer displacement, x_1 , and the microcomb displacement, x_2	74
2-27	The modeled stiffnesses for the two flexure bearing designs before and after contact with the reference flat. The slope after contact is slightly non-linear due to the Hertzian contact stiffness.	78

2-28	Assembly truss during testing with reflective optic foil inserted. The microcomb is in contact with the reference flat (<i>inset</i>).	80
2-29	Experimental data from flexure bearing assembly design 1 (<i>left</i>) and design 2 (<i>right</i>). In both designs, contact with the reference flat is observable. The second design, with its lower stiffness reference flexure, has a more dramatic change in slope.	81
2-30	Differential force data reveals the force at the comb/flat interface. Fracture occurs when the Hertzian shear stress in the comb exceeds the silicon shear strength.	82
2-31	Following the comb damage test, magnification clearly reveals the fractured surface at the comb nose.	83
2-32	Repeatability testing procedure. A single foil is slid from the side of the assembly truss into the microcomb slot. The reference microcombs are then driven into contact with the reference flat. Angles of the optic are recorded. The combs are then retracted, and the assembly truss lid is raised and replaced.	85
2-33	Accuracy testing schematic. $d = 55$ mm, $H = 140$ mm.	86
2-34	Top view of assembly truss showing how the systematic error in yaw, θ_s , is related to the microcomb lengths, L_1 , L_2 , and the measured yaw error of the foil, θ_{m1}	87
2-35	Side view of assembly truss showing how the systematic error in pitch, ϕ_s , is related to the microcomb lengths, L_1 , L_2 , L_3 , and the measured pitch error of the foil, ϕ_{m1}	89
3-1	Shack-Hartmann wavefront sensing concept.	101
3-2	Shack-Hartmann surface metrology system.	102
3-3	Portion of the Shack-Hartmann metrology system illustrating the intrinsic Keplarian design.	103
3-4	Optical properties of 0.4 mm thick borosilicate glass (Schott Glas, model D-263).	106

3-5	Path of light reflected from front and back surfaces of glass into sensor. Back reflections (<i>dashed line</i>) should be avoided.	106
3-6	Transmission curves for a range of spectral filters (Acton Research, Omega Optical)	107
3-7	Irradiance reflected from glass sheets into wavefront sensor as a function of wavelength for the 254 nm wideband filter. This simulation considers the arc lamp spectral output, spectral filter transmission, optical properties of the borosilicate glass, and lumogen coating on the CCD.	108
3-8	Beam splitter diagram showing transmitted beam T , reflected beam R , and the transmitted/reflected $T \cdot R$ beam to the sensor.	111
3-9	Power losses throughout the optical path of the Shack-Hartmann surface metrology system.	113
3-10	The sinc ² focal spot is shown overlaid with the pixels apportioned to a lenslet inside the Shack-Hartmann wavefront sensor.	116
3-11	The large tilt of the incident wavefront results in a focal spot shift to the edge of the lenslet's area-of-interest (AOI). This is the extent of the instrument's angular range.	120
3-12	Shack-Hartmann metrology system hardware in a class 1000 cleanroom environment at the MIT <i>Space Nanotechnology Laboratory</i>	123
3-13	Raw data (<i>left</i>) is collected on the CCD array in the wavefront sensor. Comparison with a reference image enables the wavefront reconstruction (<i>right</i>), which is equivalent to a surface map at the object plane. The intensity scale (<i>center</i>) indicates the relative energy density incident on the pixels in $2^{12} = 4096$ discrete values.	124
3-14	Measurement of a single silicon wafer twice before bonding (erect and inverted) and twice after bonding.	124
3-15	RMS angular deviation from flatness of a 100 mm diameter reference flat is shown. Running average of successive discrete wavefront measurements shows the mitigation of random error.	125

4-1	Optic foil coordinate system and 2-D beam bending model. In the beam bending model, the boundary conditions are pin joints.	130
4-2	The pin joint constraint (<i>a</i>) allows rotation about the <i>x</i> -axis only, and no translation of the joint. The ball-socket triad (<i>b</i>) permits rotation about all three axes, and no translation.	133
4-3	Maximum deformation of the glass foil as a function of pitch angle. Dimensions: $140 \times 100 \times 0.4 \text{ mm}^3$, Boundary conditions: ball-socket triad.	134
4-4	Maximum deformation of the glass foil as a function of thickness. Dimensions: $140 \times 100 \times t \text{ mm}^3$, Boundary conditions: ball-socket triad. Angle of inclination: 0.82°	135
4-5	Acoustics measurements of the environment inside the MIT <i>Space Nanotechnology Laboratory</i>	136
4-6	Thermal expansion mismatch causes the foil holder clamps to separate by $15 \mu\text{m}$ more than the foil length increases. This reduces the perceived warp if the boundary conditions do not allow slip (<i>left</i>). The circle geometry is used to calculate this reduction in warp (<i>right</i>). . .	139
4-7	Deformation of the glass foil decreases as the number of constraint locations increases. The deformation asymptotically approaches $0.37 \mu\text{m}$ and $1.87 \mu\text{m}$ for the non-rotating and rotating boundary conditions, respectively, as the number of contact points goes to infinity (pin joints). Dimensions: $140 \times 100 \times 0.4 \text{ mm}^3$, Angle of inclination: 0.82°	141
4-8	The actuation force of the spring comb combined with the friction force at the bottom of the foil can lead to distortion. Using pin joints and a 2-D beam bending analysis, we can estimate the magnitude.	142
4-9	Analytical result for foil deformation due to friction.	143
4-10	The foil holder allows two rotational and two translational degrees of freedom for the optic foil. The visible face of the foil can be mapped by a metrology tool.	146

A-1	The foil is shown with definitions to be used in the angle-to-displacement conversion derivation.	150
B-1	Initial concepts illustrating some techniques for meeting the functional requirements for the design. The glass foil is shown as a transparent rectangle. The microcombs are depicted as gray bars. Design (a) was eliminated since the relatively large deformation of the thin foils due to gravity sag would be unacceptable. This problem of gravity deformation is explored in more detail in Chapter 4. Kinematic balls sketched in (b-d) permit repeatable assembly of the truss. Design (c) unnecessarily restricted user access to the microcombs. Design (e) is different from (f) in that the reference surface is not a structural member and is instead mounted kinematically to the vertical support.	154
B-2	In the “stack” concept, the flight module would be placed into the truss and the lid would be set on top. Kinematic couplings (not shown) at critical interfaces would ensure repeatable assembly. Gravity deflection of the lid and deformations of the reference flat were concerns.	155
B-3	The fixed truss concept would involve sliding the flight module down into a rigid truss on guide ways, rails, or by hand. A critical shortcoming in this design is part interference. Microcomb teeth may fracture during assembly.	156
B-4	In the “L-truss,” an air bearing table allows the flight module to be slid into place followed by the remaining half of the truss. Complexity and repeatability were key concerns.	157
B-5	The fixed reference flat acts as a surface from which the flight module and microcomb embedded walls are aligned. The flight module would be repeatably placed on kinematic couplings. Air bearings could provide a frictionless surface for sliding the walls with microcombs attached.	158

B-6	The vertical air bearing concept repeatably places the microcombs with respect to the reference flat. The microcombs are glued to the carriages, which can then translate vertically or be locked in place with a vacuum preload on the bearings.	159
B-7	An initial model of the flight module is shown from the side and top perspectives. Three optic foils are shown inserted. The flight module must allow measurement during assembly and permit the entrance and exit of x-rays during flight. Relatively low tolerances can be used since the assembly tool will do the high-accuracy alignment and the foils will then be fixed into place with an adhesive.	160
C-1	Preliminary error budget for the stack concept. The average sum and RSS random errors are $1.9 \mu\text{m}$ and the net total systematic errors are $0.3 \mu\text{m}$	162
C-2	Preliminary error budget for the air-bearing concept. The average sum and RSS random errors are $1.8 \mu\text{m}$ and the net total systematic errors are $0.0 \mu\text{m}$	163
C-3	Side view of the final assembly truss design with coordinate systems for error budgeting labeled. As before, the reference coordinate system is at the center of the reference flat face, CS_1 is located at the comb/flat interface, and CS_2 is located at the contact point between the reference comb and the optic foil.	165
C-4	Final error budget for the assembly truss. The average sum and RSS random errors are $0.5 \mu\text{m}$ and the net total systematic errors are $0.3 \mu\text{m}$	169
D-1	Force sensor calibration data is shown along with sensor photographs. Linear regression fits were performed for each sensor to extract the proportionality value. Statistically, the high R^2 values indicate that the proportionality value is constant over the range.	172

List of Tables

2.1	Properties of materials for thin foil optics with aluminum as a reference.	37
2.2	Derived values for Young's modulus for Si.	37
2.3	First-generation assembly truss alignment results.	48
2.4	Random translational and angular errors in the stack concept CS_1 . .	60
2.5	Random translational and angular errors in the stack concept CS_2 . .	62
2.6	Preliminary error budget results for random and systematic error contributions in the stack and vertical air-bearing concepts. The errors shown are in the sensitive Y direction only; errors in the non-sensitive directions are available in Appendix C.	64
2.7	Mathematical expression for the error contribution in the sensitive Y direction from the microcomb pitch along with the overall Y direction error.	64
2.8	Dimensions for the two manufactured flexure bearing assemblies and calculated stiffnesses.	77
2.9	The transmission ratio, x_2/x_1 , is shown for the two flexure bearing designs before and after microcomb contact with the reference flat. .	79
2.10	Stiffness measurements from flexure bearing assembly design 1 and 2 are compared with theory.	81
2.11	Assembly truss single slot repeatability results. Displacement error is the displacement of the edge of the foil extracted from its angular error and dimensions.	85

2.12	For the three slots tested, the comb lengths were calculated. These lengths represent the distances from the reference flat/comb contact points to the foil/comb tooth contact points. Only relative lengths can be calculated.	88
2.13	Assembly truss slot accuracy results. Displacement error is the displacement of the edge of the foil extracted from its angular error and dimensions. The errors for three successive slots are shown along with the average systematic angular errors.	90
2.14	Final error budget for assembly truss design. Errors shown are in the sensitive Y direction only; errors in the non-sensitive directions are available in Appendix C.	90
3.1	Comparison of spectral filters for Shack-Hartmann metrology system. The total power from the front reflection returned to the sensor is shown along with the ratio of the power from the front and back reflection, named the focal spot intensity ratio.	108
3.2	Optical element transmission (T) and reflection (R) percentages from spatial filter to CCD detector. The items are listed in the order that the light “sees” them. Repeated items are “seen” twice. High transmission percentages are due to anti-reflection coatings.	115
3.3	Wavefront sensor quantum efficiency test data.	118
3.4	Wavefront sensor lenslet array, detector and system magnification summary.	119
3.5	Shack-Hartmann surface metrology system performance results. . . .	126
4.1	Deformation at foil centerline for three materials at pitch = 90° (perpendicular to gravity) and pitch = 0.82° (nearly aligned with gravity). Dimensions: $140 \times 100 \times 0.4$ mm ³ , Boundary conditions: pin joints. . .	131
4.2	Heat sources in the MIT <i>Space Nanotechnology Laboratory</i> metrology room.	138

4.3	Linear thermal expansion of 140 mm long foil substrates and aluminum fixture in response to 7°C (12.6°F) environment temperature change.	138
4.4	Foil holder performance for four degrees of freedom.	147
C.1	Random translational errors in the final assembly truss CS_1 . Multiple error sources have been root-sum-squared to get the random error contribution.	166
C.2	Random angular errors in the final assembly truss CS_1 . Multiple error sources have been root-sum-squared to get the random error contribution.	167
C.3	Random translational and angular errors in the final assembly truss CS_2 . Multiple error sources have been root-sum-squared to get the random error contribution.	168

Chapter 1

Introduction

X-ray astronomy has enabled the study of fundamental physics of the universe in ways not possible through the study of visible light. This regime reveals a universe of explosive objects, extreme temperatures, intense gravitational fields, and rapid time variations. Mongrard [1] has detailed the history of amazing achievements in x-ray astronomy.

Strong absorption of x-ray radiation by both the Earth's atmosphere and optical materials severely limits the location and design of x-ray imaging systems. X-ray astronomy is conducted using telescopes located in space since more than 50% of the incident radiation at 10 keV, for example, is absorbed after traveling only 1.3 m through the atmosphere [2]. In the design of these telescopes, refractive imaging is limited to very thin lenses, on the order of a few microns, since the x-rays are absorbed so strongly. These physical limitations have given rise to a class of grazing-incidence telescopes, in which nearly lossless imaging is achieved by bouncing the incoming radiation off multiple mirrored surfaces at shallow angles. At angles less than 4° , x-rays reflecting from vacuum to a high density material can be reflected with efficiencies near 100% [2].

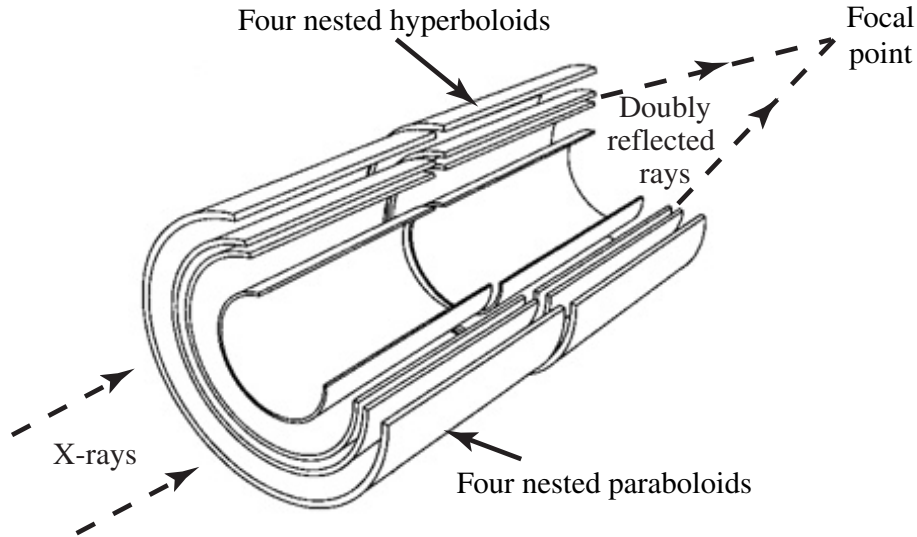


Figure 1-1: The Chandra x-ray telescope optic configuration consists of hyperbolic and parabolic shaped optics to focus the incoming radiation. These monolithic optics are heavy and expensive to manufacture.

1.1 Segmented foil optics

Figure 1-1 shows Chandra, the highest resolution x-ray telescope. The multiple mirrors shown are used to reflect incoming x-rays to a focus to form a picture of the galaxy, supernova, or other object of interest. The x-rays first hit the nested set of paraboloids at shallow angles, then the nested set of hyperboloids, and lastly travel to a focal point. Traditionally, the grazing-incidence mirrors for x-ray imaging are made from monolithic substrates which are carved and meticulously polished from huge blocks of Zerodur, a low thermal expansion glass ceramic. These optics are heavy, very expensive to manufacture, and the size of the telescope is limited by the launch vehicle capability.

These problems can be avoided by using segmented foil optics. This alternative to the monolithic structure offers less weight, larger collecting area, and lower cost to manufacture. In this approach, thin foils coated with a smooth layer of high density material are densely packed into modular units for assembly. A single foil for the Astro-E telescope mission is shown Figure 1-2. The foils are assembled into quadrants as shown in Figure 1-3. Four quadrants are then assembled to form a cylinder in Figure 1-4.

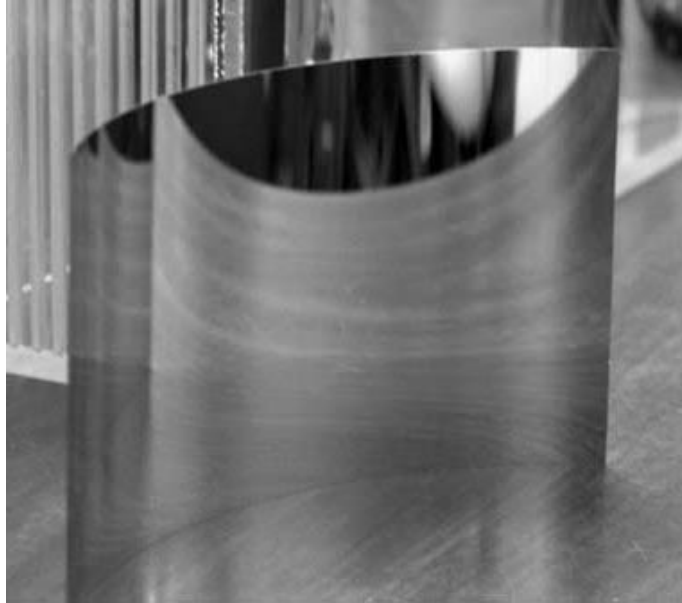


Figure 1-2: Thin foil coated with gold, as in those used for the Astro-E telescope mission.



Figure 1-3: A quadrant composed of 168 nested foil mirrors. The radial bars are oriented perpendicularly to the foils, holding them in place.

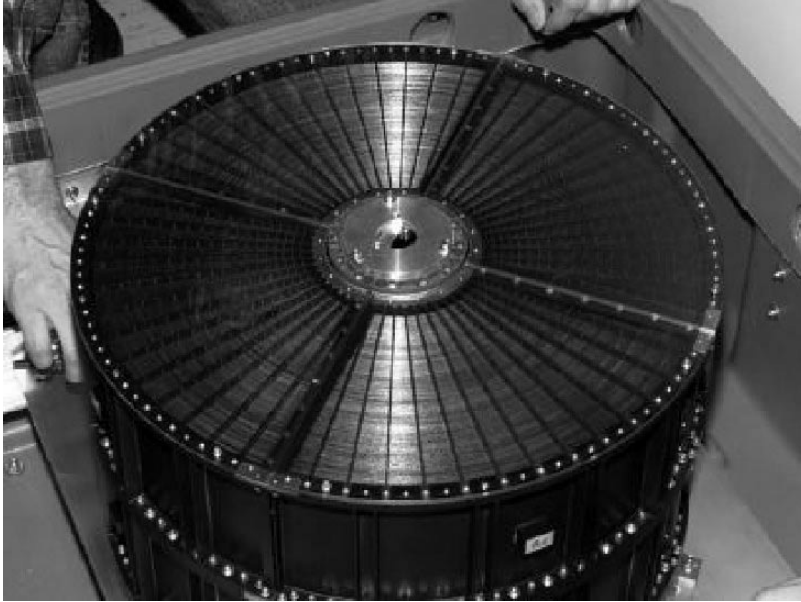


Figure 1-4: The arrangement of the Astro-E telescope. The diameter of the cylinder is 40 cm and the mass is 40 kg.

The engineering tradeoff with this design approach, however, is its limited resolution. Of the three previous foil optic missions, Astro-E has the finest resolution at $\simeq 1.5$ arcmin. This resolution is limited by foil figure errors¹ and foil assembly errors. As a result, the segmented foil optic design requires relaxation of the 0.5 arcsec Chandra angular resolution achievement. Despite this drawback, the development of high throughput telescopes with good angular resolution for deep surveys, and for spectroscopy and variability studies of faint sources and of extended objects having low surface brightness is the future of x-ray astronomy [3, 4].

1.2 Current work

Four segmented foil *Spectroscopy X-ray Telescopes* (SXT) on the NASA *Constellation-X* mission are being developed to enable large collecting area ($>15,000$ cm² at 1 keV, 6,000 cm² at 6.4 keV) with moderate angular resolution (<15 arcsec at 6.4 keV). This mission will require sub-micron accurate and repeatable assembly of thousands

¹The foil shape is a slice through a cone due to the challenges of manufacturing hyperbolic and parabolic shapes into thin foils.

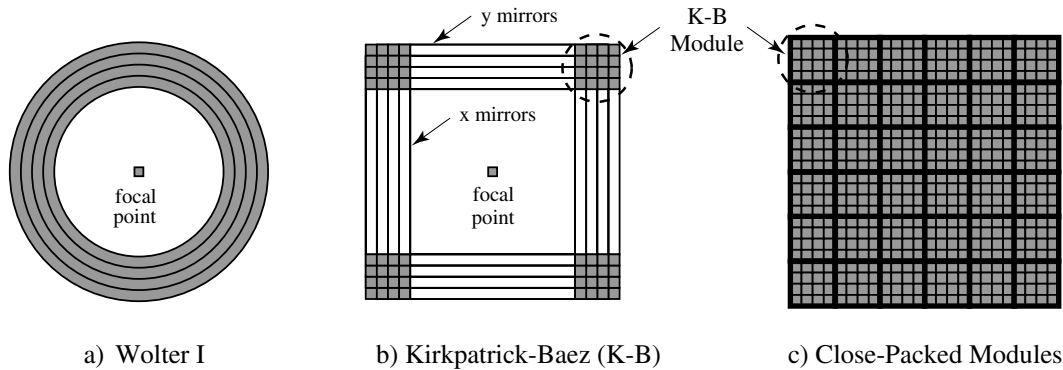


Figure 1-5: Packing configurations for x-ray imaging systems. As the x-rays approach the telescope, they “see” the optics from this perspective. A segment of the Kirkpatrick-Baez (K-B) design can be duplicated and densely packed for more collecting area.

of individual foils. In addition to the sub-micron assembly tolerances, individual foils must be manufactured with figure errors less than 500 nm over their $140 \times 100 \text{ mm}^2$ surface area.

Foil optics, as the focusing elements in an x-ray telescope, could be implemented in a number of configurations. Figure 1-5 shows the Wolter I arrangement as used on the *X-ray Multi-Mirror* (XMM) mission along with the Kirkpatrick and Baez (K-B) implementation. The Chandra telescope, shown in Figure 1-1, uses this Wolter I configuration with monolithic optics. The K-B setup offers the advantage of densely packing a set of rectangular modules, thus greatly increasing the collecting area. A single K-B flight module is depicted in Figure 1-6.

In addition to focusing incoming x-ray radiation, foil optics packed into these flight modules can be used as reflection gratings for spectroscopy, in which different incoming wavelengths are focused to different locations. Figure 1-7 shows the role of the reflection gratings after the primary optics. The proposed *Reflection Grating Spectrometer* (RGS) on the *Constellation-X* mission is designed to provide high-resolution x-ray spectroscopy of astrophysical sources. Two types of reflection grating geometries have been proposed for the RGS. In-plane gratings have relatively low-density rulings (~ 500 lines/mm) with lines perpendicular to the plane of incidence, thus dispersing x-rays into the plane. This geometry is similar to the reflec-

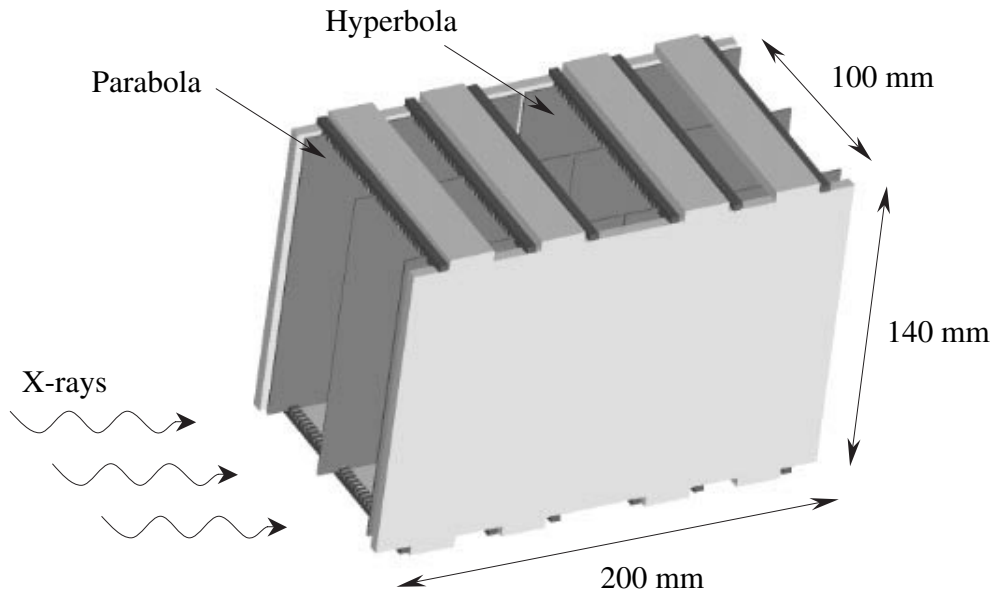


Figure 1-6: Model of a K-B optic flight module. An additional module would focus the cross axis to give the grid appearance in Figure 1-5c. Each holds 30 parabolic and 30 hyperbolic foils; only 6 are shown.

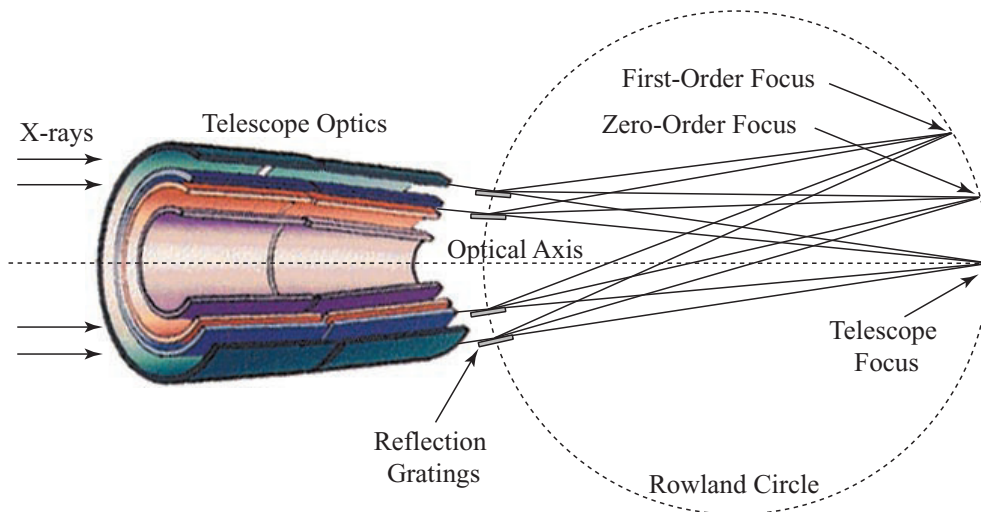


Figure 1-7: Reflection gratings disperse the x-rays into their constituent wavelengths for spectroscopy analysis.

tion grating spectrometer flown on the XMM mission. Off-plane, or conical, gratings require much higher density rulings (>5000 lines/mm) with lines parallel to the plane of incidence, thus dispersing x-rays perpendicular to the plane. Both types present unique challenges and advantages and are under intensive development [5, 6]. In both cases, however, grating flatness and assembly tolerances are driven by the mission's high spectral resolution goals and the relatively poor resolution of the Wolter I foil optics of the SXT that are used in conjunction with the RGS. In general, to achieve high spectral resolution, both geometries require lightweight grating substrates with arcsecond flatness and assembly tolerances. This implies sub-micron accuracy and precision which go well beyond that achieved with previous foil optic systems.

At the MIT *Space Nanotechnology Laboratory*, in cooperation with NASA *Goddard Space Flight Center* and the *Harvard Smithsonian Astrophysical Observatory*, technology is being developed for the assembly, manufacture, and metrology of these optic foils. This thesis focuses on the assembly and metrology aspects.

Chapter 2 details the assembly research, in which a device has been designed and manufactured to assemble optic foils repeatably and accurately, making substantial progress towards achieving the *Constellation-X* mission performance goals. This device has been designed for planar foils, which suffice for the reflection gratings, and can be modified for hyperbolic and parabolic focusing optics. This method for assembling nested, segmented foil optics with sub-micron accuracy and repeatability uses lithographically manufactured silicon alignment microstructures, called microcombs [7]. A system of assembly tooling incorporating the silicon microstructures, called an assembly truss, is used to position the foils which are then bonded to a spaceflight module. The advantage of this procedure is that the flight module has relaxed tolerance requirements while the precision assembly tooling can be reused. Previous work [1] has demonstrated that the microcombs can provide accurate and repeatable reference surfaces for the optic foils; current research has developed a device that makes progress towards actual flight module assembly. Key features include flexure bearings for frictionless motion of the microcombs, kinematic couplings to ensure repeatable alignment of successive flight modules, and flight module integration.

Chapter 3 addresses measurement of an optic foil's shape. Individual foils have challenging flatness requirements; foils require figure errors less than 500 nm over their $140 \times 100 \text{ mm}^2$ surface area. Accurate metrology is critical to verify that these foils meet surface shaping and assembly requirements. Concerning shaping, metrological feedback closes the loop on the manufacturing process, since quantification of figure errors permits the evaluation of process improvements. During assembly, micron level distortions to the foil optic may occur due to gravity or friction. Material thermal expansion mismatch may also cause low spatial frequency distortion. The study of these effects requires a metrology tool with a large viewing area, high angular resolution, and large angular range. A deep-ultraviolet (deep-UV) Shack-Hartmann surface metrology system has been designed and implemented to meet this need. The deep-UV wavelengths are particularly useful for studying transparent substrates such as borosilicate glass which are virtually opaque to wavelengths below 260 nm.

Chapter 4 presents how thin materials such as silicon wafers and glass sheets deform and how they can be constrained to minimize these effects. Both finite element analyses (FEA) and analytical calculations are utilized to understand the effects of gravity on foil deformation while varying parameters such as foil thickness and angle of inclination. Friction forces imparted during foil manipulation are studied as well as foil vibration amplitudes, sources, and mitigation. Thermal expansion mismatch between the foil and constraint device is also evaluated. These theoretical analyses form the basis for a set of functional requirements for the design of a foil fixture: a device which can hold these thin, floppy foils with kinematic mounting and minimal deformation. This device can position the glass or silicon foil with angular repeatability sufficient to accurately measure the foil figure errors without introducing substantial additional distortion.

1.3 Thin optic applications in other fields

Measuring and assembling progressively thinner substrates is an increasingly difficult challenge. From disk drive substrates to flat panel displays, glass must be mechan-

ically maneuvered without substantial distortion. Flatness of silicon wafers in the semiconductor industry is also becoming more important. Silicon-on-insulator (SOI) wafer bonding, for example, requires minimally warped wafers (less than 300 nm amplitude over 10 mm scale) for bonding with tolerable residual stress [8]. A tool for surface mapping of thin, transparent materials is useful for quality control of glass substrates of computer hard disks, photomask flatness testing in the semiconductor industry, and flat panel display metrology in addition to the x-ray telescope segmented optics primarily described in this thesis.

Chapter 2

Foil optic assembly truss

Accurate and repeatable assembly of thousands of individual foil optics will be required for the NASA *Constellation-X* mission. This assembly research is another link in the chain towards that goal. Mongrard [1, p. 61] has made substantial progress in proving key technologies for successful assembly. This generation of technology makes strides towards simulating *actual* assembly conditions. The optic foils used in this research very closely resemble the telescope optics in dimensions and material properties. Procedures for assembling many foils within a single flight module have been studied as well as procedures for assembling multiple flight modules. The metrology frame has been effectively separated from the assembly tool mechanical structure, which are both separated from the flight module. All of these factors impact the assembly accuracy and repeatability. Fundamental aspects of the assembly technology have been redesigned based on theoretical analyzes. Actuator and metrological feedback have been improved, leading to accurate analytical models of the assembly process. These models have been validated with experimental testing yielding sub-micron repeatability and accuracy results.

2.1 Functional requirements

The basis for an engineering design is a set of functional requirements which describe what the design must do. For the design of the assembly tool that will meet the per-

formance requirements of the telescope, two functional requirements were identified for the scope of this research.

1. Optic foils must be aligned parallel to each other with tolerances that correspond to 2 arcsec resolution. This implies alignment of the front faces of the foils to within 1 μm of their intended positions repeatably and accurately.
2. Optic foils must be held in their aligned positions inside a flight module structure, which is both rigid and lightweight, for transport to space.

Achievement of these fundamental milestones will establish a basis for the full telescope assembly technology and procedures.

2.2 Optic foils

The proposed optic foils have dimensions $140 \times 100 \text{ mm}^2$ with 200-400 μm thickness. Foil material options currently being studied include borosilicate glass (Schott, model D-263 [9]) and silicon wafers. Foil specifications include a flatness of 500 nm over the surface of the optic, thickness variation of 20 μm , and surface roughness tolerance of $<0.5 \text{ nm}$. These foil size specifications are driven by the telescope weight budget and assembly technology. Flatness and surface roughness requirements are driven by resolution goals. Here, when we use the term “flatness,” we mean the shape of the front surface of the optic, and not the thickness variation which is widely misused. The mission plan includes up to 25 flight modules each holding 120 optic foil mirrors.

Currently, foils can not be manufactured to these flatness tolerances. The MIT *Space Nanotechnology Laboratory* is actively involved in this research [10, 11]. Table 2.1 shows the typical warp, or flatness, of stock thin materials under consideration for the telescope optics along with useful mechanical properties. The silicon wafers are anisotropic, so the stiffnesses along the three crystallographic orientations have been averaged to estimate the expected stiffness during constraint. This estimation simplifies the analytical and simulation calculations. The true derived values for the Young’s modulus are given in Table 2.2 [12].

Properties		D-263 glass	Silicon wafer	Aluminum
Thickness	μm	400	475	
Thickness variation	μm	20	0.5	
Flatness (warp)	μm	600	6	
Young's modulus	N/mm^2	72900	160000	69000
Density	g/cm^3	2.51	2.33	2.72
Thermal Expansion Coefficient (CTE)	$10^{-6}/^\circ\text{C}$	7.2	3.68	23

Table 2.1: Properties of materials for thin foil optics with aluminum as a reference.

Miller Index for Orientation	Young's Modulus (E) (GPa)
[100]	129.5
[110]	168.0
[111]	186.5

Table 2.2: Derived values for Young's modulus for Si.

The flatness of the borosilicate glass has been provided by the manufacturer according to the definitions shown in Figure 2-1. The warp tolerance of the 400 μm thick glass sheets is 600 μm . The silicon wafer flatness has been determined from Hartmann and Shack-Hartmann apparatuses in the MIT *Space Nanotechnology Laboratory*. These in-house measurements of the silicon wafers verify manufacturer specifications.

For all assembly research to date, two types of optic foils have been used. The

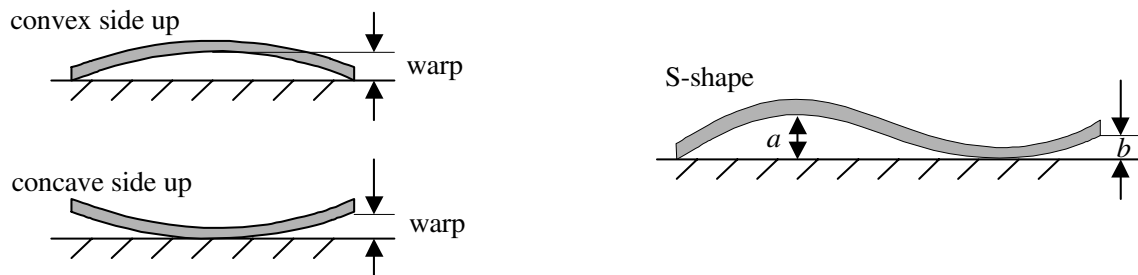


Figure 2-1: Warp is measured by placing the glass on a flat table without external mechanical constraints. S-shaped glass does not meet quality control specifications if dimensions a and $b > \text{warp tolerance}/2$. Warp tolerance is 600 μm for a 400 μm thick foil. (Schott Glas)

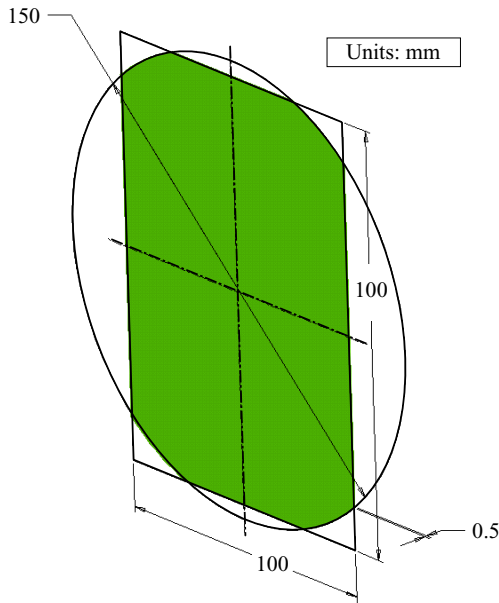


Figure 2-2: Model of the silicon foil used for experimentation with assembly truss.

first are relatively thick, 2.3–3 mm, quartz plates coated with a reflective gold or aluminum surface. The dimensions of these plates vary and are described in the relevant section of this thesis. These “dummy” foils are stiff enough to neglect foil deformation as a source of error in the assembly measurements. The second type of foil is a 150 mm silicon wafer, double-side polished, with a thickness of $475 \pm 0.25 \mu\text{m}$. From this circular wafer, a rectangle of dimensions $140 \times 100 \text{ mm}^2$ was cleaved as shown in Figure 2-2.

2.3 Previous assembly research

2.3.1 Assembly procedure

The foil alignment tolerances for the NASA *Constellation-X* mission go well beyond those of previous segmented foil optic telescopes. To meet these tolerances, Mongrard [1] has initiated a novel assembly scheme. In this process, depicted in Figure 2-3, the optic foils are first loosely held inside a flight module. The flight module is

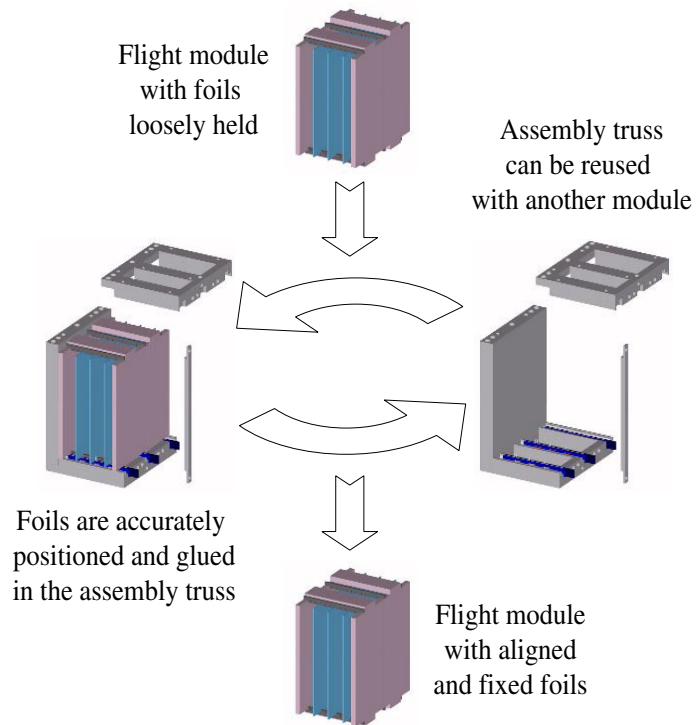


Figure 2-3: Assembly procedure. Foils are first held loosely in the flight module. The flight module is then inserted into the precision assembly truss. The foils are aligned and bonded to the flight module. The assembly truss is removed and reused to align the foils in another flight module.

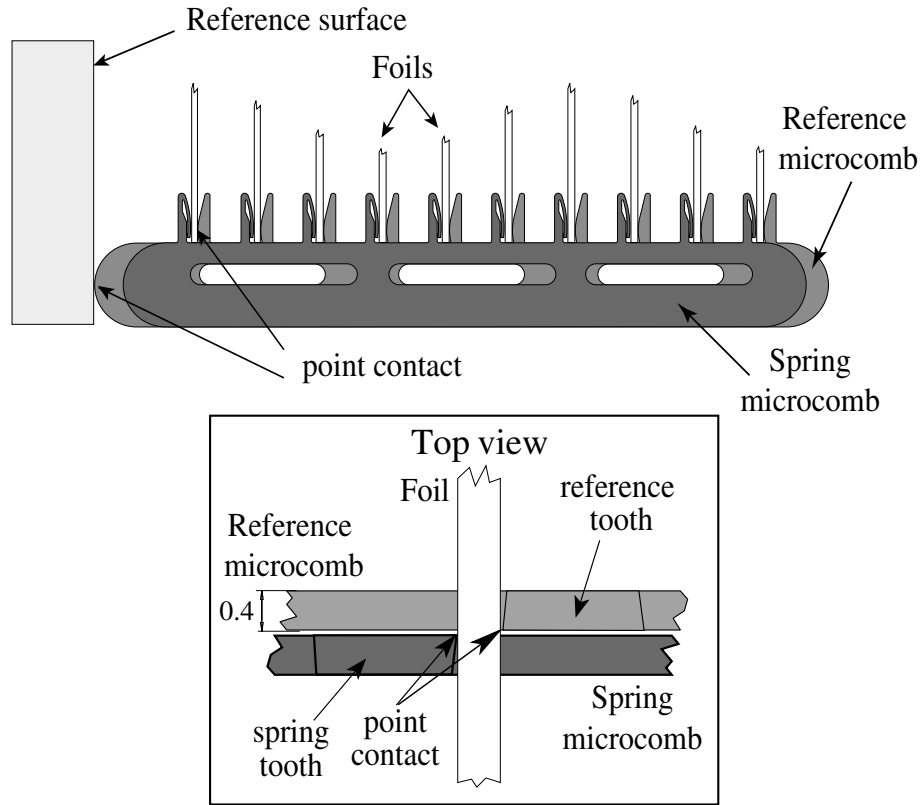


Figure 2-4: Foils are forced into alignment by the spring microcombs against the reference microcombs. The reference microcombs are registered against the reference flat surface.

then inserted into precision assembly tooling, where the foils are manipulated into aligned positions and then glued in place. The flight module is then removed from the assembly tooling. The advantage of this procedure is that the flight module has relaxed tolerance requirements while the precision assembly tooling can be reused.

2.3.2 Microcombs

Within the precision assembly tooling, a set of silicon microstructures, called microcombs [7], are used to perform the alignment. According to the previous work, when the foils are “clipped by [a set of] silicon microcombs with a point-like contact at their top and bottom edges. . . [they] provide accurate positioning of the foils. The microcombs in turn are referenced with point-like contact against an ultra-flat reference surface [1, 13].” This arrangement is shown in Figure 2-4 and 2-5.

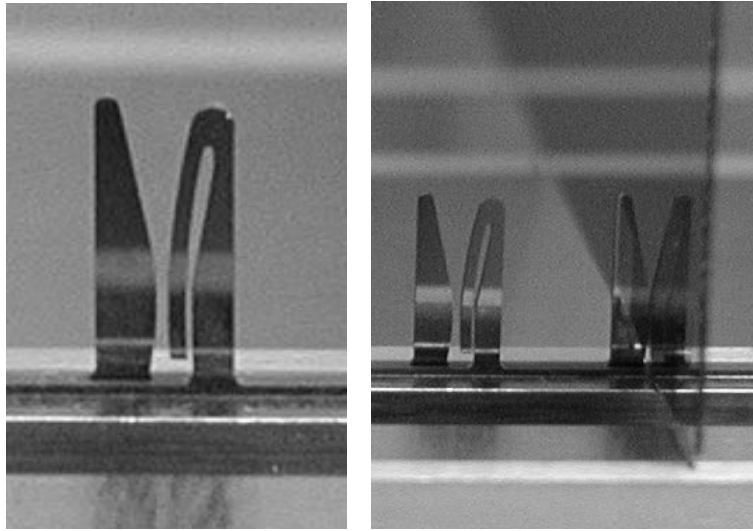


Figure 2-5: Side view of microcombs installed in the assembly tooling (*left*) and a dummy foil pinched in between them (*right*).

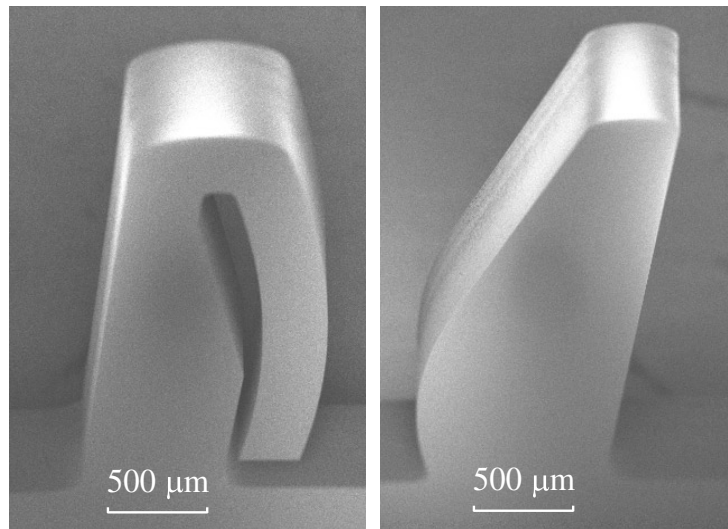


Figure 2-6: Scanning electron microscope (SEM) images of silicon spring (*left*) and reference (*right*) microcomb teeth.

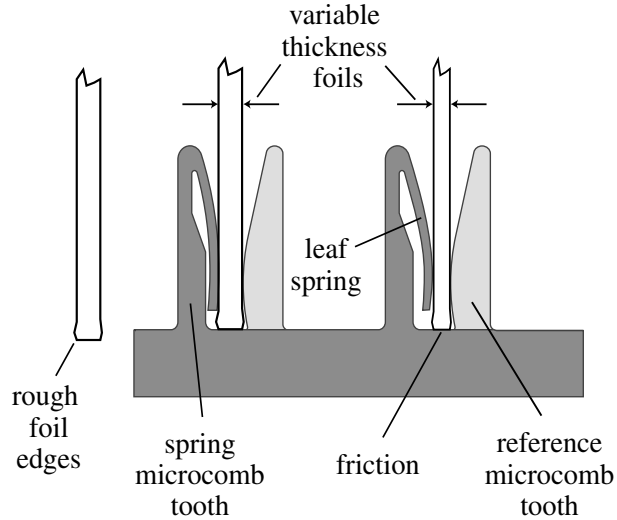


Figure 2-7: The spring comb design ensures that foils of varying thickness can all be pushed up against the reference comb teeth.

The previous assembly research has developed high-accuracy silicon microcombs of two types: reference microcombs and spring microcombs (See Figure 2-6). Mongrard’s design provides that “the circular extremities of the reference microcombs come into a precision point contact with the reference flat in order to provide a precise reference between the foils and the reference flat. The teeth of the reference microcombs then form accurate reference surfaces for the [optic foils] to register against [1, p. 65].” This detail is shown in Figure 2-4. According to Mongrard, the “spring microcombs can be actuated and provide sufficient force to push the foils against the reference microcombs. As the spring microcomb slides. . . , each foil is pushed against its corresponding tooth on the reference microcomb (See Figure 2-4). Furthermore, their special shape [can accommodate] thickness variation of the foils [1, p. 67].” The ability of the spring combs to accommodate foils of varying thickness is depicted in Figure 2-7.

These microcombs are manufactured by etching a silicon wafer using micro-electro-mechanical systems (MEMS) technology to sub- μm accuracy. The manufacturing accuracy on this generation of combs has been quantified to be 200 nm at NASA’s *Goddard Space Flight Center* [14] using a Moore Coordinate Measuring Machine (CMM) which features a touch probe and interferometers to determine stage

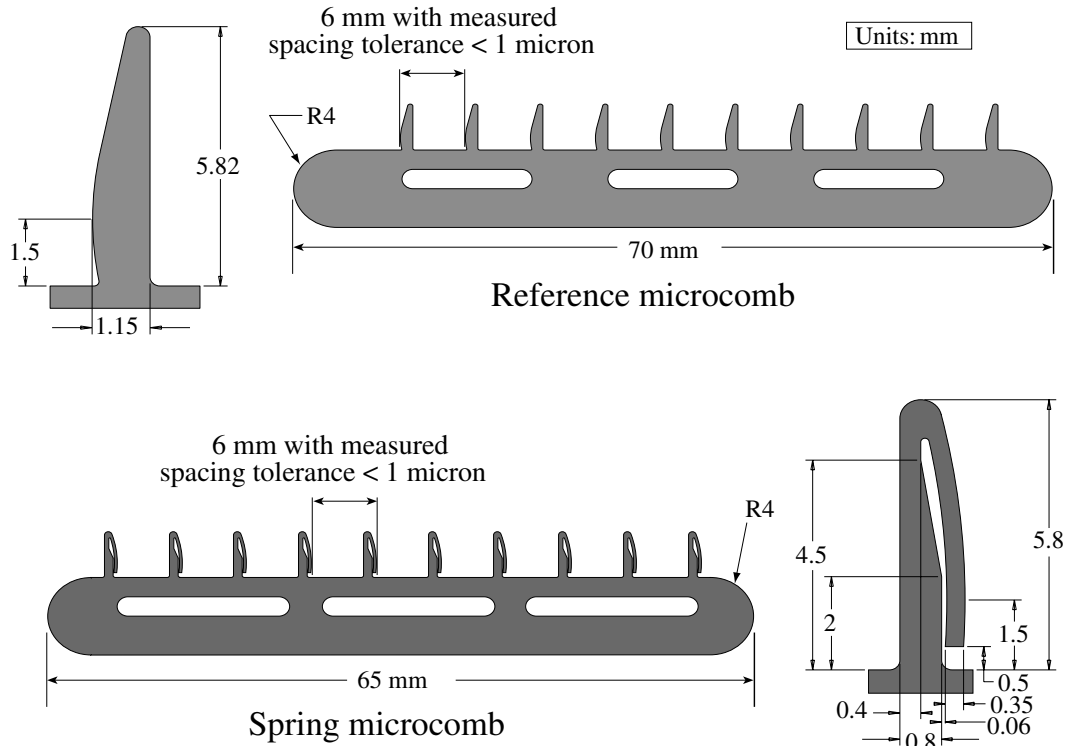


Figure 2-8: Reference and spring microcomb dimensions used for previous assembly research.

position. The dimensions of the combs used in this previous research are shown in Figure 2-8.

The engineering design of these original microcombs has been studied by Mongrard [1] and the complexities of their manufacture have been pioneered by Chen [2] and later explored by Sun [15, 16]. The design and results of the previous assembly truss research by Mongrard are summarized in the following section. The relationship and distinctions of this research to the previous work have been noted on page 35.

2.3.3 First-generation assembly truss

Design

The first attempt at using microcombs for optic foil assembly was made by Mongrard [1] at the MIT *Space Nanotechnology Laboratory*. In this research, a breadboard test assembly system was designed and manufactured to measure the alignment ca-

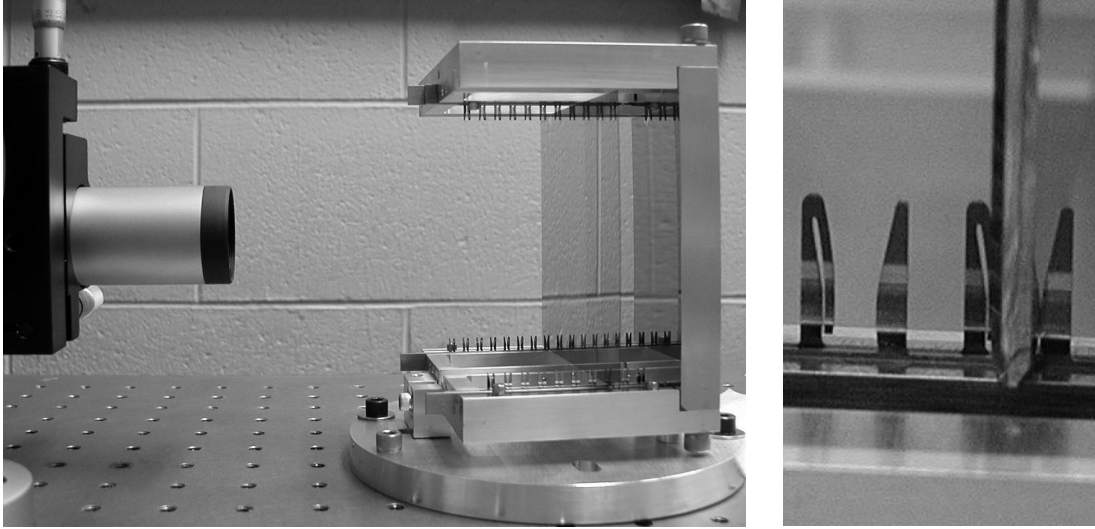


Figure 2-9: First-generation of the assembly truss technology utilizing the microcomb design for foil alignment. A single flat plate is installed (*left*). Close up of the spring and reference comb constraining the aligned foil (*right*).

pabilities of the microcombs. This device demonstrated “proof of principle” for the assembly concept and microcomb technology. The hardware is shown in Figure 2-9.

The system has rectilinear geometry and is designed to orient a fused-silica plate of dimensions $102 \times 102 \times 2.3 \text{ mm}^3$ and flatness specified to be less than $2 \mu\text{m}$. For this work, the fused-silica plate was coated with approximately 1000 \AA of gold to make it reflective to permit metrology during testing.

This assembly truss consists of a base plate, a reference flat, and a top plate. The base plate and top plate are responsible for supporting and guiding the microcomb sets. The reference flat is a diamond turned aluminum plate which also acts as a structural member. A model of the assembly truss is shown in Figure 2-10 along with the its overall dimensions.

In this system, reference and spring microcombs, which are first attached to steel support bars that lend additional strength and rigidity, are assembled to both the top and base plates by springs. Those springs facilitate linear travel along the slots and reduce the number of precision surfaces required.

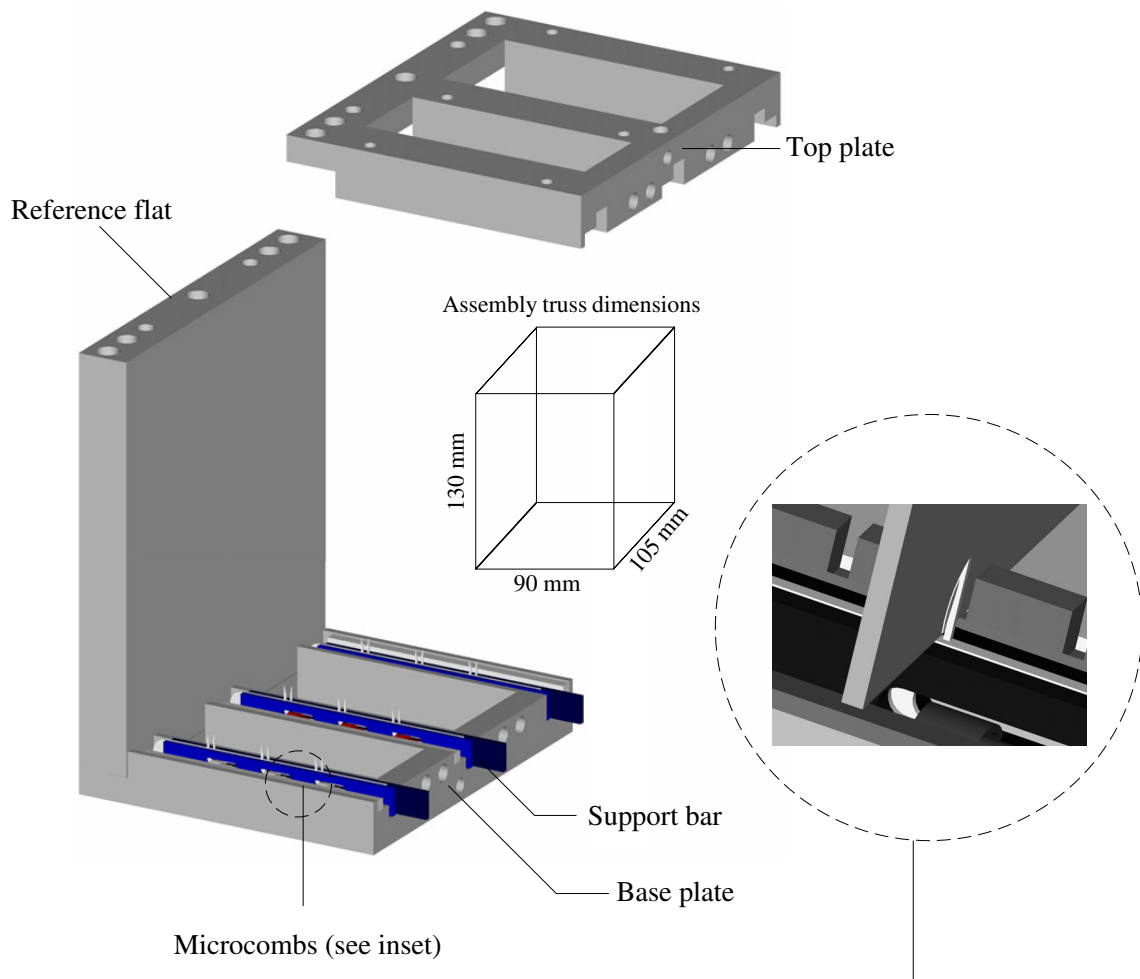


Figure 2-10: The parts of the first-generation assembly truss are assembled in an open structural loop to facilitate metrology of the optics. The reference flat and microcombs establish the metrology frame. The microcombs' function is illustrated with an optic foil (*inset*).

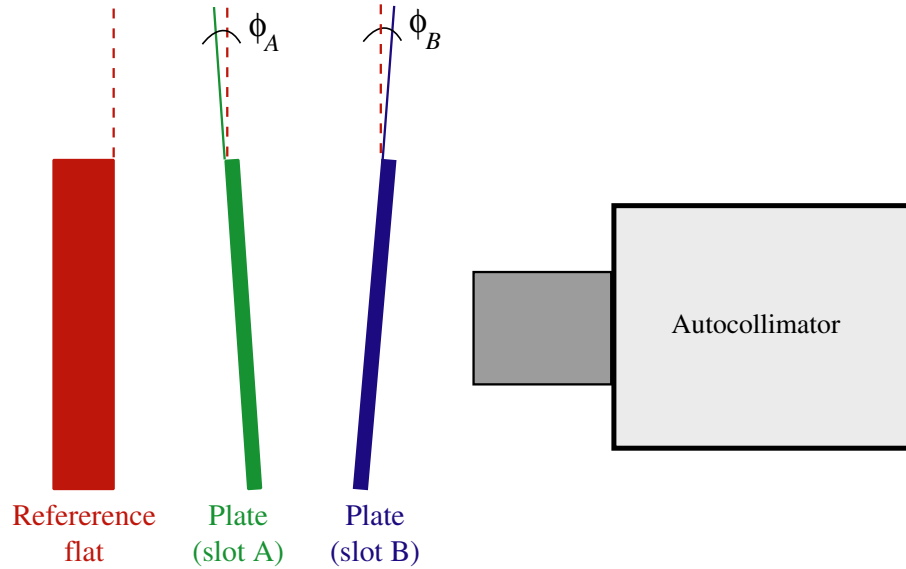


Figure 2-11: The autocollimator provides measurement of the angles ϕ_A or ϕ_B . These angles represent the deviation from zero in pitch only (yaw reading also gathered) from the planar reference flat if the autocollimator is zeroed from the flat. Drift of the autocollimator reading with time must be accounted for as well.

Setup, Experiments, and Results

Numerous tests were performed on the first-generation assembly tool [1]. The tests and results discussed here are those that serve directly as a comparison to the current research. The experimental setup was constant in the tests performed on the first-generation assembly truss. Two pairs of microcombs were installed on the base plate and one pair was installed in the center of the top plate as shown in Figure 2-9. Metrology was performed by an autocollimator (Newport, model LAE500-C). The autocollimator works by emitting a collimated laser beam and measuring its angle of reflection. As shown in Figure 2-11, the angles in pitch and yaw of the plate can be measured in different slots in the microcombs, or the angle of the reference flat to the autocollimator can also be measured. The angles can be converted to linear measurements as shown in Appendix A, page 149.

For all of the tests presented here, the assembly truss was in the following configuration:

1. The spring comb teeth *did not touch* the fused-silica dummy optic plate. Their

presence only served to support the weight of the plate and they were not physically moved.

2. The reference combs *were not moved* once contact with the reference flat was believed to be made by pushing on the support bar by hand until resistance was felt.

Three relevant tests were performed: single-slot repeatability, slot-to-slot accuracy, and slot-to-reference flat accuracy. The single-slot repeatability test involved a repeated process of lifting and replacing a fused-silica plate against stationary reference microcomb teeth in a given slot and measuring its pitch and yaw. These angles were then converted to linear displacements and statistical analyses were performed. Results for the pitch data for a given slot 1, for example, yielded mean pitch, μ_{slot1} , and standard deviation, σ_{slot1} . The number quoted for the single-slot repeatability was σ_{slot1} .

To measure the slot-to-slot accuracy, the single-slot test was repeated on slots 2–9 and the same statistics were calculated. The average pitch for all slots was computed as $\mu_{allslots}$. This value of $\mu_{allslots}$ is the average of the individual slot averages (i.e. μ_{slot1} , μ_{slot2} , μ_{slot3} , etc.) The slot-to-slot accuracy for slot 1 is then defined as $\mu_{allslots} - \mu_{slot1}$.

The slot-to-reference flat accuracy for slot 1 was given as μ_{slot1} , assuming that the autocollimator has been zeroed at the reference flat. Autocollimator drift was compensated. The data for this test was reduced by 2 μm in pitch and 1.1 μm in yaw to remove a perceived error contribution from distortion of the reference flat [1, p. 91]. The results for these three tests for most slots are shown in Table 2.3.

Analysis and Conclusions

The results from the first-generation assembly truss were extremely encouraging. If the actual telescope optics were to be assembled with this sub-micron level of accuracy, resolution on the order of 2 arcsec would be realizable. However, this experimental work was only proof-of-concept. The research on the first-generation assembly

slot	displacement error (μm)					
	repeatability		slot-to-slot		reference flat	
	pitch	yaw	pitch	yaw	pitch	yaw
2	0.01	0.03	-0.2	0.5	-0.4	0.5
3	0.04	0.10	0.3	0.0	0.1	0.1
4	0.07	0.02	-0.1	-0.4	-0.3	-0.3
5	0.10	0.13	0.2	0.1	0.0	0.2
8	0.07	0.01	0.1	0.1	-0.2	0.2
9	0.30	0.21	-0.3	-0.3	-0.6	-0.2

Table 2.3: First-generation assembly truss alignment results.

truss proved that the microcombs have the potential to provide accurate and repeatable reference surfaces for segmented foil optics. The results are spectacular when considering the functional requirements for the assembly technology, but there is a challenging list of milestones to be met before the *Constellation-X* mission optics can be assembled to the desired tolerances.

The current, or second-generation, assembly truss research strives to prove the feasibility of assembling foil optics accurately and repeatably. The following list explains the challenges inherent to this objective which remain after the first-generation truss research. This list incorporates recommendations for a redesign in the second-generation assembly technology.

1. The circular extremities, or “noses,” of the reference combs must be actuated accurately and repeatably to a reference surface. Stationary combs understandably show good repeatability in the first-generation design.
2. Assembling 200-400 μm thick foils will be necessary. These foils could illuminate major design problems if their deformation prevents repeatable or accurate assembly.
3. An independent flight module must be integrated into the assembly truss.
 - This module should hold the foils loosely before alignment and permit external access for metrology and gluing the aligned foils.

- To manufacture multiple flight modules with sub- μm repeatability, the assembly truss must be able to *repeatably* constrain the flight module and be *repeatably* taken apart and put back together again.
4. Errors in the assembly tool need to be quantified. Errors in the angle of the microcomb to the reference flat (non-perpendicularity) can consume the allowable $2\ \mu\text{m}$ functional requirement as shown in the error budget analysis in Section 2.5.2.
 5. The spring combs should be able to independently slide the foils into contact with reference teeth without changing the position of the reference combs, distorting the foil shape, or damaging the foil, reference teeth, or spring teeth due to Hertzian compressive stresses.
 6. The structural loop on the assembly truss should be closed to ensure a stiff and accurate metrology frame. An open structural loop is less structurally and thermally stable. The lack of symmetry in an open loop leads to undesirable thermal gradients and bending moments. The fact that a critical part of the structure is cantilevered means that Abbe errors abound* [17].
 7. A highly coupled metrology frame and structure should be avoided. In the first-generation truss, deformation to the reference surface from this coupling occurred on the order of $2\ \mu\text{m}$ [1, p. 91]. A properly designed metrology frame is unaffected by dynamic or static loads within the machine, and acts as a static structure for moving sensors to measure against.
 8. Active sensing of the state of the alignment will be critical.
 - Feedback of the entire foil shape during assembly will be useful to understand deformations due to external loads (i.e. foil pinching from spring and reference combs, friction forces, gravity loading).

*Abbe errors occur when an angular error is allowed to manifest itself in a linear form via amplification by a lever arm. Mathematically this error has a magnitude equal to the product of the lever arm's length and the sine of the angle. Also known as sine error.

- Monitoring the microcombs’ positions, or simply whether their noses are in contact with the reference surface, will indicate the “green light” for alignment success.

2.4 Design process

For the current second-generation of assembly technology, the functional requirements in Section 2.1 were evaluated anew. For each of the functional requirements, a Rohrback process [17] was performed to generate ideas for the following:

Design Parameters Strategies for how to address the functional requirements

Analysis Physics calculations for the design parameters

References Where physics formulae or analytical data were obtained

Risks What might go wrong with the design parameters or analyses

Countermeasures How to address those risks

The results of this study are shown in Figure 2-12. Based on the excellent results of the previous work and this analysis, the decisions were made to (1) use the microcomb technology to provide highly accurate and repeatable reference surfaces for the foil alignment and (2) use the separate assembly tooling and flight module concept to perform assembly.

The design process was undertaken by a three-member team in a semester-long graduate course, *Precision Machine Design*, at the Massachusetts Institute of Technology.[†]

[†]The project team included the following members:

Matthew J. Spenko Ph.D. candidate in *Field and Space Robotics Laboratory*

Yanxia Sun Ph.D. candidate in *Space Nanotechnology Laboratory*

Craig R. Forest Master’s student in *Space Nanotechnology Laboratory*

Alexander H. Slocum Professor of *Precision Machine Design* course and team mentor

Mark L. Schattenburg Director of *Space Nanotechnology Laboratory* and team mentor

Functional Requirements	Strategy	Physics	Risks	Counter-Measures	
Align the foils parallel to each other to achieve 2 arc second resolution. This corresponds to placing the front face of the foil to within 1 micron of its intended position repeatedly and accurately.	Align foils using MEMS fabricated micro-combs with reference to a flat plate	Accuracy of combs to flat plate, mechanics (cantilever beams, simply supported beams)	Reference flat gets deformed when combs are placed against it	Carefully stop combs at first sign of contact	
			The combs become clipped when pressed against the reference flat	Careful/ slow placement of combs	
Foil alignment is done by one "Assembly Fixture" for all of the flight modules	Stack foils with spacers in between them	Friction, Mechanics of Materials	Reference flat gets scratched Spacers scratch foils Sheets are different shapes Stack up error because of different foil thicknesses	Minimize touching of reference flat Use low coefficient of friction material/ work in clean room Machine different shaped spacers	
	Real-Time measurement of distance between foils coupled with movement of each corner of the foils	Measurement Technology	Slow process (100 sheets x 25 modules) Measurement error Actuation too coarse	Spend more money/ time Survey measurement technology Use sub micron capable stepper motors/ linear stages	
	Foil alignment is done by one "Assembly Fixture" for all of the flight modules	Alignment process and fixtures exist on every flight module	Proper alignment, geometry	Foils can be damaged while in "loose" configuration	Handle carefully
				Deformation can occur if flight module is held differently in alignment and in use Added complexity to flight module	Design to hold assembly in same configuration as test fixture; Kinematically hold the fixture in both places Fine alignment structures are removed and thrown away
Foils must be fixed into place inside a rigid lightweight structure for transport to space		Proper alignment, geometry	Added weight to flight module	Fine alignment structures are removed and thrown away	

Figure 2-12: Design Process chart. The functional requirements, strategies, physics, risks, and countermeasures are also shown. Highlighted rows indicate selected design routes. The physics concerns were too broad to cite specific references.

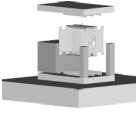
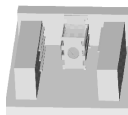
	Design	1. Vertical flat with air-bearing 	2. Stack with kinematic couplings 	3. Fixed truss 	4. L-truss with air-bearing 	5. Fixed reference flat with air bearing 
	Value					
Accuracy	*****	+	0	-	0	0
Repeatability	*****	+	0	-	+	+
Cost	**	-	+	0	-	-
Complexity of design	*	-	+	0	-	-
Complexity of assembly	**	+	0	-	+	+
Lifetime	***	+	0	-	+	+

Figure 2-13: The Pugh chart qualitatively identifies concept strengths and weaknesses. From this chart, the (1) vertical air-bearing design and (2) stack design were pursued further.

2.5 From conceptual designs to selection

Based on the Design Process chart (See Figure 2-12) and the recommendations from the first-generation truss research on page 48, many conceptual designs for the second-generation assembly tool were developed. These ideas started as hand sketches and stick figures. Appendix B, page 153, shows all of the conceptual designs that were given serious consideration. A Pugh chart was one of the tools used to help determine which designs would work best. This chart is shown in Figure 2-13. Two of the concepts in Appendix B were taken to the next stage of the design process. The stack (See page 155) and the vertical air-bearing concepts (See page 159) were studied in more detail to analytically evaluate which design would be better overall.

2.5.1 Error budget theory

A preliminary error budget was performed to evaluate the competing stack and air-bearing designs. An error budget allocates resources (allowable amounts of error)

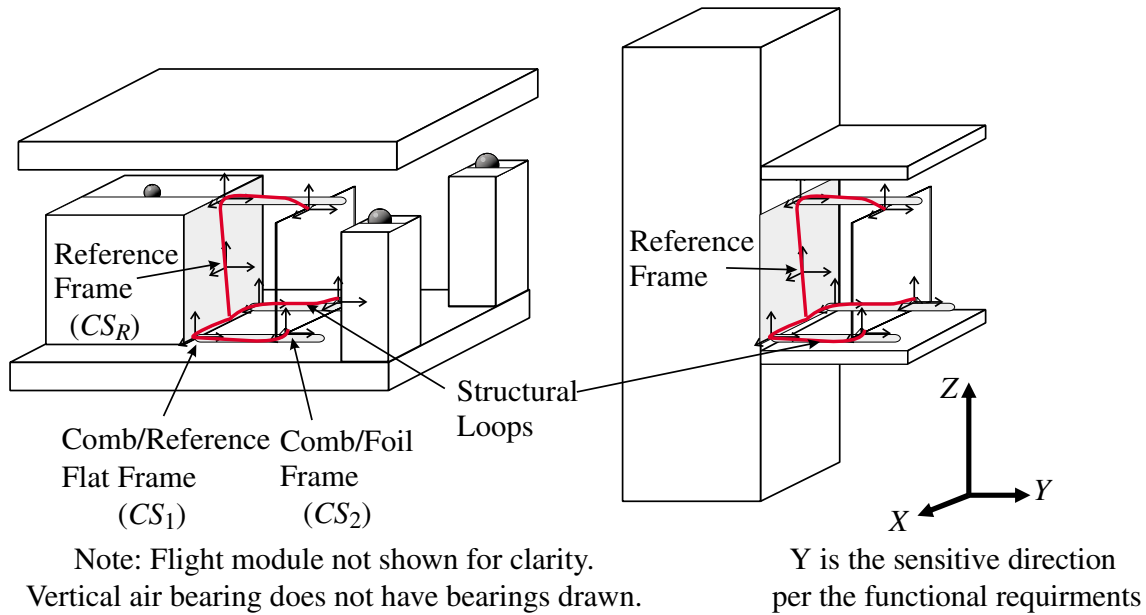


Figure 2-14: The stack design (*left*) and the vertical air-bearing design (*right*). The reference frame, CS_R , is located at the center of the reference flat. Coordinate system CS_1 is located at the interface between the microcomb and the reference flat. Coordinate system CS_2 is at the interface between the microcomb tooth and optic foil. In the preliminary error budget, we will consider the structural loop from the reference frame to CS_2 for both concepts.

among a machine's different components [18]. This type of budgeting can indicate if the design can theoretically meet the functional requirements and which aspects of the design most significantly contribute to the overall error. The preliminary error budget at this stage in the work provided a rough estimate of the slot-to-reference flat accuracy of the two competing designs.

The error budgets for these two concepts were guided by the concept design sketches shown in Figure 2-14. The structural loops for each concept are highlighted on the figure. The structural loop connects the reference frame coordinate system (CS_R) to the point-of-action (comb/foil frame or CS_2) through the mechanical structure of the assembly truss. The error budget was formulated based on connectivity rules that define the behavior of a machine's components at their interfaces and combinational rules that describe how errors of different types are to be combined. In general, the first step in developing an error budget is to model the system in the form of a series of homogeneous transformation matrices (HTM). An HTM will be

located at each rigid body of the machine and it will describe that body's location and rotation with respect to the previous HTM. Error motions for each body's six degrees of freedom (three translational and three angular) are also included in the HTM. The HTM's are then sequentially multiplied to model the structure from the point-of-action to the reference frame coordinate system. We will start the mathematical formulation by defining the position of a coordinate system in three-dimensional space with respect to a known coordinate system. This known coordinate system would be the reference frame for the first coordinate system, the first coordinate system for the second, and so on. A coordinate system's location and orientation is defined by

$${}^{n-1}T_n = \begin{bmatrix} O_{ix} & O_{iy} & O_{iz} & x \\ O_{jx} & O_{jy} & O_{jz} & y \\ O_{kx} & O_{ky} & O_{kz} & z \\ 0 & 0 & 0 & 1 \end{bmatrix} \quad (2.1)$$

where subscript n denotes the coordinate system number and $n-1$ denotes the coordinate system preceding n in the structural loop. The first three columns are direction cosines (unit vectors i, j, k) representing the rotation of the rigid body's axes (X_n, Y_n, Z_n) with respect to the preceding coordinate system ($X_{n-1}, Y_{n-1}, Z_{n-1}$). The last column represents the pure translation of the rigid body with respect to the preceding coordinate system. The coordinate systems in the structural loop are not rotated with either design (See Figure 2-14), so the general coordinate system formulation reduces to

$${}^{n-1}T_n = \begin{bmatrix} 1 & 0 & 0 & x \\ 0 & 1 & 0 & y \\ 0 & 0 & 1 & z \\ 0 & 0 & 0 & 1 \end{bmatrix} \quad (2.2)$$

where x, y, z represent the translations as before. The next step in generating an error estimation is to calculate the error matrix for each coordinate system in the structural loop. Assuming the angular errors are small (on the order of arc minutes),

the error in the position of a rigid body with respect to its ideal position is

$$E_n = \begin{bmatrix} 1 & -\varepsilon_Z & \varepsilon_Y & \delta_X \\ \varepsilon_Z & 1 & -\varepsilon_X & \delta_Y \\ -\varepsilon_Y & \varepsilon_X & 1 & \delta_Z \\ 0 & 0 & 0 & 1 \end{bmatrix} \quad (2.3)$$

where these errors are defined with respect to the rigid body's coordinate system location. Linear motion errors in the three principal axes are indicated by δ_X , δ_Y , δ_Z . Angular errors about the axes are represented by ε_X , ε_Y , ε_Z .

To generate the HTM for each coordinate system, Equations 2.2 and 2.3 should be multiplied:

$${}^{n-1}H_n = {}^{n-1}T_n E_n \quad (2.4)$$

$${}^{n-1}H_n = \begin{bmatrix} 1 & -\varepsilon_Z & \varepsilon_Y & x + \delta_X \\ \varepsilon_Z & 1 & -\varepsilon_X & y + \delta_Y \\ -\varepsilon_Y & \varepsilon_X & 1 & z + \delta_Z \\ 0 & 0 & 0 & 1 \end{bmatrix}. \quad (2.5)$$

In general, N rigid bodies can then be connected to determine the relating matrix between the point-of-action and reference coordinate system. Mathematically,

$${}^R H_N = \prod_{n=1}^N {}^{n-1}H_n = {}^R H_1 {}^1 H_2 {}^2 H_3 \cdots {}^{N-1} H_N. \quad (2.6)$$

For the examples at hand, there are two coordinate systems leading from the reference frame to the comb/foil frame as shown in Figure 2-14. To connect CS_R to CS_2 , the error for the conceptual designs can be formulated as

$${}^R H_2 = {}^R H_1 {}^1 H_2 \quad (2.7)$$

$${}^R H_2 = \begin{bmatrix} 1 & -\varepsilon_{Z1} & \varepsilon_{Y1} & x_1 + \delta_{X1} \\ \varepsilon_{Z1} & 1 & -\varepsilon_{X1} & y_1 + \delta_{Y1} \\ -\varepsilon_{Y1} & \varepsilon_{X1} & 1 & z_1 + \delta_{Z1} \\ 0 & 0 & 0 & 1 \end{bmatrix} \begin{bmatrix} 1 & -\varepsilon_{Z2} & \varepsilon_{Y2} & x_2 + \delta_{X2} \\ \varepsilon_{Z2} & 1 & -\varepsilon_{X2} & y_2 + \delta_{Y2} \\ -\varepsilon_{Y2} & \varepsilon_{X2} & 1 & z_2 + \delta_{Z2} \\ 0 & 0 & 0 & 1 \end{bmatrix}. \quad (2.8)$$

The last column of ${}^R H_2$ is the position of the comb/foil frame (CS_2), including the linear and angular error contributions from the preceding coordinate system. Using linear algebra to extract the last column:

$$\begin{bmatrix} X_t \\ Y_t \\ Z_t \\ 1 \end{bmatrix} = {}^R H_2 \begin{bmatrix} 0 \\ 0 \\ 0 \\ 1 \end{bmatrix} \quad (2.9)$$

$$\begin{bmatrix} X_t \\ Y_t \\ Z_t \\ 1 \end{bmatrix} = \begin{bmatrix} x_1 + x_2 + \delta_{X1} + \delta_{X2} + (z_2 + \delta_{Z2})\varepsilon_{Y1} - (y_2 + \delta_{Y2})\varepsilon_{Z1} \\ y_1 + y_2 + \delta_{Y1} + \delta_{Y2} - (z_2 + \delta_{Z2})\varepsilon_{X1} + (x_2 + \delta_{X2})\varepsilon_{Z1} \\ z_1 + z_2 + \delta_{Z1} + \delta_{Z2} + (y_2 + \delta_{Y2})\varepsilon_{X1} - (x_2 + \delta_{X2})\varepsilon_{Y1} \\ 1 \end{bmatrix}. \quad (2.10)$$

To find the linear error in CS_2 , we then simply subtract Equation 2.10 from the ideal position, which is defined by

$$\begin{bmatrix} X_{\text{ideal}} \\ Y_{\text{ideal}} \\ Z_{\text{ideal}} \\ 1 \end{bmatrix} = \begin{bmatrix} x_1 + x_2 \\ y_1 + y_2 \\ z_1 + z_2 \\ 1 \end{bmatrix}. \quad (2.11)$$

So the error in the position of CS_2 from the ideal position will be

$$\begin{bmatrix} \delta_{Xt} \\ \delta_{Yt} \\ \delta_{Zt} \\ 0 \end{bmatrix} = \begin{bmatrix} X_t \\ Y_t \\ Z_t \\ 1 \end{bmatrix} - \begin{bmatrix} X_{\text{ideal}} \\ Y_{\text{ideal}} \\ Z_{\text{ideal}} \\ 1 \end{bmatrix} \quad (2.12)$$

$$\begin{bmatrix} \delta_{Xt} \\ \delta_{Yt} \\ \delta_{Zt} \\ 0 \end{bmatrix} = \begin{bmatrix} \delta_{X1} + \delta_{X2} + (z_2 + \delta_{Z2})\varepsilon_{Y1} - (y_2 + \delta_{Y2})\varepsilon_{Z1} \\ \delta_{Y1} + \delta_{Y2} - (z_2 + \delta_{Y2})\varepsilon_{X1} + (x_2 + \delta_{X2})\varepsilon_{Z1} \\ \delta_{Z1} + \delta_{Z2} + (y_2 + \delta_{Z2})\varepsilon_{X1} - (x_2 + \delta_{X2})\varepsilon_{Y1} \\ 0 \end{bmatrix}. \quad (2.13)$$

This result gives the displacement of the microcomb tooth tip from where we would ideally like it to be, or the error in the accuracy of positioning the optic foil.

This procedure for finding the error was repeated for both the systematic and random errors. Systematic errors are signed and directional; random errors are unsigned and bidirectional. To accurately estimate the impact of random errors on the design, the sum of the random error effects and the root-sum-squared (RSS) random errors were calculated. The average of these values yields a reasonable estimate for the machine accuracy degradation due to random errors. A more general form of the preceding error budget calculations are available from Slocum [17].

2.5.2 Preliminary error budgets

With a sound theoretical basis, one can now proceed to identify and quantify the errors, both random and systematic, that make up the E_n matrices. The detailed preliminary error budget for the stack concept will be presented, and differences for the air-bearing concept will be noted afterward. Figure 2-15 will help clarify the descriptions of the errors. We will trace the error sources and their effects from the CS_R to CS_2 . This procedure is nearly identical for the complementary structural loop which runs from the same reference coordinate system to the comb/foil frame located on the top center microcomb due to the symmetry of the paths.

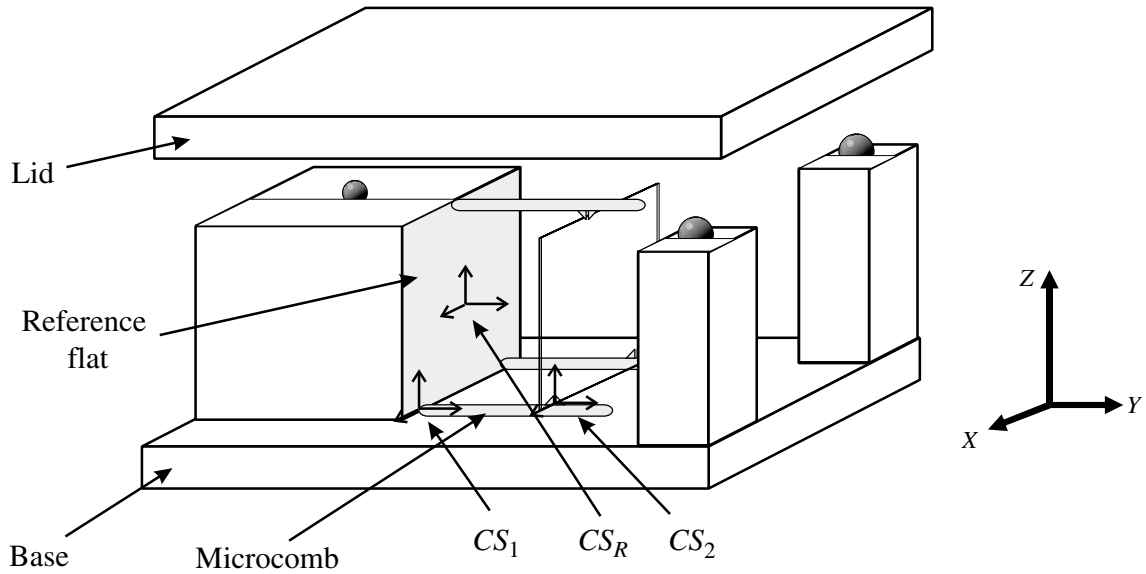


Figure 2-15: Details of the stack concept are shown. This notation will be used in the error budget calculations.

A few assumptions will help get us started:

1. CS_R is attached to the center of the polished face of the reference flat.
2. Errors only occur at the interfaces between parts.
3. This preliminary error budget will lump machine shop manufacturing errors into reasonable estimates. This is necessary because the exact location, size, and number of parts is unknown at this conceptual evaluation phase. A detailed error budget on the final design will itemize each error contribution.
4. Dynamic and thermal errors are not considered. Dynamic errors are nonexistent since the structure achieves a final static configuration when aligned. Thermal errors are not considered under the assumption that time constants for these changes will be longer than the required assembly time.
5. The reference combs are in contact with the reference flat in their “aligned” positions.
6. All errors are assumed to be random *except* for Hertzian contact deformation errors. These have a known sign and are unidirectional.

Starting from CS_R , the vector to the next coordinate system, CS_1 , is noted as:

$$CS_1 = \begin{bmatrix} X(\text{mm}) \\ Y(\text{mm}) \\ Z(\text{mm}) \\ \theta_X(\text{rad}) \\ \theta_Y(\text{rad}) \\ \theta_Z(\text{rad}) \end{bmatrix} = \begin{bmatrix} 25 \\ 0 \\ -70 \\ 0 \\ 0 \\ 0 \end{bmatrix}. \quad (2.14)$$

There is no rotation between any of the coordinate systems in either conceptual design. The 25 mm distance in the X direction between the frames is an estimate of half of the separation between the bottom combs. These combs will support the foil on its 100 mm length side. Recall that the foil dimensions are $140 \times 100 \times 0.4 \text{ mm}^3$. The vertical distance of -70 mm is an estimate of the length in the Z direction from the center of the reference flat to the origin of CS_1 .

Now we need to estimate the three translational and three rotational errors for CS_1 . Table 2.4 gives the magnitude for each random error with its linear or angular category. Most importantly, an explanation is provided to show how the value was calculated. These errors are in the directions shown. Figure 2-15 may be useful to visualize how these errors occur.

Systematic errors for CS_1 are all zero except for the Y direction. The errors in the other five degrees of freedom are zero because they can not be assumed directional or repeatable; hence, they are only random. The systematic error in the Y direction comes from the Hertzian deformation of the microcomb nose at the contact interface with the reference flat. Theoretical predictions (See page 78) and experimental data (See page 80) will later show that contact can be detected with no more than a 0.3 N force between the microcomb and reference flat. This corresponds to a Hertzian deformation of $0.3 \mu\text{m}$. This error can be negated if all microcombs are actuated in the same way, since the deformation for all combs will be the same. For a conservative error budget evaluation, we set the systematic error in Y direction to be $0.3 \mu\text{m}$.

We now need to consider CS_2 , which is located at the interface between the

Axes	Actual Dimensions	Random errors	Error description
X(mm)	25	0.0254	Machine shop tolerances of 0.001 inch dictate how the reference flat will be positioned on the base in this direction.
Y(mm)	0	0.0001	The reference flat flatness specification is 0.1 μm
Z(mm)	-70	0.0254	Machine shop tolerances of 0.001 inch dictate where the contact point between the reference flat and the microcomb will occur in the vertical direction.
θ_X (rad)	0	0.0003	There are three contributions which have been root-sum-squared. The flatness of the bottom of the reference flat is 1/10000. The angular error in the manufacturing of the “support bar” (See Figure 2-10) to which the microcomb is glued is 0.001 inch over the its predicted length of 120 mm. The angular error in the alignment of the comb to the “support bar” is 1/10000. These errors are combined as $\theta_{X\text{random}} =$ $\sqrt{\left(\frac{1}{10000}\right)^2 + \left(\frac{25.4 \times 10^{-3}}{120}\right)^2 + \left(\frac{1}{10000}\right)^2}$
θ_Y (rad)	0	0.0001	There are two contributions which are root-sum-squared. The flatness of the bottom of the reference flat is 1/10000 in this direction. Additionally, the “support bar” flatness on this face is 1/10000. These errors are combined as $\theta_{Y\text{random}} =$ $\sqrt{\left(\frac{1}{10000}\right)^2 + \left(\frac{1}{10000}\right)^2}$
θ_Z (rad)	0	0.0001	Same description as $\theta_{Y\text{random}}$

Table 2.4: Random translational and angular errors in the stack concept CS_1 .

microcomb tooth and the optic foil. Starting from CS_1 , the displacement vector to CS_2 is

$$CS_2 = \begin{bmatrix} X(\text{mm}) \\ Y(\text{mm}) \\ Z(\text{mm}) \\ \theta_X(\text{rad}) \\ \theta_Y(\text{rad}) \\ \theta_Z(\text{rad}) \end{bmatrix} = \begin{bmatrix} 0 \\ 120 \\ 5.5 \\ 0 \\ 0 \\ 0 \end{bmatrix}. \quad (2.15)$$

The 120 mm distance between the frames is an estimate of the required horizontal distance to the comb tooth from CS_1 . The distance from the center of the comb to the foil contact location is 5.5 mm from the previous microcombs (See Figure 2-8). The path from CS_1 to CS_2 travels through the microcomb.

Estimating the random and systematic errors for CS_2 is similar to the previous work. The details will be shown here for completeness and instructive purposes. Figure 2-15 on page 58 again serves as a good companion for interpreting the errors shown in Table 2.5.

For this coordinate system, the systematic errors are all zero except for the Y direction. As in CS_1 , Hertzian deformation of the microcombs is to blame. At the contact interface between the microcomb tooth and the foil, compression causes a linear error due to the thickness variation of the foils. Previous research by Mongrard [1, p. 100] has estimated this error. For the small foil thickness variation of $0.5 \mu\text{m}$ in this work, the systematic error is negligible (less than $0.05 \mu\text{m}$). For the actual flight foils however, the allowable thickness variation is $20 \mu\text{m}$ so the systematic error in the Y direction would be $0.26 \mu\text{m}$ [1, p. 101]. We shall use the smaller, negligible value to accurately model the foils to be used in this research.

Now the random and systematic errors are known for the preliminary stack concept from the reference frame (CS_R) to the bottom left microcomb tooth (CS_2). Using this information and Equation 2.13, the displacement errors can be found from its ideal position. Using a similar procedure, the displacement errors for the top middle comb tooth can be found. In fact, due to the reference frame location choice, the top

Axes	Actual Dimensions	Random errors	Error description
$X(\text{mm})$	0	0.0005	Variation in thickness of microcomb. The manufacturer specification for the wafer thickness is $475 \pm 0.25 \mu\text{m}$
$Y(\text{mm})$	120	0.0006	Tolerances on microcomb manufacturing estimated to be $0.5 \mu\text{m}$ per 100mm of length. The microcomb length is estimated to be 120 mm.
$Z(\text{mm})$	5.5	0.00003	The microcomb manufacturing tolerances of $0.5 \mu\text{m}$ per 100mm of length are applicable. The microcomb height from the centerline to point-of-action is 5.5 mm so mathematically, $\frac{0.5 \times 10^{-3}}{100} = \frac{Z_{\text{random}}}{5.5}$.
$\theta_X(\text{rad})$	0	0.0000	Microcomb angular errors in this direction are accounted for in the Z direction manufacturing tolerances.
$\theta_Y(\text{rad})$	0	0.0005	Microcomb intrinsic angular errors would be caused by wafer bow that causes a curling of the final combs. The worst wafer flatness measured using a Hartmann metrology tool was $5 \mu\text{m}$ over the its length a 10 mm half period. The angular error is therefore $\left(\frac{5 \times 10^{-3}}{10}\right)$.
$\theta_Z(\text{rad})$	0	0.0005	Same description as $\theta_{Y_{\text{random}}}$

Table 2.5: Random translational and angular errors in the stack concept CS_2 .

middle comb structural loop nearly mirrors the one already found so the errors are nearly identical.

The preliminary error budgeting for the vertical air-bearing design was also undertaken. The combs used are identical so the random and systematic error from the air-bearing CS_1 to CS_2 are identical. However, the errors from the reference frame to CS_1 are slightly different in two respects:

1. Since the carriage will be mounted perpendicularly directly to a smooth granite bearing way as in Figure B-6 (See Appendix B, page 159), there will be no contribution as before from a non-flatness of the *bottom* of the reference block towards the non-perpendicularity of the combs to the flat as in the in the stack design.[‡] This random angular error about the X axis will then be only:

$$\theta_{X\text{random}} = \sqrt{\left(\frac{25.4 \times 10^{-3}}{120}\right)^2 + \left(\frac{1}{10000}\right)^2} = 0.0002 \text{ rad.} \quad (2.16)$$

2. In the vertical air-bearing concept, the reference combs would not be independently actuated. They would initially be driven until contact with the flat occurred. They would then be glued to the carriages. To move the combs out of position, the *carriage* would be released from its vacuum seal and slid down the bearing way. This effectively eliminates the systematic error in the comb placement against the flat by repeatably imparting nearly exactly the same force to each comb. Thus, the systematic error for the stack design from CS_R to CS_1 in the Y direction is zero.

These errors have been tallied in error propagation spreadsheets [19] and the totals have been calculated. Additional details are available in Appendix C, page 161. The overall systematic and random errors for the bottom comb tooth location on both concepts is shown in Table 2.6. Only the sensitive Y direction errors are shown in the

[‡]The angular error in the flatness of the bottom of the reference block should not be multiplied by half the height of the flat (vertical distance from CS_R to CS_1) to determine the error in the sensitive Y direction for the top microcomb. This is because the lid rests on the reference block via kinematic couplings in the stack concept, which are balls resting in vee-blocks. These balls do not transmit the angular error of the surface to the lid and its attached combs.

	Average Sum and RSS Random Errors (μm)	Net Total Systematic Errors (μm)
Stack Concept	1.9	0.3
Air-Bearing Concept	1.8	0.0

Table 2.6: Preliminary error budget results for random and systematic error contributions in the stack and vertical air-bearing concepts. The errors shown are in the sensitive Y direction only; errors in the non-sensitive directions are available in Appendix C.

	Original reference comb	Redesigned reference comb
Y axis comb error contribution	$H \sin \theta_X + L(1 - \cos \theta_X)$	$L(1 - \cos \theta_X)$
Overall Y axis random error (μm)	1.9 (stack) 1.8 (vert air brng)	0.7

Table 2.7: Mathematical expression for the error contribution in the sensitive Y direction from the microcomb pitch along with the overall Y direction error.

table since the error motions of the microcomb teeth in the X and Z directions are inconsequential at the magnitudes shown in the complete spreadsheets in Appendix C. Table 2.6 shows that we should expect similar accuracy for both designs. This issue and the design selection is explored in the next subsection.

There are two sources of error which contribute substantially to the error budget results. The first source stems from the perpendicularity of the combs to the reference flat. For example, if the random angular error of the CS_1 frame about the X axis is reduced by half, the overall errors are reduced by nearly half. Secondly, the 5.5 mm vertical distance from contact point between the comb and flat to the contact point between the comb and foil (Z direction from CS_1 to CS_2) acts as a lever arm for amplifying the comb-to-flat perpendicularity error. This Abbe, or sine, error can be eliminated entirely if the combs are redesigned to make the comb-to-flat contact point collinear with the comb-to-foil contact point in the direction of the comb's axis. This error and the proposed solution are shown graphically in Figure 2-16. Table 2.7 details the mathematical advantage of this redesign.

The error budget thus illuminated this large contribution to the foil alignment

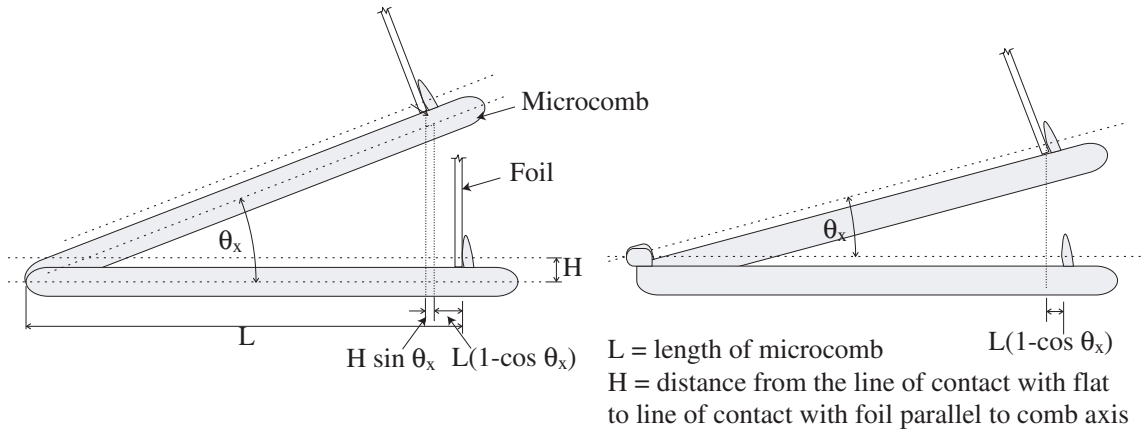


Figure 2-16: Schematic of original reference comb (*left*) and redesigned comb (*right*). The error in the position of the comb's tooth is a function of its non-perpendicularity to the reference flat. In the original design, the comb's contact point with the flat is not aligned with the foil contact point in the direction of the comb's axis. The separation between these lines of contact is magnified by $\sin \theta_X$. This term vanishes when the separation equals zero in the redesigned comb.

error. The redesigned microcombs are shown in Figure 2-17. Note that in this new design, the comb/flat contact point (location of CS_2) is collinear with the comb/foil contact point (location of CS_1). The spring comb design remains unchanged.

2.5.3 Cost/performance analysis

In addition to the preliminary error budget, cost performance curves and were created to best understand the implications of the error budget and help with concept selection.

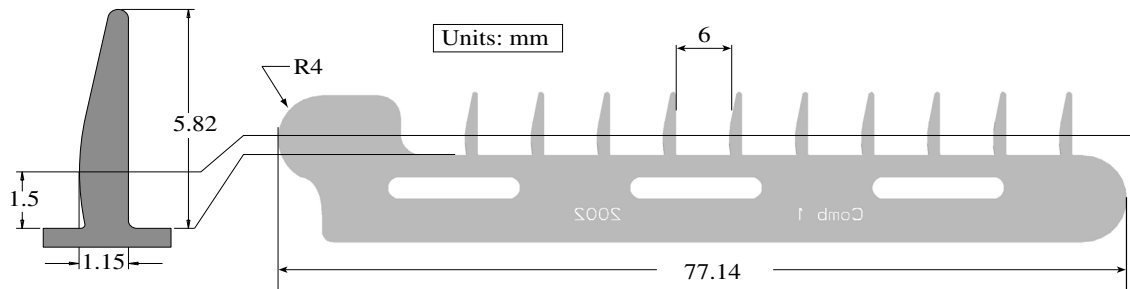


Figure 2-17: The redesigned microcomb eliminates Abbe error. The comb/flat contact point (location of CS_1) is collinear with the comb/foil contact point (location of CS_2). Compare this reference comb's dimensions with the previous generation of reference comb in Figure 2-8 on page 43.

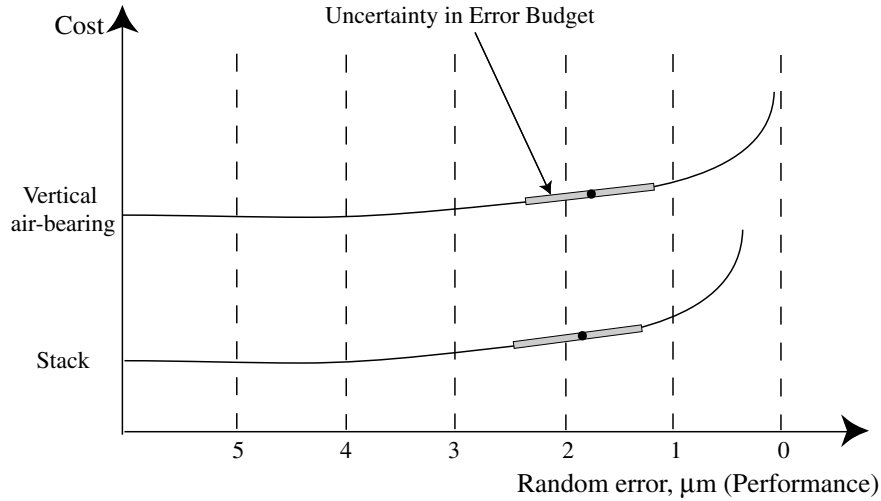


Figure 2-18: The cost/performance schematic illustrates that the theoretical marginal performance improvement for the air-bearing concept may not be worth the additional cost as compared to the stack design. The cost grows exponentially as the desired random error approaches zero; part tolerances during manufacture would drive this behavior.

To blindly choose the vertical air-bearing design over the stack concept because of its marginally better performance in the preliminary error budget analysis would be naive; there are many other factors to consider. Foremost, regarding the error budget, there is some uncertainty in determining the quantitative values for each type of error. Although this uncertainty is hard to quantify, it was estimated to be at least $0.5 \mu\text{m}$. The cost to implement the air-bearing concept would almost certainly be higher, owing to the pneumatic system impact on part design and infrastructure. These considerations are depicted in Figure 2-18.

Other considerations when choosing the final design are first indicated on the Pugh chart on page 52. The time to manufacture the air-bearing concept will be longer. Casting the carriages, for example, will require longer lead-time than milling the stack concept parts. For this work, Dover Precision Instrument Corporation in Westboro, MA, and Alexander Slocum were willing to donate an existing bearing way if the vertical air-bearing concept was selected. Unfortunately, this 500 lb. granite slab with angled magnetic preload design [20] was considered too large for our application. Lastly, the complexity of the air-bearing concept was a drawback. A pulley system or

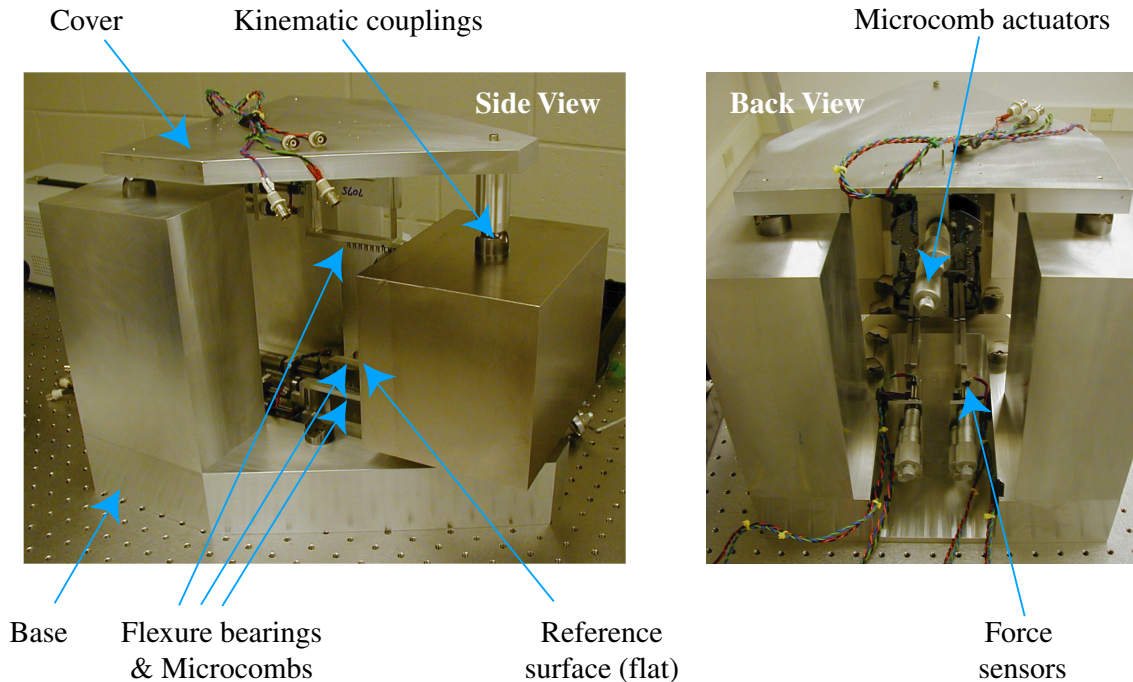


Figure 2-19: Foil optic assembly truss. The flight module is not inside of the assembly tool for this picture. Tests on this assembly truss were performed with only three comb sets instead of six as manufactured. Six will be necessary to distort a cylindrical foil into parabolic or hyperbolic shapes, but only three are necessary to locate a plane.

similar preload scheme would be required, for example, to counterbalance the weight of the carriages. Considering all of these factors, the stack design was selected and pursued.

2.6 Final design

The second-generation assembly truss is shown in Figure 2-19. Four key features shall be discussed in more detail. The reference flat, kinematic couplings, flight module, and flexure bearing assemblies serve critical roles in this device. The flexure bearing assembly was modeled to predict the dynamic performance of the system.

2.6.1 Reference flat

The reference flat is shown in relation to the assembly truss in Figure 2-20. This part is a solid block of Aluminum 6061-T6 with 0.005 inches of electroless-plated nickel

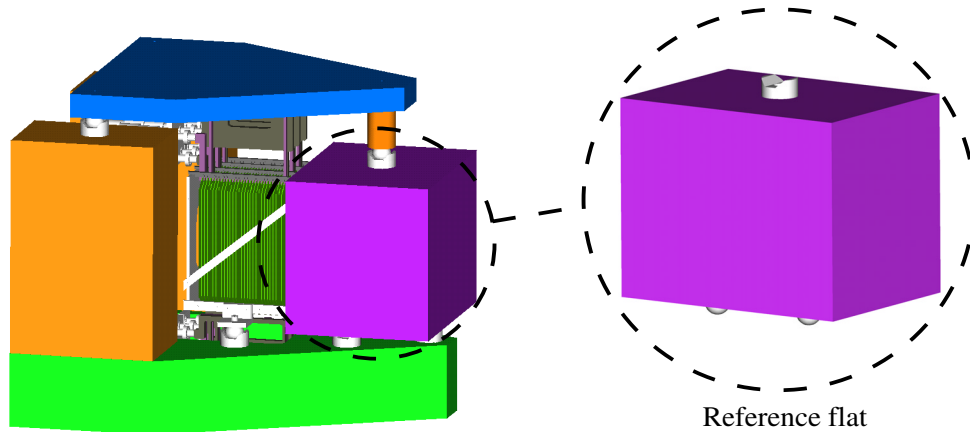


Figure 2-20: The reference flat is shown in relation to the assembly truss.

on its surface. The nickel is much harder than the aluminum to resist scratching during use. One face of the block is lapped and optically polished to $1\ \mu\text{m}$ flatness peak-to-valley (P-V).[§] Kinematic couplings on the bottom and top of the block ensure repeatable alignment with the base and lid, respectively.

2.6.2 Kinematic couplings

Ball and vee-block kinematic couplings were selected to allow repeatable placement of the flight module onto the base, the reference flat onto the base, the cover onto the reference flat. One of these couplings is shown in Figure 2-21. Kinematic couplings of this design and application have sub-micron repeatability [21]. The vee-blocks are arranged such that the lines formed by the intersection of their respective faces intersect at the centroid of the triangle whose vertices are formed by the vee-blocks themselves. This ensures uniform load distribution and prevents the faces from over-constraining the parts from misalignment.

2.6.3 Flight module

The flight module, shown in Figure 2-22, is designed to hold thirty foils loosely in a set of “coarse combs” before assembly. The microcombs manipulate the foils into

[§]A flatness of $0.1\ \mu\text{m}$ was specified for the polishing process. Unfortunately, a manufacturing error occurred.

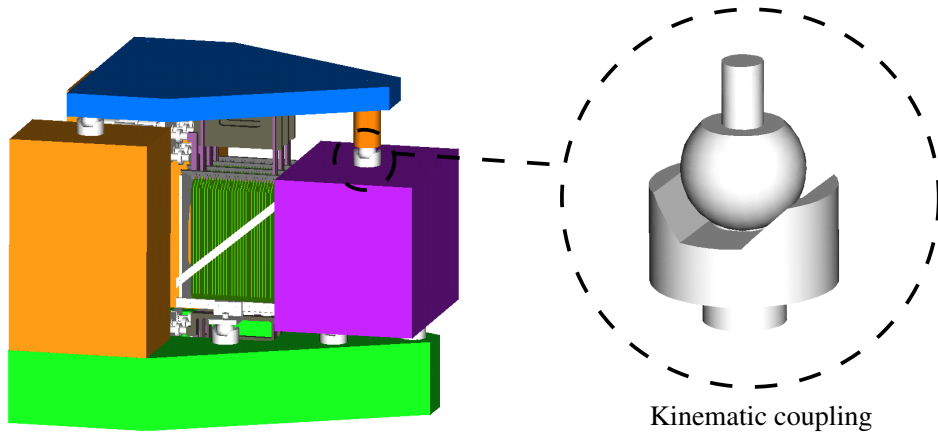


Figure 2-21: The kinematic coupling ball and vee-block components are shown. These were located at nine distinct locations on the truss to repeatably orient the reference flat, cover, and flight module.

their aligned locations within the oversized slots of these coarse combs. The flight module includes kinematic balls for the repeatable alignment with the base. After the foils are aligned, glue is injected into holes on the coarse combs to secure the foil in place. This gluing procedure is depicted in Figure 2-23.

The final and most critical subsystem of the assembly truss is the flexure bearing assembly. The next section elaborates on its purpose and design.

2.6.4 Flexure bearing assembly

The heart of the assembly truss is the flexure bearing assembly, shown in Figure 2-24. The flexure bearings provide independent, hysteresis free, friction free support for the reference combs to make contact with the reference flat and for the spring combs to impart forces to the foil. The four bar linkage design of the flexure bearings allows parallel motion between the top and bottom members. In fact, a parasitic pitch error in this motion is virtually eliminated with proper selection of the position of the driving point [22]. The flexures are actuated at half of their height by differential screw micrometers (Mitutoyo, model 110-102) which have a resolution of $0.1 \mu\text{m}$. This resolution is necessary to achieve the microcomb placement accuracy of $1 \mu\text{m}$. Force sensors (Honeywell, sold by Cooper Instruments, models LPM 560, LPM 562)

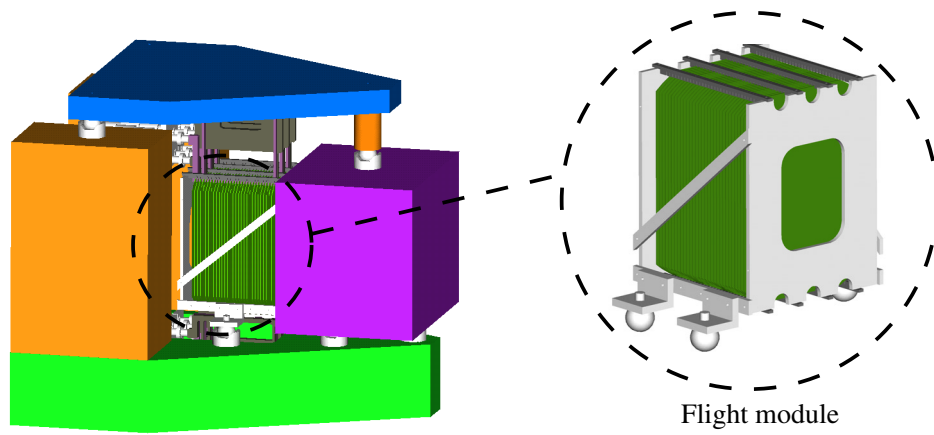


Figure 2-22: Flight module containing optic foils is shown. This prototype module is designed to hold thirty foils and fit into the assembly truss.

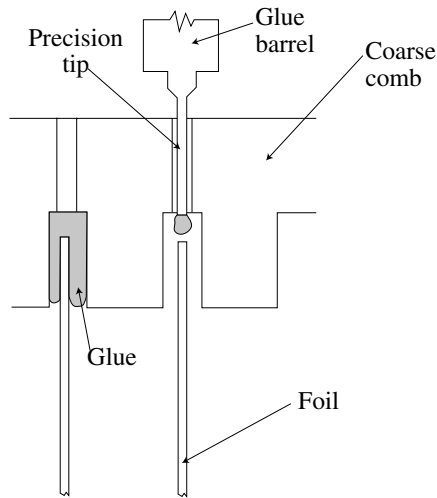


Figure 2-23: Cross-section view of an optic foil being glued to a coarse comb. This procedure is performed inside the assembly truss after the foils are in their aligned positions.

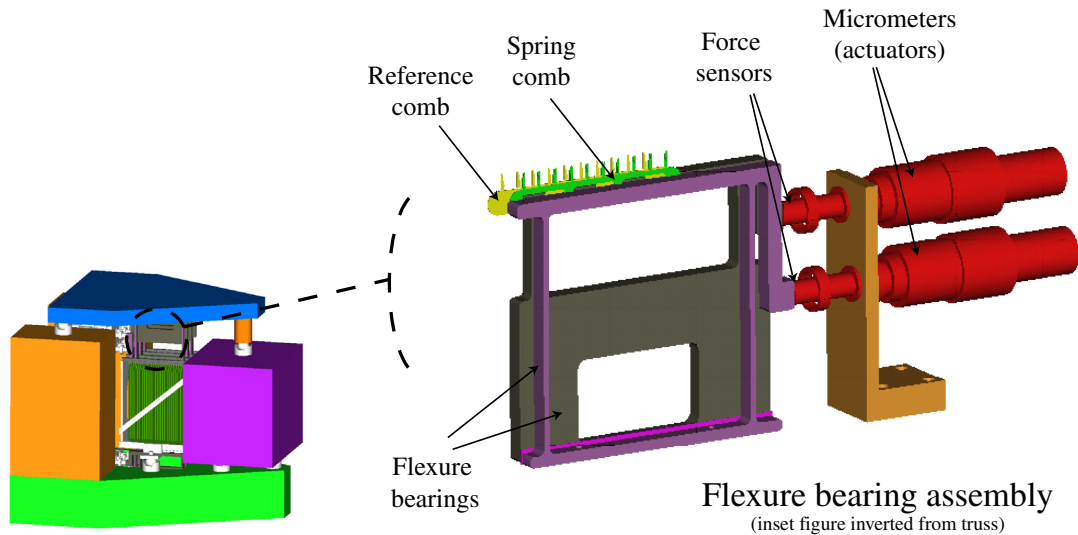


Figure 2-24: The flexure bearing assembly contains microcombs, flexure bearings, force sensors, and micrometers.

are placed in between the micrometers and the flexure bearings. They are relatively insensitive to off-center plunger loading and have rated loads of 4.9 N and 14.7 N for the reference and spring flexure bearings, respectively. Calibration lines are in Appendix D, page 171. These sensors allow the operator to detect when contact with the reference flat occurs, since then the stiffness of the system changes. Before contact, the force per unit displacement is a function of the stiffness of the flexure bearings, force sensors, micrometers, and micrometer holders. After contact, there is an additional stiffness component due to the Hertzian deformation of the microcomb.

Mathematical modeling

The flexure bearing assembly was modeled to design it for desired performance. Figure 2-25 shows the mathematical model. This modeling was undertaken for two purposes: (1) The system stiffness will change after contact with the reference flat occurs. We would like to design the flexure bearing assembly so that this change in stiffness is well defined and can be recognized when it occurs. For this, we will need to model the system stiffness before and after contact. (2) The micrometer actuator drives the system. Its displacement is x_1 in Figure 2-25. The resulting displacement

of the microcomb attached to the flexure bearing, x_2 , is needed. If the micrometer is actuated by $1 \mu\text{m}$, for example, how far does the microcomb move before and after contact? This is important because the micrometer holder should act as a relief valve, flexing backwards after the comb makes contact so that the comb nose is not fractured. We begin with the mathematical modeling, then proceed to analyze the design stiffnesses. Two competing flexure bearing designs will be evaluated mathematically and experimentally.

Since determining when contact with the reference flat has occurred is essential for system accuracy, we shall need to estimate the stiffness of this flexure bearing assembly before and after contact with the reference flat. We can then predict the expected change in the slope of the stiffness measurements as we vary parameters in the system such as physical dimensions and materials. From Figure 2-25, we can see that the equivalent stiffness before contact, $k_{<c}$, can be determined by four springs in series ($k_{\text{hertz}} = 0$ before contact). Mathematically, we have

$$k_{<c} = \frac{1}{\frac{1}{k_{\text{holder}}} + \frac{1}{k_{\text{mic}}} + \frac{1}{k_{\text{sensor}}} + \frac{1}{k_{\text{reflex}}}}. \quad (2.17)$$

After contact, the Hertzian stiffness of the reference comb to reference flat must be considered, so we have

$$k_{>c} = \frac{1}{\frac{1}{k_{\text{holder}}} + \frac{1}{k_{\text{mic}}} + \frac{1}{k_{\text{sensor}}} + \frac{1}{(k_{\text{reflex}} + k_{\text{hertz}})}} \quad (2.18)$$

where $k_{>c}$ is the equivalent stiffness after contact.

Next, we model the ratio of the micrometer displacement, x_1 , to the microcomb displacement, x_2 . This “transmission ratio” of output over input will be useful in understanding the resolution of the micrometer motion before and after contact. The model can be broken down as shown in Figure 2-26. Application of force, F , from the micrometer allows us to write the force balance for each segment as

$$F = \frac{1}{\frac{1}{k_{\text{holder}}} + \frac{1}{k_{\text{mic}}} + \frac{1}{k_{\text{sensor}}}} (x_1 - x_2) \quad (2.19)$$

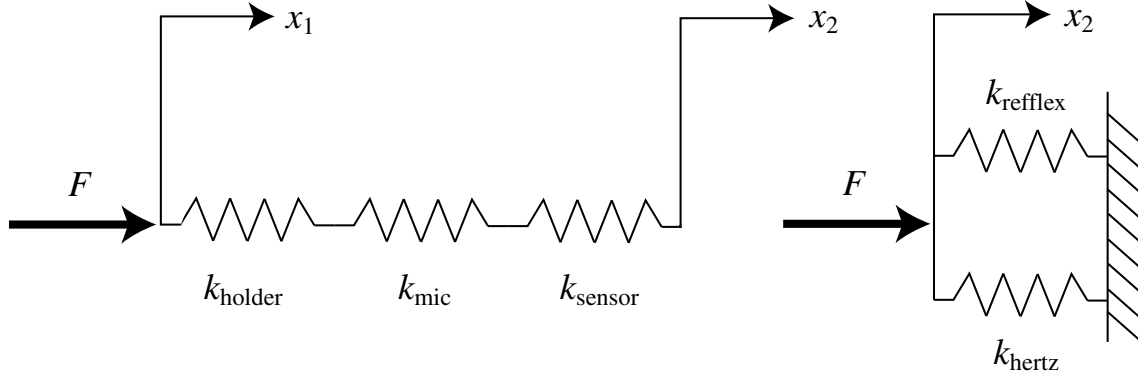


Figure 2-26: Separating the flexure bearing model into two parts permits the evaluation of the transmission ratio between the micrometer displacement, x_1 , and the microcomb displacement, x_2 .

and

$$F = (k_{\text{reflex}} + k_{\text{hertz}}) x_2. \quad (2.20)$$

Combining and solving for the transmission ratio, x_2/x_1 gives

$$\frac{x_2}{x_1} = \frac{\frac{1}{\frac{1}{k_{\text{holder}}} + \frac{1}{k_{\text{mic}}} + \frac{1}{k_{\text{sensor}}}}}{k_{\text{reflex}} + k_{\text{hertz}} + \frac{1}{\frac{1}{k_{\text{holder}}} + \frac{1}{k_{\text{mic}}} + \frac{1}{k_{\text{sensor}}}}}. \quad (2.21)$$

The transmission ratio can be calculated before contact by setting $k_{\text{hertz}} = 0$.

We will need to find numerical values for these stiffnesses to proceed. The force sensor that is positioned between the micrometer and reference comb's flexure deflects $30 \mu\text{m}$ under the rated load of 4.9 N . The sensor stiffness is therefore

$$k_{\text{sensor}} = \frac{F}{\delta} = \frac{4.9 \text{ N}}{30 \mu\text{m}} = 1.64 \times 10^5 \text{ N/m}. \quad (2.22)$$

The micrometer is the stiffest component in the structural loop. The stiffness is effectively given by its steel shaft. Therefore,

$$k_{\text{mic}} = \frac{AE}{L} = \frac{\pi r^2 E}{L} = \frac{(\pi)(4 \text{ mm})^2 (2 \times 10^{11} \text{ N/m}^2)}{25 \text{ mm}} = 4.02 \times 10^8 \text{ N/m} \quad (2.23)$$

where A is the cross-sectional area, E is the Young's modulus, r is the beam radius, and L is the beam length. Both the micrometer holder and the reference flexure act

as cantilevered beams, so their stiffnesses are given by

$$k_{\text{holder}}, k_{\text{reflex}} = \frac{3EI}{L^3} \quad (2.24)$$

where I is the moment of inertia

$$I = \frac{Wt^3}{12} \quad (2.25)$$

and W is the width of the beam. So now we can choose W , t , L , and E to get a well-defined change in slope. One may note that the reference flexure design is essentially two cantilevered beams in parallel. Therefore, to calculate k_{reflex} , we just consider the stiffness for a single vertical beam and double it.

Calculating the stiffness of the microcomb contact with the reference flat, k_{hertz} , is a little more challenging, but it is deterministic. We must consider Hertz theory [17], since we have contact between curved surfaces. In this derivation, the surface of the reference microcomb in contact with the flat will be approximated as a cylinder of length L and diameter d_1 loaded by distributed force F/L . The contact area between this cylinder and the flat is a rectangle of length L and width $2b$, where b is

$$b = \sqrt{\frac{2Fd_1d_2}{\pi LE_e(d_1 + d_2)}}. \quad (2.26)$$

In evaluating this equation, the microcomb has diameter d_1 of 8 mm and the contact patch length is 40 μm , which is 10% of the microcomb thickness as determined by Mongrard [1, page 99]; d_2 is the reference flat diameter which is much, much greater than d_1 . E_e is the equivalent modulus of elasticity of the system based on the elastic moduli and Poisson ratios of the two materials in contact:

$$E_e = \frac{1}{\frac{1-\eta_1^2}{E_1} + \frac{1-\eta_2^2}{E_2}}. \quad (2.27)$$

The materials used are single crystal silicon and nickel. Their moduli are 160 GPa and 200 GPa, respectively; their Poisson ratios are 0.215 and 0.310. We calculate the deflections for the cylinder and flat separately, then sum them. The deflection for the

cylinder is

$$\delta_{\text{cyl}} = \frac{2F}{\pi L E_e} \left[\ln \left(\frac{2d_1}{b} \right) - \frac{1}{2} \right]. \quad (2.28)$$

In evaluating this expression, we assume E_2 is infinite in Equation 2.27. This substitution leads to a unique E_e and subsequent b . For the deformation of the flat:

$$\delta_{\text{flat}} = \frac{2F}{\pi L E_e} \left[\ln \left(\frac{2d_1}{b} \right) - \frac{\eta}{2(1-\eta)} \right]. \quad (2.29)$$

In this case, E_1 is infinite in Equation 2.27 resulting in another value for b . The total deflection of the system composed of one flat and one cylinder is thus

$$\delta_{\text{sys}} = \delta_{\text{cyl}} + \delta_{\text{flat}}. \quad (2.30)$$

And lastly, we can find the stiffness, k_{hertz} , as

$$k_{\text{hertz}} = \frac{F}{\delta_{\text{sys}}}. \quad (2.31)$$

This stiffness is not constant as it is for the other components in the flexure bearing assembly.

Two different flexure bearing assemblies were designed and manufactured. Aluminum 6061-T651 was selected for its low cost, availability, and ease of machining. The -51 designation indicates that the aluminum is stress-relieved to prevent warping due to the release of internal stresses during manufacture. The two assemblies' dimensions are shown in Table 2.8 along with material properties. In the chronologically first design, design 1 in Table 2.8, the dimensions of the micrometer holder and reference flexure were selected considering several factors. The reference flexure should be able to extend the 400 μm distance to the reference flat without yielding so that its motion is repeatable. At this deflection, the designed reference flexure has a yielding factor of safety of 9.92. In design 2 in Table 2.8, the dimensions were modified primarily so that the change in slope of the stiffness plot before and after contact would unmistakably provide sub-micron resolution. The thinness of the refer-

Design	1	2
Reference flexure design		
L_f	30.40 mm	30.40 mm
t_f	1.50 mm	0.65 mm
W_f	6.35 mm	6.35 mm
k_{reflex}	1.07×10^5 N/m	8.69×10^3 N/m
Micrometer holder		
L_h	60.0 mm	60.0 mm
t_h	5.0 mm	7.0 mm
W_h	25.4 mm	25.4 mm
k_{holder}	2.57×10^5 N/m	7.06×10^5 N/m

Table 2.8: Dimensions for the two manufactured flexure bearing assemblies and calculated stiffnesses.

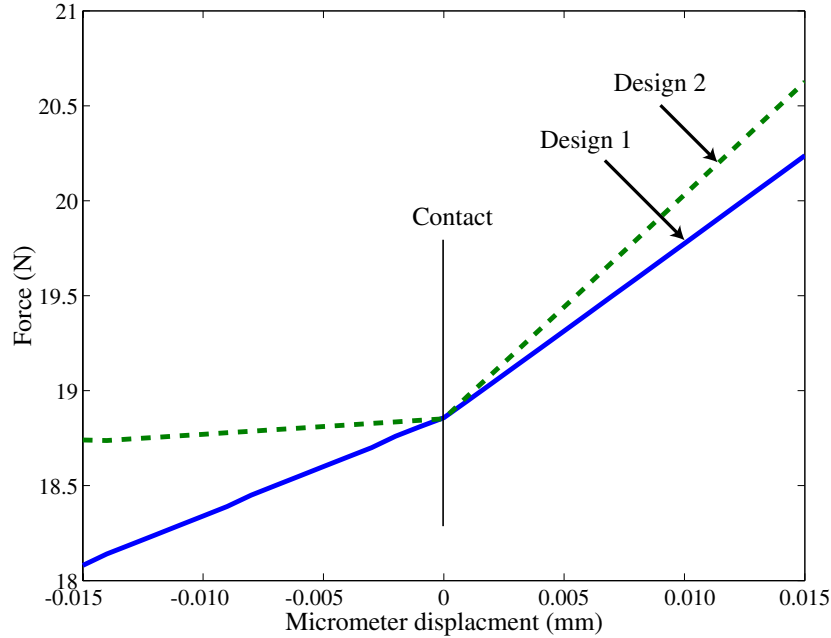


Figure 2-27: The modeled stiffnesses for the two flexure bearing designs before and after contact with the reference flat. The slope after contact is slightly non-linear due to the Hertzian contact stiffness.

ence flexure wall, t_f , was reduced until limited by milling machine capabilities. This thinner flexure will have an even higher safety factor against yielding for the same displacement. The resulting stiffness change prediction for these two systems from Equations 2.17 and 2.18 are shown in Figure 2-27. This theory will be compared with experimental data in the next section.

From these plots, we note that contact should be detectable immediately after the abrupt transition in slope. This should occur for a micrometer actuator displacement of less than $3 \mu\text{m}$. This corresponds to a force at the microcomb/reference flat interface of approximately 0.3 N . We can compute the average value of k_{hertz} from $0\text{--}0.3 \text{ N}$ to be $8.70 \times 10^5 \text{ N/m}$ from Equation 2.31. The Hertzian compression of the microcomb nose can also be evaluated from this expression as $\delta_{\text{sys}} = 0.3 \mu\text{m}$.

The transmission ratios of the two designs will be considered to decide on which flexure bearing assembly is best. Using Equation 2.21 and the component stiffnesses, we can compare the flexure bearing assemblies before and after contact for design 1 and 2 in Table 2.9. The transmission ratio for design 1 is smaller. If this flexure

	Before contact	After contact
	x_2/x_1	x_2/x_1
Design 1	0.484	0.093
Design 2	0.939	0.132

Table 2.9: The transmission ratio, x_2/x_1 , is shown for the two flexure bearing designs before and after microcomb contact with the reference flat.

bearing assembly is actuated by the micrometer resolution of $0.1 \mu\text{m}$ after contact, the microcomb will only move into the reference flat by 9.4 nm. Although the transmission ratio for design 2 is larger, we still have a moderate microcomb resolution after contact of 13.2 nm. Considering the abrupt, easily recognizable stiffness transition for design 2 shown in Figure 2-27, the decision was made to go with design 2. This flexure bearing assembly will still allow the micrometer holder to act as a “relief valve” to prevent microcomb damage while clearly conveying the contact to the operator.

The Hertzian stress in the microcomb nose was compared to the material strength to ensure that the comb nose will not fracture before contact is recognized. This is very important considering that the silicon will not exhibit any plastic deformation below 800°C [23] and brittle fracture will dominate. Using the same variables as in the previous Hertzian deformation derivation, the maximum contact pressure, q , in this cylindrical contact case is

$$q = \frac{2F}{\pi bL} \quad (2.32)$$

and the maximum shear stress that occurs inside the microcomb cylinder is then

$$\tau_{\max} = 0.3q \quad (2.33)$$

We can therefore evaluate the force necessary to fracture the microcomb nose. Silicon has a tensile strength of 566 MPa. The shear strength will be half this value [24]. Substituting Equation 2.26 into the above two equations allows us to solve for the force required to fracture the silicon, 4.7 N. Note that the shear stress goes with the square root of F .

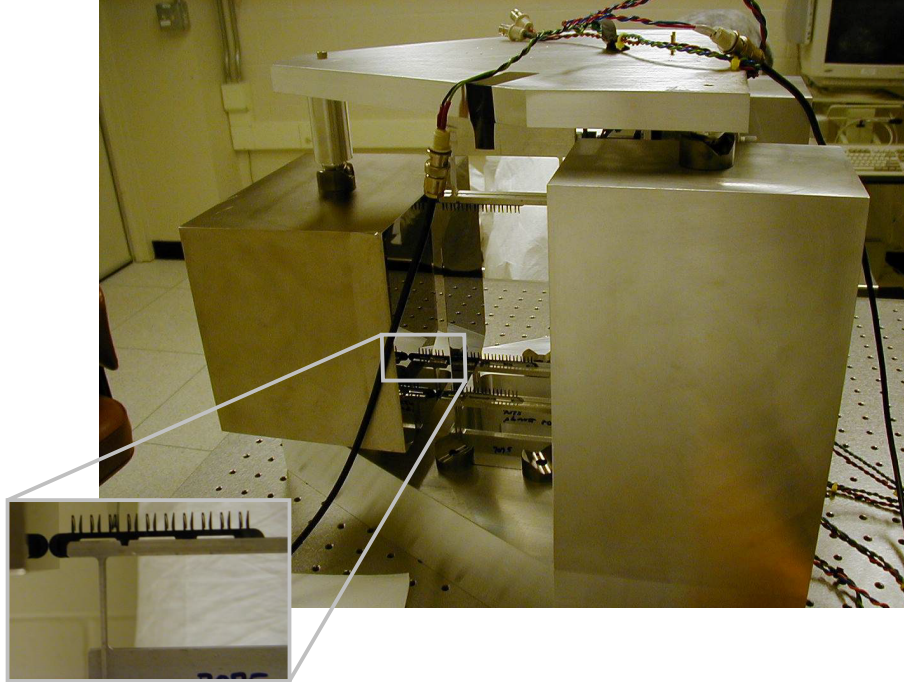


Figure 2-28: Assembly truss during testing with reflective optic foil inserted. The microcomb is in contact with the reference flat (*inset*).

2.7 Microcomb contact with reference flat, experimental

The flexure bearing assembly is actuated until the microcomb makes contact with the reference flat, as shown in Figure 2-28. For both flexure bearing assembly designs, the stiffness plots reveal when contact with the reference flat has occurred. Two representative data sets are shown in Figure 2-29. At contact, there is a smaller change in slope for design 1 than for design 2. With the improved second design, the contact location can easily and repeatably be resolved to 1 μm micrometer displacement. To compare with the stiffness theory from the previous section, the force per displacement slopes from several design 1 and design 2 flexure bearing assemblies were measured. Table 2.10 shows the results. The theoretical and experimental values compare reasonably well. One factor which may account for the deviation is the flexure bearing manufacturing process variation.

Another contact test was conducted to attempt to fracture a microcomb to verify

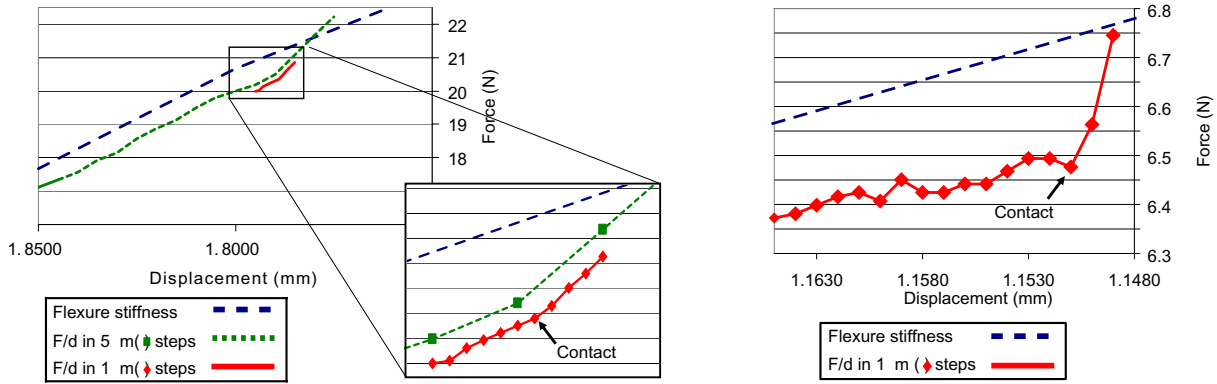


Figure 2-29: Experimental data from flexure bearing assembly design 1 (*left*) and design 2 (*right*). In both designs, contact with the reference flat is observable. The second design, with its lower stiffness reference flexure, has a more dramatic change in slope.

		Before contact stiffness, $k_{<c}$ (10^3 N/m)	After contact stiffness, $k_{>c}$ (10^3 N/m)
Design 1	Theory	51.7	90.8
	Experimental	60.5	121.0
	% Difference	17%	33%
Design 2	Theory	8.2	116.0
	Experimental	10.5	109.8
	% Difference	29%	5%

Table 2.10: Stiffness measurements from flexure bearing assembly design 1 and 2 are compared with theory.

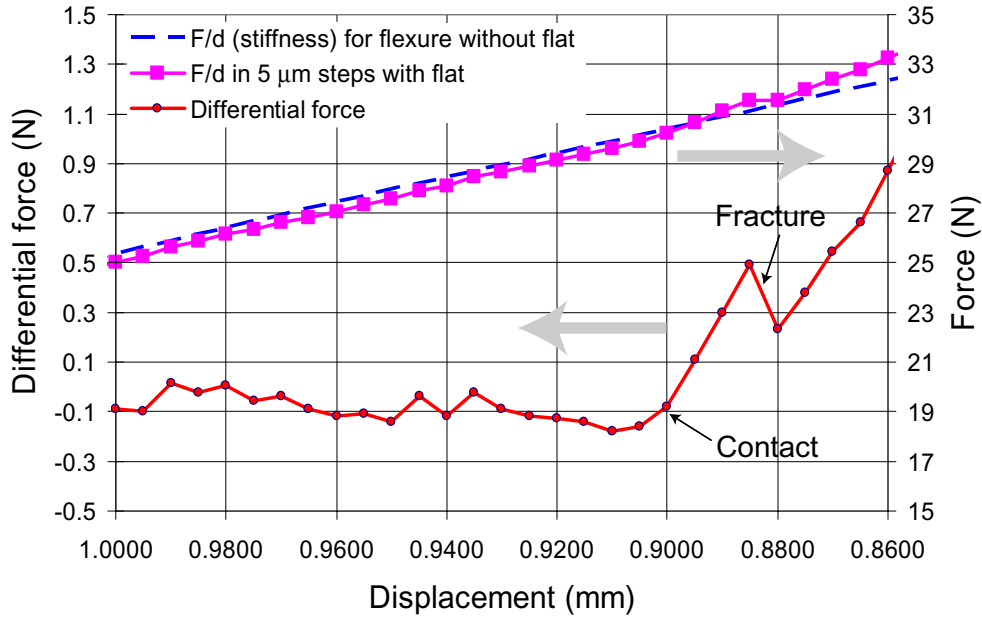


Figure 2-30: Differential force data reveals the force at the comb/flat interface. Fracture occurs when the Hertzian shear stress in the comb exceeds the silicon shear strength.

the Hertz theory. In this test, a microcomb was driven into the reference flat until fracture had occurred visually. Figure 2-30 shows the stiffness data along with a difference plot. This difference plot represents the force that the microcomb nose feels. Fracture should be accompanied by a significant force drop. Microscope pictures (See Figure 2-31) confirmed this hypothesis. This fracture occurs at a displacement of about $15\ \mu\text{m}$ after contact. The differential force at this location is only $0.5\ \text{N}$ instead of the $4.7\ \text{N}$ predicted from Hertz theory on page 79. There are likely some other mechanisms at work to fracture the comb, such as imperfections in the silicon due to over-etching. Regardless, the operator of the assembly truss should be confident that the comb will not fracture until around $15\ \mu\text{m}$ of micrometer displacement after contact—typically only $1\text{-}2\ \mu\text{m}$ are needed to verify the change in stiffness. This corresponds to a differential force of approximately $0.1\ \text{N}$.

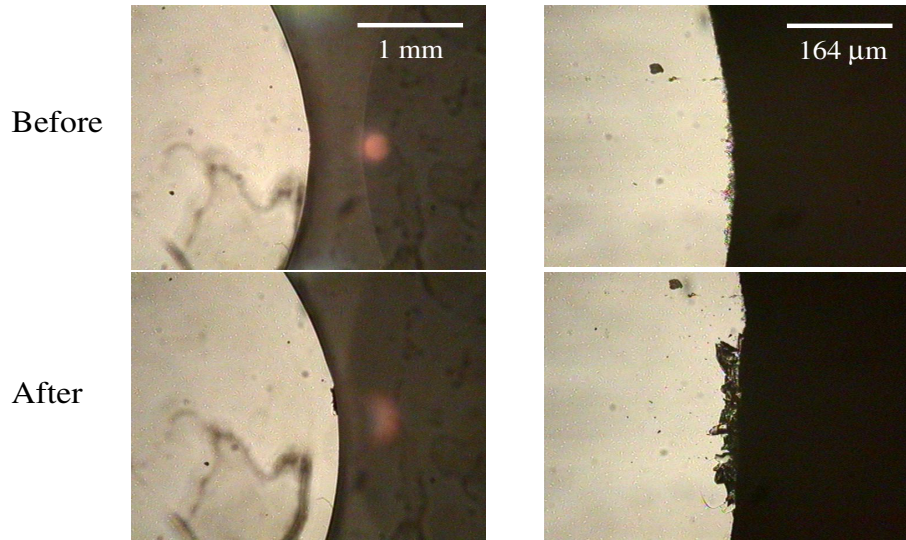


Figure 2-31: Following the comb damage test, magnification clearly reveals the fractured surface at the comb nose.

2.8 Repeatability testing

Numerous tests have been performed on the assembly truss to determine its ability to meet precision foil alignment goals of $1\ \mu\text{m}$. An autocollimator (Newport, model LAE500H) was used to measure the angular errors of a foil located in a “slot,” which were then converted to displacements. Previous experiments performed on a static breadboard test assembly system have demonstrated a $1\ \sigma$ mounting slot repeatability error of about $0.11\ \mu\text{m}$ in both axes [25]. This previous research defined repeatability as the standard deviation of a set of measurements collected by successively measuring, lifting, and replacing a fused-silica plate against fixed reference microcomb teeth. This test was repeated with the new design and the data shows less than $0.05\ \mu\text{m}$ for both pitch and yaw.

The current research involves a dynamic assembly truss, which strives to mimic the actual telescope foil alignment procedures. A static test was performed to obtain a baseline for repeatability. In this test, an optic foil was inserted into a slot, measured, then completely removed from the truss, reinserted, and remeasured. All mechanical parts on the truss were static. To test dynamic slot repeatability, two tests were performed. In the first test, the truss lid was removed and replaced as would be

required for actual flight module assembly. The combs were not moved relative to the lid or base. The second dynamic test, which comes closest to actual flight module assembly, includes microcomb actuation to the planar reference flat in addition to lid reinstallation.

The procedure for this second dynamic test (See Figure 2.8) is as follows: a single foil was slid from the side of the assembly truss into the microcomb slot. The reference microcombs were then driven into contact with the reference flat. The pitch and yaw of the foil were recorded with the autocollimator zeroed to the reference flat. The combs were then retracted, and the assembly truss lid was raised and replaced. The lid was tapped by hand to settle the kinematic couplings. The reference combs were then driven back into contact with the flat, and the foil angle was recorded. This procedure was repeated three times. The autocollimator has a resolution of $0.1 \mu\text{rad}$ in pitch and yaw; instrument drift was subtracted out. The autocollimator measurements ranged by approximately $5 \mu\text{rad}$ during testing. To compensate, five data points were manually collected and averaged at each foil position. During settling of the kinematic couplings, the lid centroid typically moved about $1 \mu\text{m}$. The device was inclined slightly (20 mm height over 300 mm length) to allow gravity to preload the foil against the reference teeth. Spring combs were not used during this testing since gravity provided the necessary preload and we wanted to isolate the variables affecting repeatability. This procedure was performed for both a 3 mm thick quartz plate coated with 1000 \AA of aluminum and a 0.4 mm thick silicon wafer. Both foils were of size $140 \times 100 \text{ mm}^2$. The two were studied to understand the repercussions of thin foil deformation. Results from these tests are summarized in Table 2.11.

Results from the static test indicate that the repeatability of fully replacing an optic foil on the microcombs is approximately $0.35 \mu\text{m}$ in both axes. The second test includes the lid kinematic coupling repeatability error in addition. In this test, gravity deformation of the thin silicon wafer may account for the difference between the substrate results. The final test effectively cancels out the kinematic coupling error in the sensitive direction by actuating the combs to the reference flat. Hence, in the final test, the optic foil placement repeatability appears to dominate. Comparing the

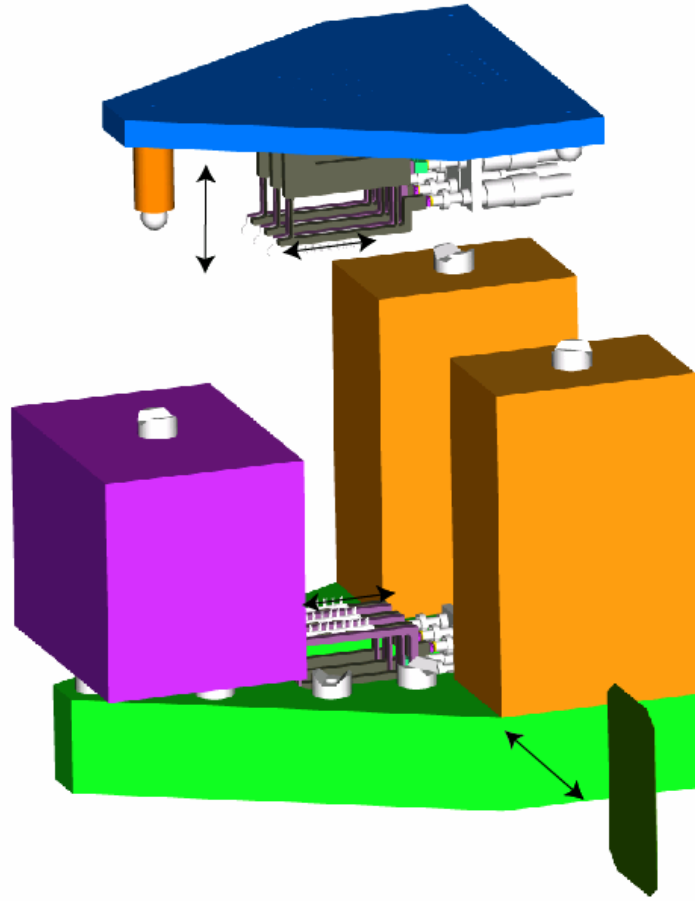


Figure 2-32: Repeatability testing procedure. A single foil is slid from the side of the assembly truss into the microcomb slot. The reference microcombs are then driven into contact with the reference flat. Angles of the optic are recorded. The combs are then retracted, and the assembly truss lid is raised and replaced.

single slot repeatability test	displacement error, one σ (μm)			
	0.4 mm-thick silicon wafer		3 mm-thick fused-silica plate	
	pitch	yaw	pitch	yaw
fixed lid and combs	0.26	0.39	0.59	0.23
dynamic lid, fixed combs	0.83	0.93	0.47	0.40
dynamic lid and combs	0.34	0.36	0.33	0.30

Table 2.11: Assembly truss single slot repeatability results. Displacement error is the displacement of the edge of the foil extracted from its angular error and dimensions.

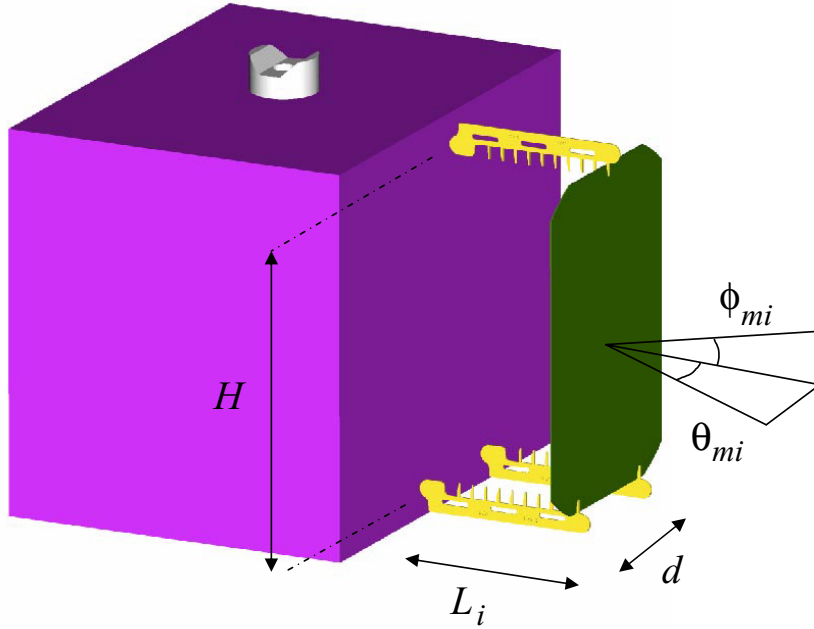


Figure 2-33: Accuracy testing schematic. $d = 55$ mm, $H = 140$ mm.

difference in the final test results for the different foil thicknesses, thin foil deformation does not appear to be a significant contributor to the overall error.

2.9 Accuracy testing

The accuracy of foil placement in the assembly truss has also been measured. In these tests, we compare the angular error of the foil with respect to the reference flat after the microcomb length errors have been subtracted out. This compensation was necessary due to fabrication errors in the microcombs. Other work [16] elaborates on these fabrication challenges. The average systematic angular errors of the previous static breadboard assembly truss have been called “slot-to-reference flat” errors by Mongrard [1]. For these experiments, the 3 mm-thick quartz plate was used as a dummy wafer to measure the system accuracy. Errors due to the thinner silicon foil have been quantified in repeatability testing in Section 2.8.

The accuracy terms we will use are conveyed in Figure 2-33. The terms θ_{mi} and

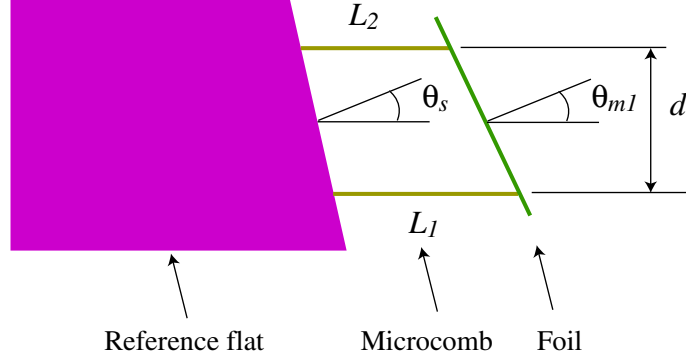


Figure 2-34: Top view of assembly truss showing how the systematic error in yaw, θ_s , is related to the microcomb lengths, L_1 , L_2 , and the measured yaw error of the foil, θ_{m1} .

ϕ_{mi} refer to measured yaw (θ) and pitch (ϕ) of the foil for measurement number i . We seek the average systematic error in the device, θ_s and ϕ_s , converted to linear dimensions, as a measurement of the accuracy.

Unknowns in this analysis include the three microcomb lengths for a given slot, L_1 , L_2 , and L_3 , as well as θ_s and ϕ_s . First we consider the systematic yaw error, θ_s . Figure 2-34 illustrates that this error can be defined as

$$\theta_s = \theta_{m1} - \frac{L_1 - L_2}{d}. \quad (2.34)$$

There are three microcombs and three possible microcomb positions, so six permutations of the combs are possible. This gives the equation

$$Ax = b \quad (2.35)$$

$$\begin{bmatrix} 1 & -1 & 0 & 1 \\ -1 & 1 & 0 & 1 \\ -1 & 0 & 1 & 1 \\ 1 & 0 & -1 & 1 \\ 0 & 1 & -1 & 0 \\ 0 & -1 & 1 & 0 \end{bmatrix} \begin{bmatrix} L_1 \\ L_2 \\ L_3 \\ d\theta_s \end{bmatrix} = d \begin{bmatrix} \theta_{m1} \\ \theta_{m2} \\ \theta_{m3} \\ \theta_{m4} \\ \theta_{m5} \\ \theta_{m6} \end{bmatrix}. \quad (2.36)$$

Since there are only four unknowns, only four equations are required to solve this

		Slot 1 (μm)	Slot 2 (μm)	Slot 3 (μm)
Comb 1	L_1	a	b	c
Comb 2	L_2	$a + 2.78$	$b + 6.85$	$c + 3.16$
Comb 3	L_3	$a + 3.12$	$b + 6.08$	$c + 5.86$

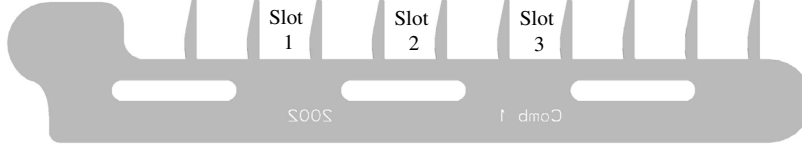


Table 2.12: For the three slots tested, the comb lengths were calculated. These lengths represent the distances from the reference flat/comb contact points to the foil/comb tooth contact points. Only relative lengths can be calculated.

system. Here we retain the six equations to perform a least squares fit to the data as in

$$A^T A x = A^T b. \quad (2.37)$$

In the accuracy testing procedure, the lid was placed on the assembly truss, the foil was inserted, the combs were driven into contact with the flat, and the foil's angular orientation was measured with the autocollimator. The truss was then disassembled, the flexure bearing assemblies were permuted, and the assembly procedure was repeated. Six comb permutations resulted in six foil angular measurements to fill b in Equation 2.35. This entire process was repeated for three different slots in the micro-combs. The resulting systematic yaw error for these three slots is shown along with average value of θ_s in Table 2.13. Equation 2.36 also yields the three comb lengths for the three slots tested. The absolute values can not be found from this mathematics, only the relative lengths. They are given in Table 2.12.

To find the systematic pitch error, ϕ_s , we take a similar approach, shown in Figure 2-35. We derive a similar expression

$$\phi_s = \phi_{m1} + \frac{1}{H} \left(L_3 - \frac{L_1 + L_2}{2} \right). \quad (2.38)$$

This time, there is no difference between the permutations of comb L_1 and L_2 (See

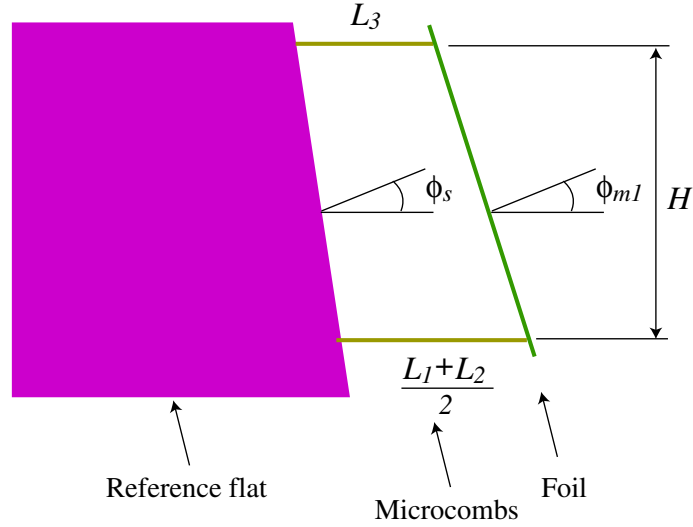


Figure 2-35: Side view of assembly truss showing how the systematic error in pitch, ϕ_s , is related to the microcomb lengths, L_1 , L_2 , L_3 , and the measured pitch error of the foil, ϕ_{m1} .

Figure 2-35), so we only derive three unique equations in the form

$$Cy = f \quad (2.39)$$

$$\begin{bmatrix} 1 & 1 & -2 & 2 \\ 1 & -2 & 1 & 2 \\ -2 & 1 & 1 & 2 \end{bmatrix} \begin{bmatrix} L_1 \\ L_2 \\ L_3 \\ H\phi_s \end{bmatrix} = 2H \begin{bmatrix} \phi_{m1} \\ \phi_{m2} \\ \phi_{m3} \end{bmatrix}. \quad (2.40)$$

Since the comb lengths were found from Equation 2.35, we can solve directly for ϕ_s three times from Equation 2.40. These values were averaged to find the true ϕ_s for each slot. Again this procedure was performed for three slots. The systematic pitch error for these three slots is shown along with average value of ϕ_s in Table 2.13. Discussion of these results follows in Section 2.11.

2.10 Final error budget

The error budget was revisited for the final assembly truss design. This error budget carefully tracked the errors in every part leading from the reference frame to the

	Yaw θ_s (μm)	Pitch ϕ_s (μm)
Slot 1	0.56	-1.84
Slot 2	0.25	-1.84
Slot 3	0.21	-2.34
Avg	0.34	-2.01

Table 2.13: Assembly truss slot accuracy results. Displacement error is the displacement of the edge of the foil extracted from its angular error and dimensions. The errors for three successive slots are shown along with the average systematic angular errors.

Average Sum and RSS Random Errors (μm)	Net Total Systematic Errors (μm)
0.5	0.3

Table 2.14: Final error budget for assembly truss design. Errors shown are in the sensitive Y direction only; errors in the non-sensitive directions are available in Appendix C.

point-of-action, the contact interface between the microcomb and foil. The details are shown in Appendix C, page 161. The results are presented in Table 2.14.

2.11 Discussion and conclusions

The repeatability results will meet the functional requirements for the assembly of foil optics. These $\sim 0.3 \mu\text{m}$ repeatability errors can be further reduced primarily by averaging more autocollimator measurements. Eliminating Hertzian deformations at the comb/reference flat interface and comb/foil interface could also improve the repeatability

The error budget predicts that the expected accuracy of the assembly truss alignment is $0.5 \mu\text{m}$ in pitch and yaw, assuming that systematic error can be recorded and compensated. The errors are nearly identical in the three microcombs due to the symmetric structure of the assembly truss. These results predict that the foil should be aligned in pitch and yaw to within $0.5 \mu\text{m}$ in the as-built machine. This is a purely theoretical estimation, and the errors could be better or worse depending

on the particular milling machine used to make the parts, wafer warp, etc. Comparing them to the accuracy testing results in Table 2.13, we see that the prediction is quite close. In yaw, the difference is less than 200 nm. This indicates that with better manufacturing tolerances and a revised error budget, accuracy should further improve.

In pitch, the experimental errors are greater than the prediction by approximately $1.5 \mu\text{m}$. Some sources of error in the accuracy measurements are that the reference flat was only polished to $1 \mu\text{m}$ P-V due to a vendor mistake and that the quartz optic was only flat to $2 \mu\text{m}$ P-V. The linear systematic errors in Table 2.13 correspond to an angular systematic error of 2.95 arcsec in pitch and 1.13 arcsec in yaw. Therefore, this device meets the 2 arcsec assembly functional requirement for accuracy in yaw. The pitch error is beyond the functional requirement. However, with better polishing of the reference flat and optics with less warp, this error should be within the specification.

The design and performance of the assembly truss meets the outlined functional requirements from Section 2.1, with the notable exception of the systematic pitch error previously described. The assembly tool design integrates an independent flight module, which holds the foils loosely before alignment, and permits a glue adhesive to secure the aligned foils. The closed structural loop is stiff and the metrology frame is effectively isolated. Thin optic foils have been assembled repeatably and these results should hold for the accuracy testing as well. Active feedback in the form of force sensing enables continuous monitoring of the state of the foil boundaries.

Chapter 3

Shack-Hartmann surface metrology system

The surface topography of thin, transparent materials is of interest in many areas. Some examples include glass substrates for computer hard disks, photomasks in the semiconductor industry, flat panel displays, and x-ray telescope optics.

Some of these applications require individual foils to be manufactured with figure errors that are a small fraction of a micron over 10-200 mm lengths. Accurate surface metrology is essential to confirm the efficacy of manufacturing and substrate flattening processes. Assembly of these floppy optics is also facilitated by such a metrology tool. We report on the design and performance of a novel deep-ultraviolet (deep-UV) Shack-Hartmann surface metrology tool developed for this purpose. The use of deep-UV wavelengths is particularly advantageous for studying transparent substrates such as glass which are virtually opaque to wavelengths below 260 nm.

The system has a $143 \times 143 \text{ mm}^2$ field of view at the object plane. Performance specifications include $350 \mu\text{rad}$ angular dynamic range and $0.5 \mu\text{rad}$ angular sensitivity. Surface maps over a 100 mm diameter are accurate to $<17 \text{ nm RMS}$ and repeatable to 5 nm RMS .

3.1 Introduction

Metrology is essential for successfully shaping foil optics. Metrological feedback closes the loop on the manufacturing process. Quantifying figure errors permits the evaluation of process improvements. During assembly, micron level distortions to the foil optic may occur due to gravity or friction. Material thermal expansion mismatch may also cause low spatial frequency distortion. Study of these effects requires a metrology tool with a large viewing area, high angular resolution, and large angular range.

There are three principle functional requirements for this non-null aspheric metrology system, as described by Greivenkamp *et al.* [26]:

- The system must be able to measure the observable output with sufficient angular dynamic range and precision (angular resolution) to record the large amount of asphericity that is present.
- The optic system used to create the observable output must be designed so that no vignetting of the aspheric wavefront occurs.
- The system must be calibrated in order to relate the details in the observable output to the surface under test.

The factory-supplied stock optic foils for our shaping processes typically have low spatial frequency distortions, as observed with other metrology tools.* Stock borosilicate glass sheets (Schott Glas, model D-263) have large distortions, up to 0.6 mm over their 100 mm lengths for 0.4 mm thick foils. By comparison, silicon wafers typically have a flatness of 3 μm over a 10 mm lateral distance, or 0.3 mrad. We seek to flatten these materials to <500 nm over one 100 mm diameter face; this corresponds to a measurement angular sensitivity maximum of 50 μrad over a 10 mm lateral distance. We desire a sensitivity that is five times better than the maximum allowable, so the angular sensitivity functional requirement becomes 10 μrad .

*Interferometric maps and Hartmann tests reveal about three waves per optic length of 100 mm

3.1.1 Metrology technology candidates, research review

Demand for metrology of thin, transparent materials has resulted in many solutions to the problem. Here, we will present technical details of related work and discuss their relative merits and drawbacks.

A key challenge for optical techniques is the measurement of the front surface of the object without the effect of the reflection from the rear surface. We consider phase shifting interferometry (PSI) methods using short coherence length sources in various configurations [27, 28, 29, 30, 31], mathematically deconvolving the contributions of the two reflections using wavelength tunable-sources [32, 33] with some mathematical manipulation [34, 35], spatial separation of the two reflections [36, 37], grating interferometers [38, 39], and use of a diode source and optical path difference (OPD) that is a multiple of the laser cavity length [40]. We also consider mechanical methods such as coatings and contact probes. Lastly, the Shack-Hartmann technique will be presented.

Rear and front surface coatings

One method for frustrating rear surface reflection is the application of an appropriate index matching coating. One may also apply a highly reflective coating to the front surface, thereby eliminating the back reflection. Unfortunately, this impairs routine inspection of optic foils by adding complex application and cleaning procedures. In our case, coatings induce warp on the thin optics or change their elastic behavior as well as requiring subsequent cleaning [10].

Partially coherent or white-light illumination for phase shifting interferometry

White light has a much shorter coherence length than a monochromatic laser owing to the range of wavelengths that comprise it. This has been exploited in modern interferometry to eliminate ghost fringes from the back reflection of a transparent material, among other applications [41]. This technique is limited to samples whose

warp is less than their thickness.

A Michelson interferometer has been commonly used for white-light interferometry. In this setup, unwanted interference fringe patterns from parallel surfaces of transmissive plates are eliminated by limiting the production of interference fringe patterns to reference and test surfaces located at equal optical path lengths along reference and test arms. More precisely, the lengths of both arms are carefully adjusted such that the optical path difference (OPD) is within the source's coherence length [29, 30, 31]. Well-matched optics are required between the reference and test arms, which can be prohibitively expensive for measuring large test plates. ADE Phase Shift has developed an equal path interferometer for this purpose [27]. This instrument features a 2-3 μm coherence length. The front or rear face of photomasks and flat panel displays, which are thicker than this, can be successfully measured since interference fringes will only be formed from one surface.

A white-light Fizeau interferometer reported by Schwider [28] achieved similar results. Schwider combined a Fabry-Perot interferometer in front of a two-beam Fizeau interferometer to get white-light fringes. One disadvantage to this setup is the poor light efficiency caused by the low reflectance of the Fizeau plates and the low transparency of the Fabry-Perot interferometer averaged over the full-width-half-max (FWHM) of an interference filter.

Wavelength-tuned phase shifting interferometry

de Groot *et al.* [34, 35] has developed a Fizeau interferometer operating with software that mathematically separates the interference contributions of plane-parallel surfaces. This solution is based on processing the interference data generated with two single-mode wavelengths. The cumulative interference produced by three surfaces R , T , and S (reference, test, and rear) is measured with a first wavelength λ_1 and then with a second wavelength λ_2 , in sequence. The sample is then flipped over with the rear surface S now facing the reference surface R , and the cumulative interference is again measured with the two wavelengths, λ_1 and λ_2 . Thus, four sets of data are generated from which the desired interference between the reference and the

test beams may be extracted by mathematical manipulation. The measurement of either or both parallel surfaces of a test plate therefore requires a sequence of phase-shift measurements and inversion of the test plate for measuring both surfaces in two opposite orientations. This method requires double handling of the sample, which should be avoided on our low stiffness foils.

A Twyman-Green interferometer has been developed by Okada *et al.* [32, 33] that can obtain separate measurements of surface shapes and refractive index inhomogeneity of optical elements using tunable-source phase shifting interferometry. Separation of the interferogram from the front and rear surface becomes possible since the wavelength change is proportional to the OPD of the two arms (reference and test). This means that interferograms with different optical path differences have a different amount of phase shift. This device acquires sixty interference images at a sequence of wavelengths and least-square fits the first-order terms to calculate surface and optical thickness profiles.

A variation on this technique has been implemented by Deck [42] in which a Fourier analysis of the interference spectrum extracts the frequencies and phases of all of the surfaces in a transparent flat. Zygo Corporation has successfully implemented this wavelength-tuned Fourier transform PSI in a commercial product which can measure both the front and back surface profiles, optical thickness variation, and index homogeneity.

Spatial separation of reflections

A grazing incidence interferometer by Dewa *et al.* [37] exploits the reflective surface properties of plane-parallel plates to individually measure surface topologies of either or both parallel surfaces of such test parts in a single mounting position. Illumination at grazing incidence laterally shears reflections of a test beam from the two surfaces, and spatial coherence of an extended light source is limited in relation to the lateral shear to prevent the formation of an undesired interference fringe pattern between the two parallel surfaces of the plate. In addition, this device provides for realigning a reference beam with the portion of the test beam that is reflected from one of the

parallel surfaces but not the portion that is reflected from the other surface. The realignment favors the formation of an interference fringe pattern between the reference surface and the one parallel test surface to the exclusion of a similar interference pattern between the same reference surface and the other parallel test surface. This technique can be utilized to make the sheet appear thicker (i.e. longer than the illumination coherence length) for conventional PSI or the reflections can be spatially separated for the front and back reflection using a relatively small, scanning source.

Evans *et al.* [36] has also pursued a method of spatial separation of the two reflections. In this work, a Ritchey-Common configuration allows testing of flats with a spherical wavefront. With the flat at an angle to the expanding spherical wave propagation direction, a spatial shift in the two surface reflections occurs. This shift is a function of the thickness of the plate and the tilt angle. Additionally, rays reflected from the rear surface will be refracted as they traverse the front surface, producing an aberrated wavefront with focus displaced from the ideal position. Simulation and experimentation has demonstrated that this back reflection can be effectively spatially blocked with a stop.

Our application would certainly extend these techniques to their limit. Precise optical alignment will be paramount. The grazing incidence technique will also require precision machine design for a translating source and sensor. Linear and angular errors will directly affect the measurement accuracy.

Grating interferometry

An adjustable coherence depth interferometer has been studied by de Groot *et al.* [38, 39] This geometrically desensitized interferometer (GDI) uses two beams at different incident angles to generate an interference pattern with an equivalent wavelength of 5-20 μm . Recognizing that the coherence depth is a function of the size and shape of the light source, the GDI can separate the front and back reflections of transparent flats if the coherence depth is less than the sample thickness. In this work, the minimum coherence length obtained is 152 μm . This is just less than half of the 400 μm sample thickness for our work, so this technique may be feasible, although back fringes will

be observable, yet attenuated. From the data reported [39], the back reflection for our samples would be about 13 times weaker than the front.

Multimode laser diode

A Fizeau interferometer that utilizes a multimode (i.e., multilongitudinal-mode) laser as a light source for testing transparent thin-plate samples has been developed by Ai [40]. As a result of the multimode laser operation, interference fringes are obtained only when the optical separation between the reference surface and test surface is an integer multiple of the laser's effective cavity length. By judiciously selecting the multimode spectrum of operation and the effective cavity length of the laser, the interferometer may be calibrated to produce interference fringes at a workable optical separation between the reference and test surfaces without ghost fringes from the opposite surface of the thin-plate sample.

For this technology to work in our application, there would need to be a sufficiently large number of modes under the gain curve in the power spectrum so that the spikes in the coherence function would be very narrow. According to Ai [40], the spike width, ~ 0.15 mm, was shorter than the glass thickness of 1 mm, so there was no interference pattern between the sample's two surfaces.

Contact metrology

A contact metrology method was also considered. In this scheme, a touch probe which uses a high frequency resonating stylus to detect contact with a test object would be used as a displacement transducer in an application similar to what is found in many contact coordinate measurement machines (CMM's). The probe requires 0.1 mN of force to detect contact. Application of this force to the center of a simply supported sheet without considering gravity would result in a deflection of

$$\delta_{max} = \frac{PL^3}{48EI} \tag{3.1}$$

where P is the load in Newtons, L is the optic length, E is the Young's modulus of borosilicate glass, and I is the moment of inertia. I is further defined as

$$I = \frac{wh^3}{12} \quad (3.2)$$

where w is the optic width and h is its thickness. Substituting values, we find that

$$I = \frac{(100 \times 10^{-3} \text{ m})(400 \times 10^{-6} \text{ m})^3}{12} = 5.3 \times 10^{-13} \text{ m}^4. \quad (3.3)$$

Substituting into equation 3.1 yields

$$\delta_{max} = \frac{(1 \times 10^{-4} \text{ N})(140 \times 10^{-3} \text{ m})^3}{48(6.3 \times 10^{10} \text{ N/m}^2)(5.3 \times 10^{-13} \text{ m}^4)} = 170 \text{ nm}. \quad (3.4)$$

The small distortion is below the flatness tolerance. However, this system would require a vertical, high precision stage to map the foil topography. Also, throughput would be restricted by the serial scanning procedure.

Shack-Hartmann

The Shack-Hartmann technology was developed by Shack and Platt [43] as an improvement to the existing Hartmann concept. Shack-Hartmann sensors do not rely on light-interference effects but rather infer local near-field wavefront gradients by measuring a corresponding focused spot position in the far field. To do this, an array of lenslets is placed at the system image plane. This array dissects the incoming wavefront, as shown in Figure 3-1. Each lenslet focuses its portion of the wavefront onto the CCD detector array. The average wavefront tilt across each lenslet aperture results in a shift of the respective focal spot. A planar wavefront produces a regular array of focal spots, while an aberrated wavefront produces a distorted spot pattern. Comparing these two produces a map of the wavefront slopes, and integration of these slopes allows reconstruction of the test wavefront [26, 43]. The wavefront incident on the lenslet array can be the test wavefront directly (i.e. 1:1 magnification) or it can be demagnified, as long as this is accounted for in the wavefront reconstruction software.

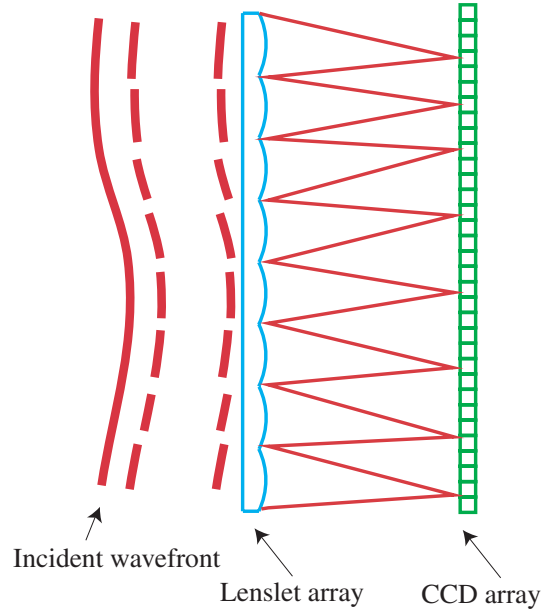


Figure 3-1: Shack-Hartmann wavefront sensing concept.

3.1.2 Justification for Shack-Hartmann technology selection

The Shack-Hartmann technology offers a number of advantages over phase-shifting interferometry for our relatively large-optics metrology application [44]. In the Shack-Hartmann system, temporally incoherent light sources can be used, which are generally cheaper than lasers. The sensors can produce short-duration frames either by shuttering the detector or by using a pulsed light source, thus mitigating the effects of vibrations and turbulence by allowing many effectively instantaneous measurements to be averaged. Shack-Hartmann sensors can function in poorly controlled environments, such as a clean room with air turbulence and acoustic noise, that would introduce errors in phase-shifting interferometry measurements or preclude them entirely [45, 46, 47]. The sensors themselves are much less complex and expensive than sequential PSI's, and can provide greater dynamic range.

There are, of course, some drawbacks to this selection. The advantages are balanced by a reliance on the fidelity of the wavefront reconstruction algorithm and by low spatial resolution and sensitivity as compared to PSI. According to a study by Koch *et al.* [44], Shack-Hartmann sensors can measure difference wavefronts with a fidelity approaching that of a PSI provided an appropriate number of individual

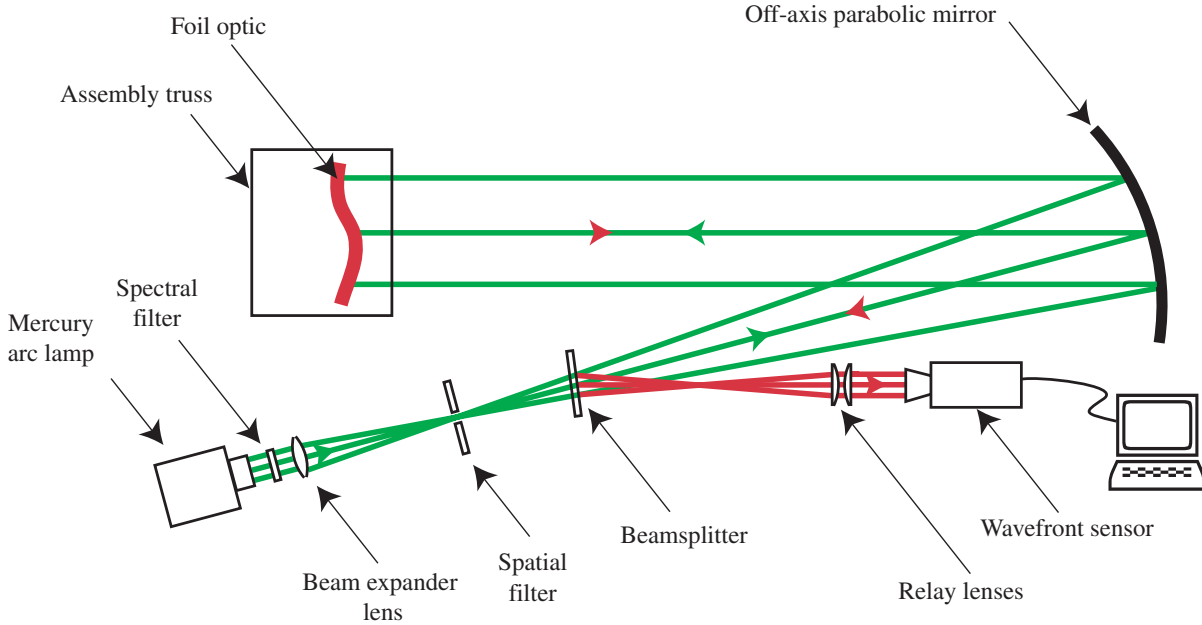


Figure 3-2: Shack-Hartmann surface metrology system.

measurements are averaged and with a spatial resolution that is adequate for the application. This is especially true in our large optic application, where longer scale-length aberrations (e.g. due to mounting distortions) are important to characterize at full aperture even with reduced angular sensitivity, but where high spatial frequency distortions can be measured more easily over small subapertures.

3.2 System design overview

The optical design for the deep-UV Shack Hartmann metrology tool is shown in Figure 3-2. Collimated illumination is spectrally filtered and then focused by a beam expander lens. This light is then spatially filtered to propagate as an expanding spherical wave. The spherical wave is collimated by an off-axis paraboloid, which limits the maximum size of the object under test. The collimated light then reflects from the test optic, the paraboloid again, and the beam splitter. The optical information is then re-collimated by the relay lenses, dissected by a lenslet array inside the sensor, and falls onto a charged coupled device (CCD) detector. From there, software

3.3 Detailed design

3.3.1 Arc lamp

To provide the illumination for this optical metrology system, a 200 W broadband mercury arc lamp was selected. The photon emission is concentrated at the cathode and anode of the lamp, so-called “hot-spots.” A hot-spot can then be imaged onto a pinhole.

In operation, the nearly omnidirectional output of the lamp is amplified by a spherical rear reflector. The light then expands from the center of the lamp to fill a collimating lens in the condenser (housing exit tube). After passing through the spectral filter, a positive power lens with an $f/\#$ matched to the off-axis parabola focuses the light. At the focus of this lens, a magnified image of the lamp is formed. The magnification is given by the ratio of the $f/\#$'s of the lenses as

$$\text{arc magnification} = \frac{f/\#_2}{f/\#_1} = \frac{3.8}{1.5} \quad (3.6)$$

where $f/\#_1$ is for the collimating lens and $f/\#_2$ is for beam expander lens. The original arc size of $0.6 \times 2.2 \text{ mm}^2$ is therefore imaged to $1.5 \times 5.7 \text{ mm}^2$. High spherical aberration will roughly double this image size, resulting in a $3 \times 10 \text{ mm}^2$ arc image. This image is then spatially filtered as shown in Figure 3-2.

Arc instability

A major drawback to the arc lamp as a source is arc instability. Although the illumination from the electrodes shows good rotational symmetry [48], there are spatial variations which can be detected by the wavefront sensor. These changes in local tilt and intensity are caused by convection currents inside the lamp, arc migration on the electrodes, and ambient temperature changes. Assuming these fluctuations are random with a Gaussian probability distribution, the effects on the metrology measurements have been mitigated by averaging 100 successive images over a several minute time span.

A light intensity controller (Oriel, model 68950) was considered to help solve this problem. An analysis showed that this device would have an unacceptably slow sampling rate of 240 ms. The unit is mainly designed to counteract much slower output changes such as caused by age, filament or electrode erosion, and gas absorption or desorption. Also, the light sensor would require valuable power downstream to close the feedback loop. High cost, up to 50% of the cost of the arc lamp itself, was also a factor in the rejection of this unit. Lastly, since the averaging technique proved reliable, the need for another solution was reduced.

Heat rejection

The heat rejection fan for the arc lamp housing blows hot air towards the test optic. To eliminate potential thermal distortion, a hose and blower (Oriel, model 61720) were installed. This replaced the lamp housing heat rejection fan and cools the lamp by removing heat from the vicinity.

Rejecting infrared radiation (IR) in the usable output was critical. This heat could crack the spectral filter, distort its shape, or change its transmission characteristics. For this purpose, a beam turning assembly with a dichroic mirror was considered. After study, it was concluded that this would not be necessary since the filter could reflect most of the incident IR. Also, slight and low temporal frequency changes to the filter transmission curve would not jeopardize the accuracy of the metrology data.

3.3.2 Spectral filter

The optical properties of borosilicate glass (Schott Glas, model D-263) are shown in Figure 3-4. From the transmission curve, light incident on the glass foil at wavelengths greater than 300 nm will partially transmit through the substrate and reflect off its back surface. This will result in a doubled set of input data to the wavefront sensor (See Figure 3-5), corrupting wavefront reconstruction. For example, if a higher wavelength HeNe laser were used for illumination, the ratio of the power from the front to back reflection would be 1.3. This would make the wavefront reconstruction

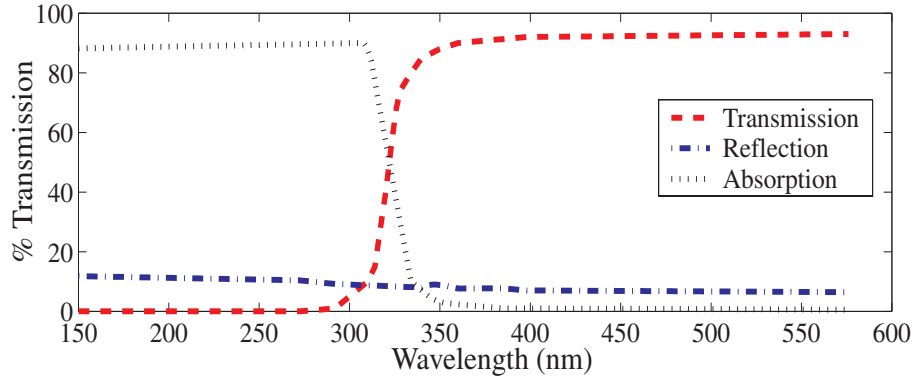


Figure 3-4: Optical properties of 0.4 mm thick borosilicate glass (Schott Glas, model D-263).

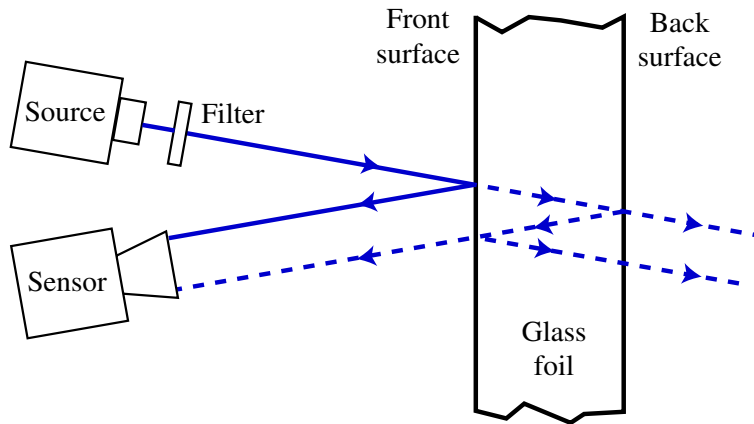


Figure 3-5: Path of light reflected from front and back surfaces of glass into sensor. Back reflections (*dashed line*) should be avoided.

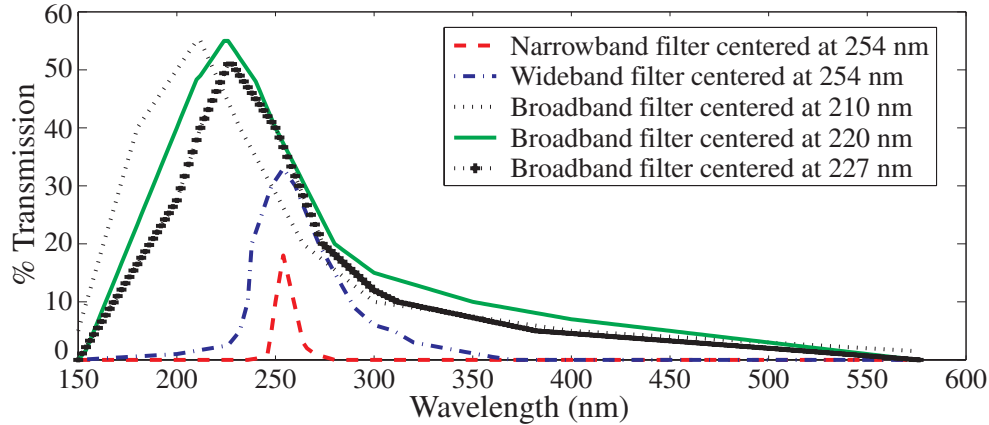


Figure 3-6: Transmission curves for a range of spectral filters (Acton Research, Omega Optical)

erroneous. Therefore, we ideally seek a filter that passes 100% of the electromagnetic radiation below 260 nm and blocks 100% above. Of course, real filters simply attenuate all wavelengths to varying extents. We therefore need to balance the attenuation of the visible wavelengths and the total power input to the system. Filters considered are shown in Figure 3-6 [49, 50]. As a baseline for the power measurements, the most conservative filter was installed in the system. Although this filter successfully blocked nearly all of the long wavelength light, only $1.1 \mu\text{W}$ of power was incident on the sensor. This resulted in a very low signal-to-noise ratio (SNR), with high gain. From this test, it was estimated that a signal strength increase of five times would be desirable.

To choose the best spectral filter, a simulation was created to evaluate (1) the total power incident on the detector and (2) the power incident on the detector from the front and back reflections. This algorithm multiplies the lamp spectral irradiance by the filter transmission curve to calculate the spectra incident on the glass optic under test. Then, accounting for the transmission, reflection, and absorptive properties of the 0.4 mm-thick glass at the incident wavelengths, the spectra returned to the wavefront sensor from the front and back surface is computed. The lumigen-coated CCD responsivity is not constant over the wavelength band [51], so this quantum efficiency is considered in the simulation as well. Integrating the resulting spectra yields the total powers returned from the respective reflections. These values indicate

Spectral filter peak λ (nm)	254	254	210	220	227
Filter shape	narrow	wide	broad	broad	broad
Power into sensor (μW)	1.1	4.1	7.2	9.5	7.8
Focal spot intensity ratio	>1000	40.0	3.9	4.6	5.5

Table 3.1: Comparison of spectral filters for Shack-Hartmann metrology system. The total power from the front reflection returned to the sensor is shown along with the ratio of the power from the front and back reflection, named the focal spot intensity ratio.

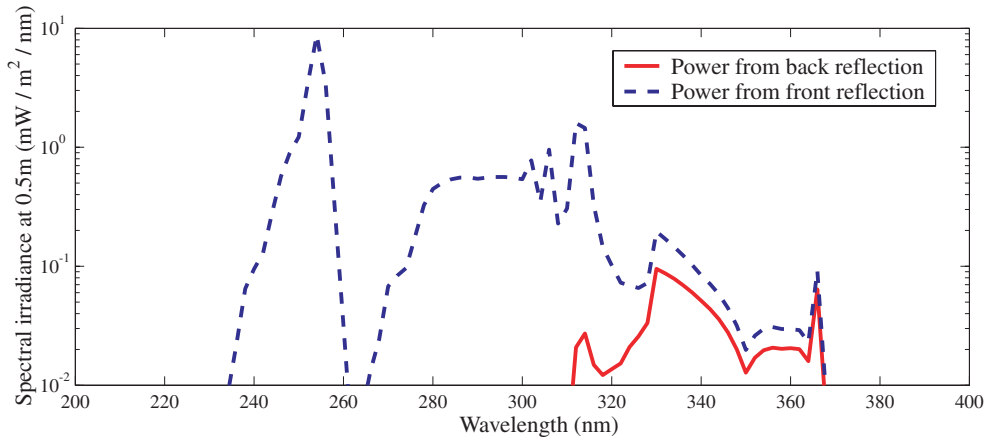


Figure 3-7: Irradiance reflected from glass sheets into wavefront sensor as a function of wavelength for the 254 nm wideband filter. This simulation considers the arc lamp spectral output, spectral filter transmission, optical properties of the borosilicate glass, and lumogen coating on the CCD.

the relative intensity of the front and back focal spots on the detector. From this data, Table 3.1 was generated. A plot of the front and back reflected power into the sensor for the 254 nm wideband filter is shown in Figure 3-7. As shown in Table 3.1 for this filter, the ratio of the area under the front reflected curve to the area under the back reflected curve is 40.0. The back reflection power is below the sensor noise floor, making the error signal negligible. Also, the 4.1 μW total power incident on the CCD for the 254 nm wideband filter was satisfactory. For these reasons, this filter was selected.

3.3.3 Spatial filter

The spatial filter has two functions. It cleans up the illumination from the arc lamp, reshaping the profile to an expanding spherical wave. The spatial filter also plays a key role in determining a lenslet's focal spot size on the detector. If the former were the sole factor, one would select the smallest pinhole that admitted power above a SNR threshold. However, the latter role of the spatial filter constrains the lower bound on the diameter.

Making the pinhole too large would do more harm than affecting the spherical wave profile. A large pinhole would effectively consume the dynamic range of the sensor, since a lenslet's focal spot would then cover all of the pixels dedicated to it. An upper bound on the pinhole size is thus imposed such that the size of the focal spot on the detector should not exceed half of that lenslet's pixels. For the sensor selected, there are 16 pixels/lenslet.

To determine the size range for the pinhole, a few calculations need to be performed. A focal spot on the detector should cover at least 10 pixels for accurate centroiding, so the diameter of the spot should therefore be at least 3.6 pixels. Diffraction effects from the lenslet array will increase the focal spot size. A collimated input to a lenslet will have a focal spot diameter due to diffraction given by

$$d_{\text{focal spot, diffraction only}} = \frac{2\lambda f_{\text{lenslet}}}{d_{\text{lenslet}}}. \quad (3.7)$$

Using the peak transmitted wavelength, λ , of 253.7 nm, the lenslet parameters diameter, d_{lenslet} , of 224 μm , the focal length at λ , f_{lenslet} , of 17.904 mm, the focal spot diameter due to diffraction is 40.6 μm .

Next we need to consider the demagnified pinhole contribution. This demagnification is given by the ratio of the focal lengths of the lenslet array and the relay optic. The other lenses do not contribute to the demagnification since a conjugate 1:1 magnification of the pinhole occurs between the beam splitter and the relay lenses as shown Figure 3-2. Therefore, the diameter of the pinhole image on the detector is

given by

$$d_{\text{pinhole image}} = \frac{f_{\text{lenslet}}}{f_{\text{relay optic}}} d_{\text{pinhole}}. \quad (3.8)$$

With f_{lenslet} given above and $f_{\text{relay optic}} = 75.0$ mm, the pinhole diameter on the CCD is equal to $0.239 d_{\text{lenslet}}$. Hereafter, m will denote the pinhole magnification of 0.239.

These two effects, diffraction and pinhole demagnification, are combined by convolution. This is approximately the same as addition in this case, yielding a total focal spot size on the detector of $40.6 \mu\text{m} + 0.239d_{\text{pinhole}}$. This focal spot diameter must cover at least 3.6 pixels for sensitivity, as previously mentioned, but not more than $(\frac{1}{2})16 = 8$ pixels for dynamic range. Since the pixel size is $14 \mu\text{m}$, we have

$$3.6 \text{ pixels} < \frac{40.6 \mu\text{m} + (0.239)(d_{\text{pinhole}})}{14 \mu\text{m}/\text{pixel}} < 8 \text{ pixels}. \quad (3.9)$$

To satisfy this inequality, the pinhole diameter must be between 41 and 299 μm in size. To admit as much power as possible, a 250 μm diameter pinhole was selected.

3.3.4 Beam splitter

A beam splitter was selected based on a satisfactory combination of substrate material, coatings, and diameter. For the substrate, UV-grade fused silica was the easy choice since it can transmit better than 90% down to 160 nm. To avoid the influence of dust or local defects, a 2 inch diameter was chosen with the intention of filling the clear aperture.

A multilayer dielectric coating was selected for our application. The slight polarization effect is not detrimental. This beam splitter has an average polarization transmittance/reflectance of 50% at 45° incidence. This percentage was selected based on the following maximization calculation. A beam splitter diagram showing the transmitted beam T , reflected beam R , and the transmitted/reflected beam to the sensor is shown in Figure 3-8. For this description, T and R are percentages of transmission and reflection, respectively; they sum to one, neglecting absorption. The choice of transmittance/reflectance coating is based on the maximization of $T \cdot R$.

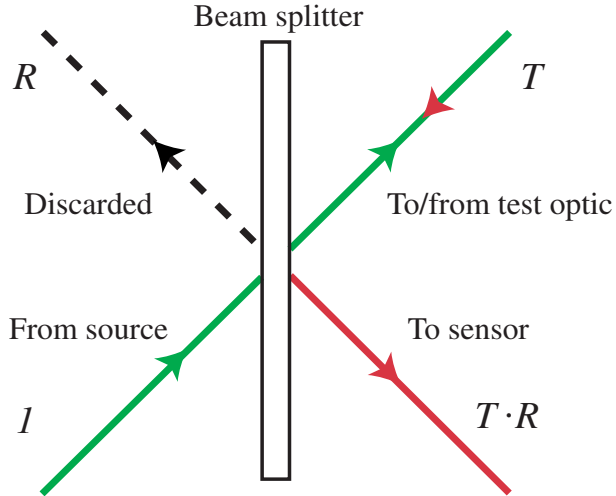


Figure 3-8: Beam splitter diagram showing transmitted beam T , reflected beam R , and the transmitted/reflected $T \cdot R$ beam to the sensor.

Given

$$T = 1 - R, \quad (3.10)$$

then

$$TR(R) = R(1 - R). \quad (3.11)$$

Taking the derivative and setting it equal to zero to maximize yields

$$\frac{d(TR(R))}{dR} = 1 - 2R = 0. \quad (3.12)$$

Therefore,

$$R = 50\%. \quad (3.13)$$

The anti-reflection coating on the back side is a limiting factor. This somewhat narrowband coating reflects around 0.5% or less at 248 nm. From there however, as the wavelength is increased, there is a gradual rise to the uncoated reflectivity (around 4%) at 400 nm. Beyond 400 nm, the reflectivity is flat all through the visible (700 nm). This presents a slight problem, since the aforementioned spectral filter does leak some light at 400 nm. A reflection from the back of the beam splitter has been observed in the laboratory. Luckily, the thickness of the beam splitter allows

this unwanted light to be spatially blocked.

3.3.5 Laser source discussion

At this point, the reader may wonder why a laser was not selected as the source. Indeed, a 266 nm pulsed solid-state laser could serve as a deep-UV source. No spectral filter would be required, the Gaussian profile would be constant, and power would be more than sufficient. The JDS Uniphase nanolaser (model NU-00111-100) was investigated for this purpose, and several drawbacks were realized. The first concerned the beam waist at the pinhole. Converging the beam down with such a fast lens would result in only a 2.1 μm waist since

$$\text{waist} = \frac{\lambda}{\sin \theta} \approx \frac{\lambda}{\theta} = 2 \lambda (f/\#) = (2)(266 \times 10^{-9} \text{ m})(3.88) = 2.1 \mu\text{m}. \quad (3.14)$$

This small waist could be a problem since there is a high average power per pulse. The laser performance specifications include 2 mW output power, 10 kHz repetition rate, and 1 nsec pulse width. Therefore,

$$\begin{aligned} \text{avg power during 1 nsec pulse} &= \text{output power} \div \text{repetition rate} \div \text{pulse width} \quad (3.15) \\ &= 2 \times 10^{-3} \frac{\text{J}}{\text{sec}} \div 10 \times 10^3 \frac{\text{pulse}}{\text{sec}} \div 1 \times 10^{-9} \frac{\text{nsec}}{\text{pulse}} \\ &= 200 \text{ W}. \end{aligned}$$

Squeezing 200 W of power into such a small volume could potentially cause a breakdown in the air. This spark would then act as the temporarily unsteady source for the system. Additionally, this spark could damage the perimeter of a pinhole, increasing its diameter with time. One solution to this problem would be to reduce power with a neutral density filter. Another solution would be to simply expand the beam from the laser head, thus removing the focus and spatial filter. The beam would have to be diverged again after the beam splitter.

Another potential problem exists for the laser source. To accurately centroid a focal spot on the detector, it should cover at least 10 pixels in area. This argument

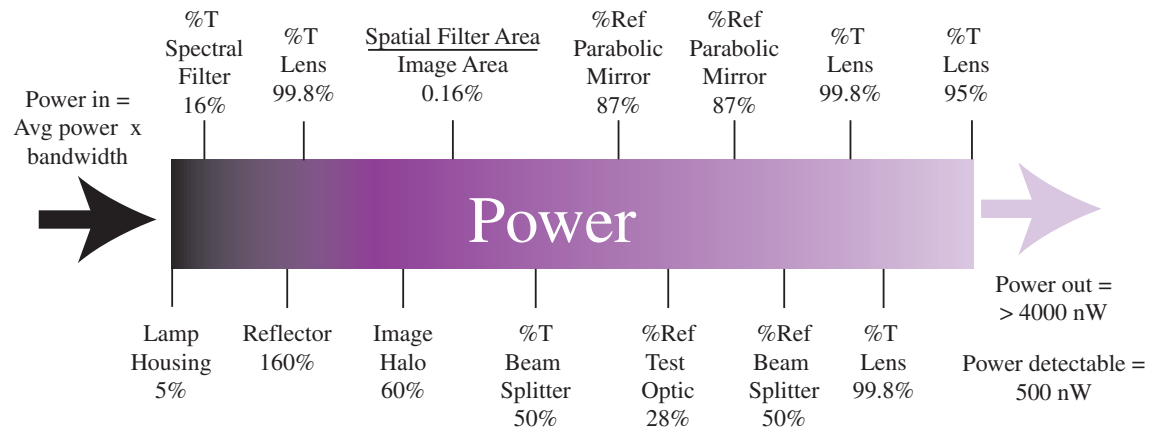


Figure 3-9: Power losses throughout the optical path of the Shack-Hartmann surface metrology system.

was the basis for the actual pinhole size selected. Since the focused spot (waist) from the laser is so small in diameter, it would effectively serve as its own $2 \mu\text{m}$ pinhole. This area would be largely increased by diffraction by the lenslet array, to around $46.5 \mu\text{m}$ in diameter. However, with a $14 \mu\text{m}$ pixel size, the spot would only cover 7 pixels in area. This could compromise centroiding accuracy which is critical to the angular resolution. This problem could be mitigated by moving the detector within the camera to an out of focus position or physically moving the parabola or relay lenses, thus blurring the focus.

Lastly, the cost for the laser source is approximately 30% greater than the arc lamp (including the heat rejecting blower). Considering all of these complicating factors, the arc lamp source was selected.

3.3.6 Power considerations

Making sure that enough irradiance would reflect from the inefficient glass and return to the sensor for a successful measurement was a prime consideration in the design. Irradiance from the source is lost at many locations along the optical path, as illustrated in Figure 3-9. To keep track of the power remaining for imaging, we need to calculate the power into the system and the power lost. This process starts with the arc lamp inside of the lamp housing. To find the total power coming out of this lamp,

the spectral filter bandwidth (FWHM) is multiplied by the average power from the lamp spectral irradiance curve over this bandwidth. From Figure 3-6, the FWHM is 40 nm. The average flux from the lamp over this bandwidth is 35 mW/m²-nm [48]. So the flux from the lamp is 1400 mW/m².

Three multiplicative factors next affect this power: the spectral filter transmittance, lamp housing rear reflector, and the housing itself. The filter transmittance at FWHM is approximately 20%, again pulled from Figure 3-6. The lamp housing rear reflector acts as an amplifier, yielding a 160% boost [48]. The housing itself is naturally very lossy, since the omnidirectional irradiance is mostly wasted, excluding the contribution from the rear reflector. The housing factor is a mere 5% [48]. So in the exit tube of the lamp housing, we have $1400 \text{ mW/m}^2 \times 0.2 \times 1.6 \times 0.05 = 22.4 \text{ mW/m}^2$.

The anti-reflection-coated fused-silica beam-expander lens at the end of the condenser (exit tube) transmits 99.8% of incident light. So the image of the arc formed at the spatial filter contains $22.4 \text{ mW} \times 0.998 = 22.34 \text{ mW/m}^2$. As mentioned in Subsection 3.3.1, this image size is 30 mm². About 40% of this power is lost in a “halo” around the image, further reducing our available power to 13.4 mW. Next we spatially filter with a 250 μm pinhole, as described in Subsection 3.3.3. The ratio of the area of this pinhole to the area of the image is 0.16%, so a mere 21 μW makes it through.

This light then goes through a veritable pinball machine of mirrors and lenses until it is incident on the CCD detector inside of the wavefront sensor. The percentage transmitted or reflected by each component in normal operation is summarized in Table 3.2. This data was compiled from intensity graphs as cited. Intensity data can be used since power is proportional to intensity. So the final power incident on the CCD detector is 21 μW from the spatial filter multiplied by 15.6% for the optical elements downstream. This calculation gives roughly 3.3 μW of power centered at 254 nm to excite electrons in the CCD. This light is then divided unevenly by the lenslets over the 1024 \times 1024 pixel CCD. Is this enough? Tests of the measurable power threshold for this instrument indicate that 500 nW is detectable, but 1 μW is

Optical element	T,R	%	Source
Beam splitter	T	50	[52]
Parabola	R	87	[53]
Test optic (Si or glass)	R	50	[54, 9]
Parabola	R	87	[53]
Beam splitter	R	50	[52]
Relay optic 1	T	99.8	[55]
Relay optic 2	T	99.8	[55]
Lenslet array	T	95	[56]
TOTAL		15.6	

Table 3.2: Optical element transmission (T) and reflection (R) percentages from spatial filter to CCD detector. The items are listed in the order that the light “sees” them. Repeated items are “seen” twice. High transmission percentages are due to anti-reflection coatings.

needed for a lower gain, higher SNR measurement. An incident power of $4.1 \mu\text{W}$, as shown in Table 3.1, is therefore satisfactory.

3.3.7 Wavefront sensor

There were a number of tradeoffs considered in the selection of this device as identified by Greivenkamp *et al.* [26]. The spot displacement on the detector is equal to the wavefront slope times the focal length of the lenslet. A limitation to the allowable wavefront slope, or dynamic range, is imposed by the detector area allocated to that lenslet.[†] For the same detector, a lenslet array with a shorter focal length will have greater dynamic range with reduced sensitivity. On the other hand, a longer focal length lenslet will allow greater accuracy in determining the average incident wavefront slope since a given slope produces a greater spot displacement. So there is a tradeoff of sensitivity and dynamic range associated with the lenslet focal length.

The size versus number of lenslets is another important tradeoff. As the number of lenslets is increased for a given area, spatial sampling and spatial resolution are increased. This results in less averaging of the wavefront slope over the lenslet aper-

[†]This is primarily a software-based limitation. There is no inherent requirement that a spot remain within the cell of pixels associated with its lenslet. Spots can translate several cells as long as the one-to-one correspondence between the spots and the lenslets can be mapped or identified [26].

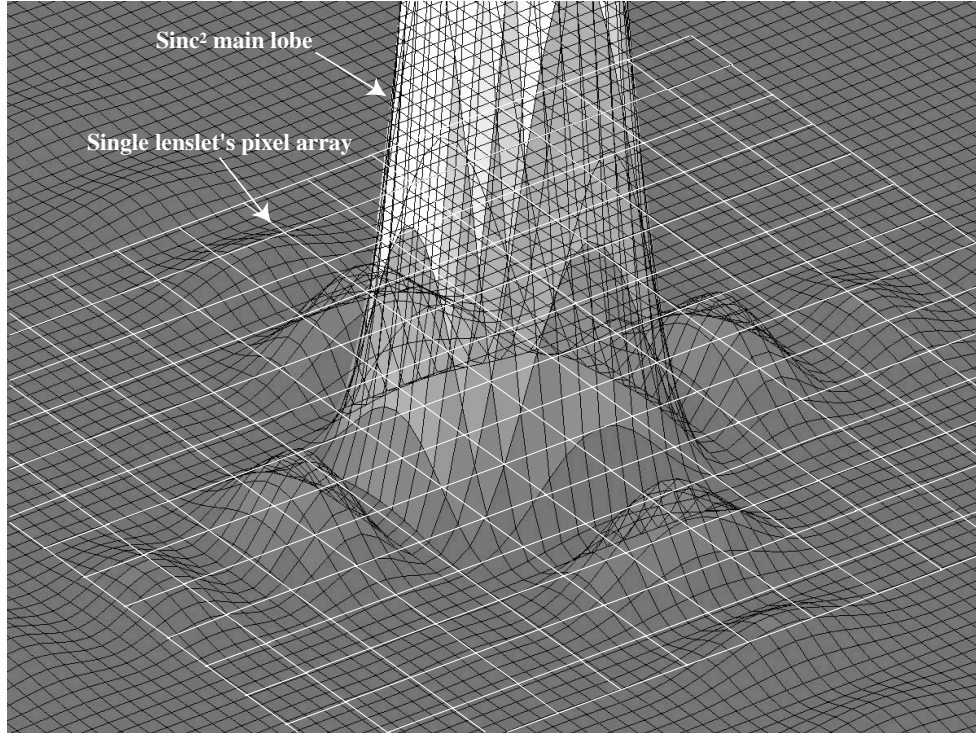


Figure 3-10: The sinc^2 focal spot is shown overlaid with the pixels apportioned to a lenslet inside the Shack-Hartmann wavefront sensor.

ture, but reduces the number of detector pixels that are available behind each lenslet to make the measurement. Selecting larger lenslets will allow a more sensitive measurement of slowly varying wavefronts, but may not sufficiently sample high spatial frequency wavefronts, producing artificially smooth surface maps.

Pixel size on the detector and the lenslet $f/\#$ are also related. The spot size produced by each lenslet must be sufficiently large (covering at least 10 pixels in area) to obtain a good centroid calculation, while separation between spots from adjacent lenslets must be maintained to ensure dynamic range. As a general rule, the spot size diameter should not cover more than half of the number of pixels dedicated to a lenslet's diameter for a reasonable balance of sensitivity and dynamic range. The spot size scales linearly with the wavelength and lenslet $f/\#$, so the lenslet diameter and focal length should be selected wisely. Figure 3-10 shows a desirable balance between the sensitivity and dynamic range for a square lenslet array. This focal spot covers 4 pixels in width and length, respectively; there are 16 pixels apportioned for

the lenslets width and length respectively. So the focal spot covers $4 \times 4 = 16$ pixels while not consuming more than $4 \div 16 = 25\%$ of the pixels along that lenslets width or length.

Quantum efficiency study

A quantum efficiency study was performed on another model wavefront sensor (Wavefront Sciences, model CLAS-2D 6612 [57]) to determine if it could meet our needs. Specifically, silicon CCD detector quantum efficiency plummets in the UV, and the manufacturer of this detector could not provide efficiency data for deep-UV wavelengths. Since a limited amount of power was available at 254 nm, there was concern that we could not bombard the CCD with enough photons at this short wavelength to make successful measurements. This sensor did not have the efficiency improving lumigen coating, so we also wanted to know if this coating was necessary for satisfactory deep-UV performance.

In this test, the wavefront sensor relative quantum efficiencies at 633 nm and 254 nm were measured. Their ratio is useful for determining how much light is needed to achieve a given light level at a new wavelength, crudely assuming a linear relationship. The relative quantum efficiency is defined as

$$QE = \left(\frac{S_{\max}(\text{counts})}{I_{\max}(\mu\text{W}/\text{cm}^2)} \right) \left(\frac{1 \text{ sec}}{t(\text{sec})} \right) \quad (3.16)$$

where I_{\max} is the maximum power intensity incident on the lenslet array, S_{\max} is the relative saturation of the detector, and t is the integration time. The 10-bit detector saturates at $2^{10} = 1024$ counts. The power intensity was measured with a separate detector instrument (Newport, model 1830-C). The data from the test are shown in Table 3.3. The quantum efficiencies of this instrument at the two wavelengths are calculated using Equation 3.16 to be

$$QE_{633} = \left(\frac{500 \text{ counts}}{0.687 \mu\text{W}/\text{cm}^2} \right) \left(\frac{1 \text{ sec}}{1/10000 \text{ sec}} \right) = 7.278 \times 10^6 \frac{\text{counts-cm}^2}{\mu\text{W}} \quad (3.17)$$

Test wavelength	nm	633	254
S_{\max}	counts	500	240
I_{\max}	$\mu\text{W}/\text{cm}^2$	0.687	37.5
t	sec	1/10000	1/60

Table 3.3: Wavefront sensor quantum efficiency test data.

$$QE_{254} = \left(\frac{240 \text{ counts}}{37.5 \mu\text{W}/\text{cm}^2} \right) \left(\frac{1 \text{ sec}}{1/60 \text{ sec}} \right) = 384 \frac{\text{counts}\cdot\text{cm}^2}{\mu\text{W}} \quad (3.18)$$

The ratio of QE_{633} to QE_{254} is the information we desire. The resulting efficiency ratio is $\sim 19000:1$. This means that for every 19000 photons that impinge on the detector at 633 nm, only 1 at 254 nm hits it! These results showed that this instrument would not work for our application. After consultation with Wavefront Sciences, we determined that lumigen coating would make a huge difference since the lumigen coating is 30–40% efficient in absorbing the incident light at 250 nm and upconverting to 500 nm.[‡]

Since the efficiency ratio was so large, there was some speculation that this sensor had a plastic lenslet array used for fill factor enhancement on top of the actual silicon CCD detector array. This plastic array would have also absorbed many short wavelength photons. The lenslet array in the final sensor would definitely be manufactured from fused-silica as a result. Additionally, a glass window located immediately in front of the CCD in the final sensor would be removed to avoid this type of problem.

SMD 1M15 Instrument

Wavefront Sciences provided the SMD 1M15 wavefront sensor for our application [57]. The instrument features a 64×64 lithographically etched, fused silica lenslet array. Table 3.4 displays a summary of the notable physical characteristics of the instrument’s lenslet array and detector along with some system magnifications. The CCD detector was coated with lumigen by Spectral Instruments [58] to increase its quantum efficiency.

[‡]The lumigen coating is actually 60-80% efficient in absorbing the incident light at 250 nm and upconverting to 500 nm. However, the lumigen is a thin layer on top of the CCD, so half of the photons are emitted in each direction, thus you lose 50% from the directionality.

System		
Operating wavelength	λ	254 nm
System magnification	M	-0.1
Pinhole magnification	m	0.239
Pinhole diameter	d_p	250 μm
Lenslet		
Lenslet diameter	d_l	0.224 mm
Lenslet focal length at λ	f_l	17.904 mm
Nominal sag		1.378 μm
Active number of lenslets X	N_l	64
Active number of lenslets Y	N_l	64
Total number of lenslets X		72
Total number of lenslets Y		72
Total aperture X	D	16.128 mm
Total aperture Y	D	16.128 mm
Detector		
Pixel size X	p	14 μm
Pixel size Y	p	14 μm
Number of pixels X	N_p	1024
Number of pixels Y	N_p	1024

Table 3.4: Wavefront sensor lenslet array, detector and system magnification summary.

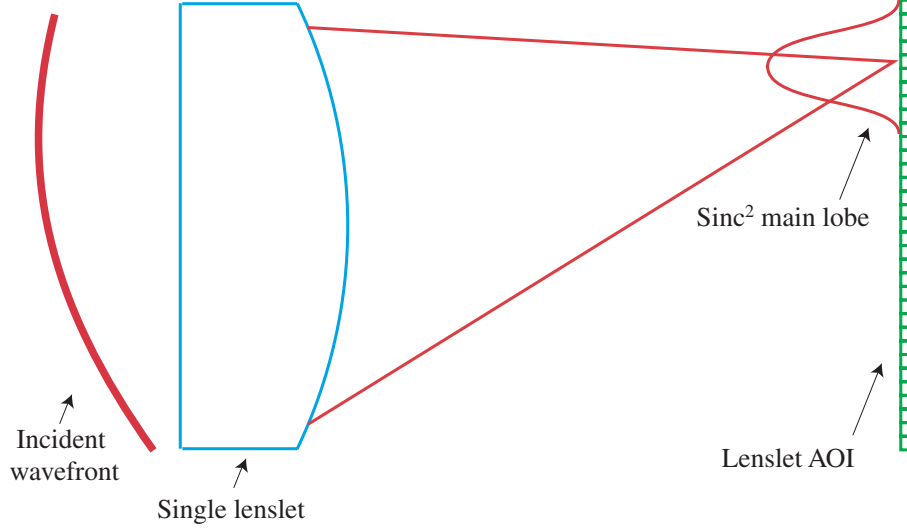


Figure 3-11: The large tilt of the incident wavefront results in a focal spot shift to the edge of the lenslet’s area-of-interest (AOI). This is the extent of the instrument’s angular range.

In selecting this unit, it’s ability to meet our functional requirements for sensitivity and dynamic angular range were paramount. These goals, described in Section 3.1, are $10 \mu\text{rad}$ and 0.3 mrad , respectively.

The dynamic range of measurement is limited by the detector area allocated to each lenslet (named the area-of-interest or AOI). When the focal spot behind a lenslet encroaches on the edge of its AOI, crosstalk occurs and wavefront reconstruction is compromised. This limitation to focal spot shift is depicted in Figure 3-11. Figure 3-10 shows in 3-D a focal spot centered within its AOI. The angular range for this instrument can be geometrically estimated from the lenslet diameter of 0.224 mm and operating focal length of 17.904 mm to be approximately $\pm 6 \text{ mrad}$. Taking the system magnification into account allows one to estimate the measurable dynamic range at the object plane to be $|-0.1 \times 6 \text{ mrad}| = 0.6 \text{ mrad}$. To make a more accurate calculation, we need to consider the focal spot size. The focal spot radius on the CCD at the 254 nm operating wavelength, $r_{\text{spot},254}$, is given by

$$r_{\text{spot},254} = \frac{f_l \lambda}{d_l} + \frac{m d_p}{2} = \frac{(17904 \mu\text{m})(0.254 \mu\text{m})}{224 \mu\text{m}} + (0.239)(125 \mu\text{m}) = 50.2 \mu\text{m} \quad (3.19)$$

where Table 3.4 gives all parameter values. This will effectively reduce the lenslet

diameter. So the actual dynamic range, considering the magnification, will be

$$\text{dyn. range} = M \left(\frac{\left(\frac{d_l}{2} - r_{\text{spot},254}\right)}{f_l} \right) = 0.1 \left(\frac{\left(\frac{224 \mu\text{m}}{2} - 50.2 \mu\text{m}\right)}{17904 \mu\text{m}} \right) = 0.35 \text{ mrad.} \quad (3.20)$$

This instrument will, therefore, meet the dynamic range requirement of 0.3 mrad at the object plane. This angular range is the same for one lenslet or the set of lenslets. For one lenslet with a diameter of 224 μm , which corresponds to 2.24 mm at the object plane, a wavefront tilt of 0.78 μm can be measured. Since $N_l = 64$, the maximum measurable object tilt over the entire lenslet array is 0.78 $\mu\text{m} \times 64 = 50.18 \mu\text{m}$ over a 143.3 mm lateral distance.

Estimating the instrument's sensitivity is a bit more difficult. We need to calculate the noise floor after algorithmic wavefront reconstruction. This analysis requires experimental data for the centroid estimation error as well as knowledge about the digital signal processing used for numerical reconstruction of the wavefront shape. We will start off by calculating the centroid estimation error at the operating wavelength, e_{254} . As a baseline, the manufacturer has tested the centroid estimation error for a similar instrument at 633 nm, yielding $e_{633} = 0.0025$ pixels. To extrapolate our estimate, we need to scale by the square of the diffraction limited spot half widths at this baseline wavelength and the operating wavelength. The square is used to realize an area contribution from a length measurement.

$$e_{254} = e_{633} \left(\frac{\frac{f_l(254 \text{ nm})}{d_l}}{\frac{f_b(633 \text{ nm})}{d_b}} \right)^2 = 0.0025 \text{ pixels} \left(\frac{36.0 \mu\text{m}}{20.3 \mu\text{m}} \right)^2 = 0.0079 \text{ pixels.} \quad (3.21)$$

For the baseline sensor tested at 633 nm, f_b and d_b are its lenslet focal length and diameter, which gives $f_b(633 \text{ nm})/d_b = 36.0 \mu\text{m}$. Now we must use this information to calculate our instrument's RMS angular noise floor. This is a function of the angle to the edge of a pixel and centroid estimation error. Including the magnification will translate us to the object plane. The noise floor is therefore

$$\theta_{\text{RMS}} = M \left(\frac{pe_{254}}{f_l} \right) = 0.1 \left(\frac{(14 \mu\text{m}/\text{pixel})(0.0079 \text{ pixels})}{17904 \mu\text{m}} \right) = 0.61 \mu\text{rad.} \quad (3.22)$$

The minimum measurable variation from flatness, or noise floor, is influenced by the numerical reconstruction algorithm as follows:

$$\text{noise floor} = \sqrt{N_l} d \theta_{\text{RMS}} = (\sqrt{64})(224 \mu\text{m})(0.61 \mu\text{rad}) = 1.1 \text{ nm}. \quad (3.23)$$

The lenslet diameter is included to compute the “per lenslet” noise floor. A factor of the square root of the number of lenslets is introduced to effectively account for the error’s random walk over the lenslet array. Equation 3.23 therefore gives the final numerically reconstructed noise floor, P-V. This minimum measurable deviation from flatness is equal to 1.1 nm. This could occur over a lateral distance as short as 2.24 mm (one lenslet’s diameter magnified). So, this sensitivity corresponds to an angular resolution of $0.5 \mu\text{rad}$ for one lenslet. As greater lateral distances are considered, the angular resolution improves, so the sensitivity functional requirement of $10 \mu\text{rad}$ is always met.

Comparing these calculated values back to the functional requirements, for a 10 mm lateral distance in the object plane, we have theoretically measurable P-V height of $\pm 3.5 \mu\text{m}$ with a resolution of $\pm 1 \text{ nm}$.

3.4 Performance evaluation

3.4.1 Test optic surface mapping

The Shack-Hartmann surface metrology instrument, shown in Figure 3-12, has been successfully used to generate surface maps of large $\frac{\lambda}{30}$ reference flats, $0.45 \text{ mm} \times 100 \text{ mm}$ diameter polished silicon wafers as commonly used in semiconductor industry, and $100 \times 140 \times 0.4 \text{ mm}^3$ glass sheets. The system can provide both angular deviations from flatness and absolute P-V measurements. The former are critical to the telescope resolution, while the latter are of immediate use in polishing and shaping.

Measurement of a 0.4 mm thick borosilicate glass sheet is shown in Figure 3-13. Results from glass metrology show no indication of back reflections in the raw data. The array of focal spots is regular and the frequency of spots is as expected,

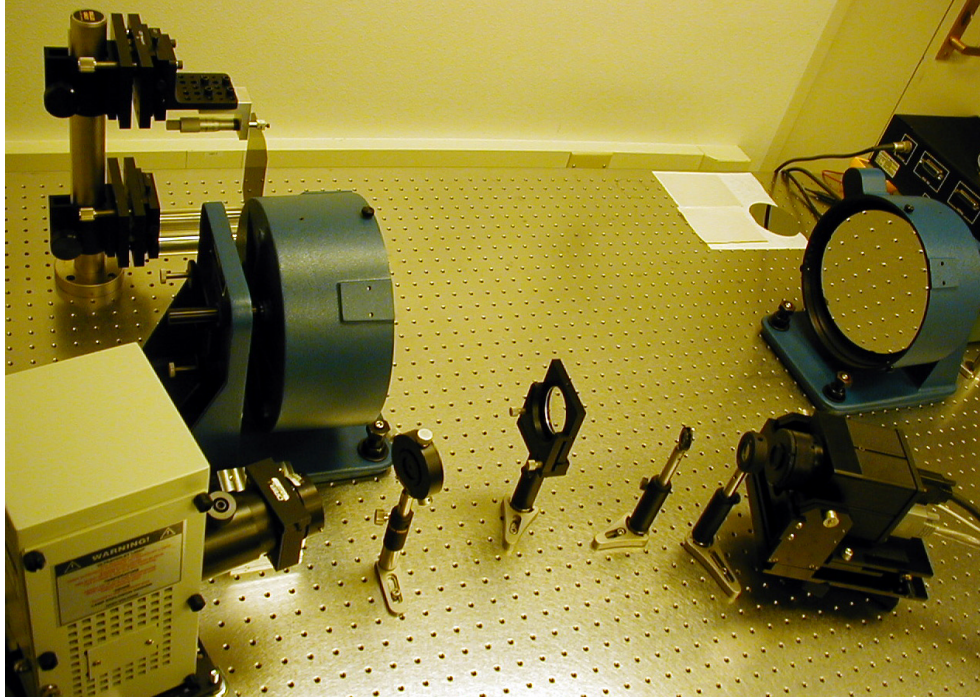


Figure 3-12: Shack-Hartmann metrology system hardware in a class 1000 cleanroom environment at the MIT *Space Nanotechnology Laboratory*.

one per AOI. Large warp in pre-figured stock glass sheets makes their entire surface unmeasurable; however, subset regions have been successfully measured.

The system has also been used to measure the impact of silicon wafer shaping processes on the wafer figure. Preliminary work by Mireille Akilian[§] toward this end is shown in Figure 3-14. Using these “before” and “after” pictures, the distortion due to a shaping process can be characterized. In this instance, the shaping process involves bonding the silicon wafer to a thicker glass substrate using a low thermal expansion thermo-plastic adhesive. Erect and inverted figure captions indicate measurements of the same object with a 180° rotation about the axisymmetric axis. Note the negligible change in the figure before and after bonding. Gravity distortion of the low stiffness unbonded wafer could account for the 190 nm difference between the P-V measurements of the erect and inverted wafer.

[§]MIT Master’s student, Mechanical Engineering Department, *Space Nanotechnology Laboratory*

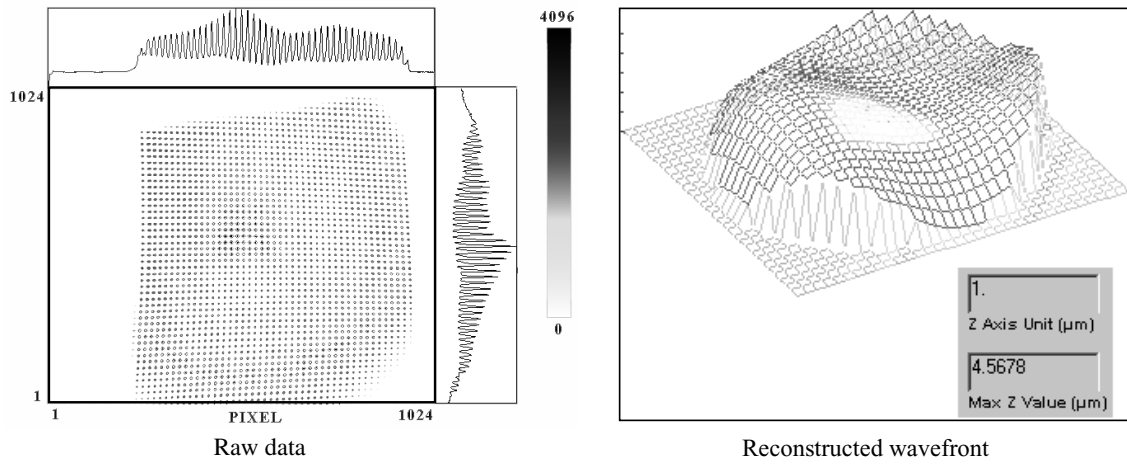


Figure 3-13: Raw data (*left*) is collected on the CCD array in the wavefront sensor. Comparison with a reference image enables the wavefront reconstruction (*right*), which is equivalent to a surface map at the object plane. The intensity scale (*center*) indicates the relative energy density incident on the pixels in $2^{12} = 4096$ discrete values.

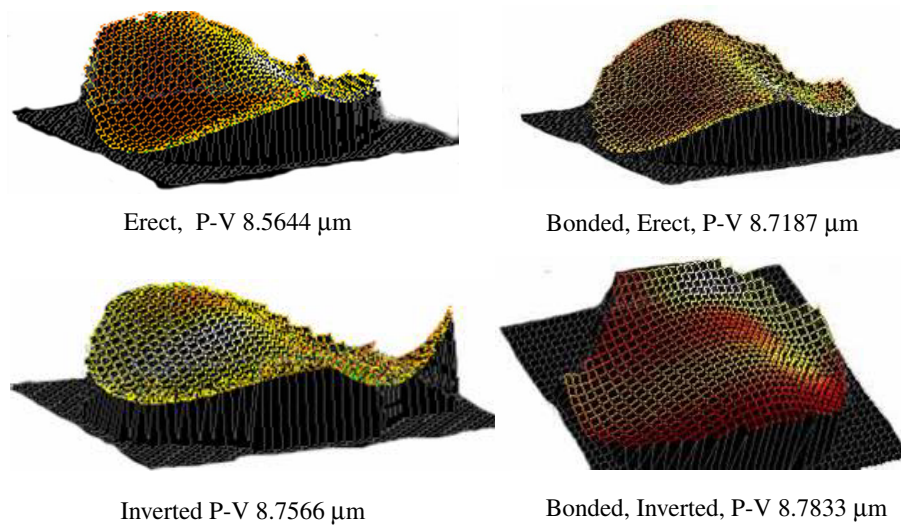


Figure 3-14: Measurement of a single silicon wafer twice before bonding (erect and inverted) and twice after bonding.

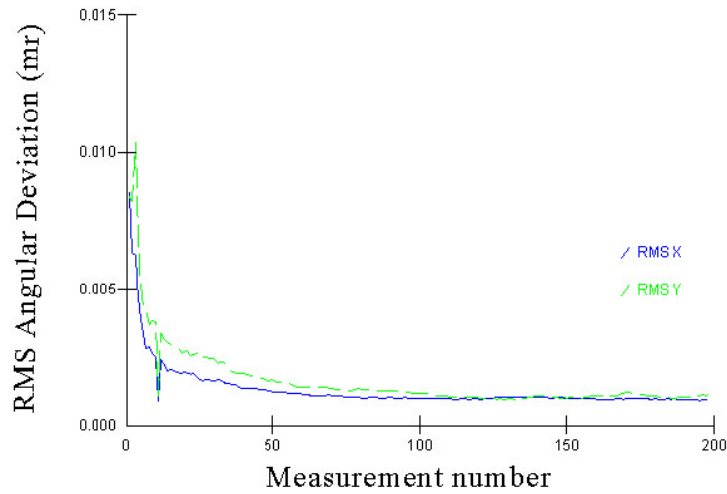


Figure 3-15: RMS angular deviation from flatness of a 100 mm diameter reference flat is shown. Running average of successive discrete wavefront measurements shows the mitigation of random error.

3.4.2 Repeatability and accuracy

The repeatability of the measurements has been primarily limited by random variations in the arc lamp caused by arc migration on the electrodes and convection currents inside the lamp [48]. Averaging 100 successive images has mitigated the effects of these variations, reducing the range of P-V surface maps to 5.0 nm (0.5 nm root-mean-squared (RMS)) over a minimum 100 mm diameter object size while the setup is unchanged, as shown in Figure 3-15. To determine the repeatability of the instrument for a human-in-the-loop environment, specimens were measured, physically removed from the metrology station, replaced and remeasured. Both the reference surface and the silicon wafer specimens were studied; results were similar. Repeatability measurements ranged 35.6 nm P-V with a 13.2 nm standard deviation. RMS surface variations ranged 14.0 nm with a 5.1 nm standard deviation.

The accuracy of the system is difficult to quantify since aberrations in the lenses will contribute different angular errors to measurements at different spatial locations. To roughly estimate the overall accuracy of the system, two flats with factory-provided interferograms were measured. These interferograms reveal non-flatnesses of

Setup	Statistic	P-V (nm)	RMS (nm)
Static			
Repeated measurements	Range	5.0	0.5
Repeatability	Range	35.6	14.0
Removed and replaced object	Std. Dev.	13.2	5.1
Accuracy			
Compared two known surfaces	Average	–	<16.7

Table 3.5: Shack-Hartmann surface metrology system performance results.

2.6 nm RMS and 4.9 nm RMS, respectively. Comparing the two flats with the Shack-Hartmann system shows an average RMS surface difference of 17.6 nm. Overlapping the interferograms, the RMS deviation can be estimated to be $\sqrt{2.6^2 + 4.9^2} = 5.5$ nm. The difference between the Shack-Hartmann and interferometric data provides a crude estimation of the accuracy of the tool. Assuming root-sum-squared (RSS) stacking of errors, a conservative estimate of the accuracy yields $\sqrt{17.6^2 - 5.5^2} = 16.7$ nm RMS. Several factors contribute to the difference between the interferograms and Shack-Hartmann measurements. The mirrors are subjected to different temperatures and mounting forces between the instruments. Additionally, the uncertainty in the interferometric measurements is estimated to be $\frac{\lambda}{50} \approx 13$ nm P-V.

In operation, the user will make a reference image with a flat, then substitute the optic under test. Based on the above analysis, the test measurement will be accurate to <17 nm and repeatable to ~ 5 nm, RMS. These results are summarized in Table 3.5.

3.5 Conclusions

A Shack-Hartmann surface metrology tool has been developed that permits metrological feedback of transparent or opaque optic foils. This instrument can be used to determine if a surface meets the 500 nm global flatness manufacturing requirement. The surface mapping data is accurate to <17 nm and repeatable to ~ 5 nm, RMS.

Non-flat figures can also be studied up to a dynamic range of $\pm 350 \mu\text{rad}$ at the object plane. The $143 \times 143 \text{ mm}^2$ square viewing range can accommodate the proposed $140 \times 100 \text{ mm}^2$ foil optic surface area.

In addition, this tool has been designed with an optic axis height and viewing range to accommodate the foil assembly truss. Active metrological feedback during the assembly procedure is important since gravity, friction, and other forces could distort the wafers beyond the assembly tolerance.

Chapter 4

Deformation and constraint of thin optics

For accurate and repeatable thin foil optic measurement and assembly, the method of holding the foil is critical. We seek to mitigate deformation from external disturbances to the upright, free standing foil to accurately measure the intrinsic warp or deformation. “Thin” is defined as a height-to-thickness ratio greater than six. The NASA *Constellation-X* mission requires constraint of foil optics of dimension $140 \times 100 \times 0.4 \text{ mm}^3$. We seek to manufacture them to less than $0.5 \text{ }\mu\text{m}$ flat peak-to-valley (P-V) on one face and assemble them to less than $1 \text{ }\mu\text{m}$ tolerance for repeatability and accuracy. The analyses presented here concern the prime material candidates for the mission, glass and silicon. We start by studying deformation of the foil as caused by environmental factors such as gravity, vibration, and thermal effects. Then, constraint effects such as friction and the number of constrain locations are considered. These analyses form the basis for a set of functional requirements about what the foil holder must do. The design resulting from these requirements is then presented.

The challenge of holding thin objects upright for measurement is of concern in applications such as flat panel displays, disk drive substrates, and lithography photomask metrology.

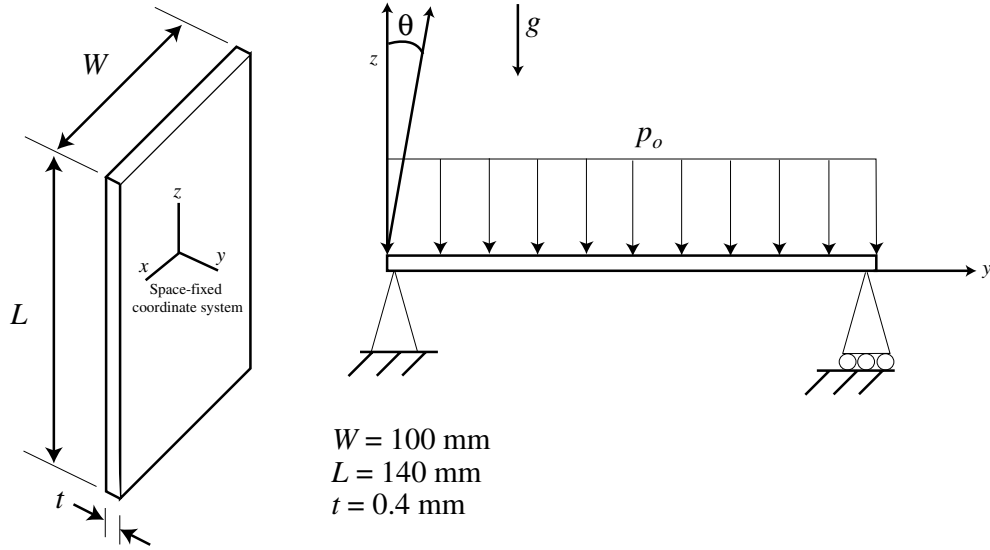


Figure 4-1: Optic foil coordinate system and 2-D beam bending model. In the beam bending model, the boundary conditions are pin joints.

4.1 Environmental concerns

Environmental factors such as gravity, vibration, and thermal disturbances must be overcome to successfully constrain the optic foil for measurement. These are addressed in the following three subsections. We first examine gravity's effect of sagging the thin foils. Top-down and bottom-up vibrations and ideas to mitigate them are next presented. For the thermal concerns, a first order analysis of the mount and optic expansion due to room temperature changes has been undertaken.

4.1.1 Gravity sag

Gravity sag is the dominant environmental concern in the constraint of the optic foils. To understand the effect of gravity on the thin materials under study, we consider both an analytical model and a Finite Element Analysis (FEA) simulation according to the coordinate system and distributed loading as shown in Figure 4-1. First, let us show that with any simply supported,* thin, floppy substrate, gravity will cause distortions on the order of the thickness. Supported horizontally, perpendicular to

*Simply supported indicates that there are “pin” joints along the edge of the “beam” as shown in Figure 4-1.

Material	90° inclination	0.82° inclination
	horizontal	nearly vertical
	δ_{\max} (μm)	δ_{\max} (μm)
Aluminum	145.08	2.08
Silicon	53.65	0.77
Glass	126.71	1.81

Table 4.1: Deformation at foil centerline for three materials at pitch = 90° (perpendicular to gravity) and pitch = 0.82° (nearly aligned with gravity). Dimensions: 140×100×0.4 mm³, Boundary conditions: pin joints.

gravity, as shown in Figure 4-1, the optic foil’s maximum deformation will occur at the foil centerline as given by

$$\delta_{\max} = \frac{5p_o L^4}{384EI} \quad (4.1)$$

where p_o is the force per unit length on the beam, E is the Young’s modulus, and I is the moment of inertia with respect to the y -axis. The force per unit length is defined as

$$p_o = \frac{mg \sin \theta}{L} \quad (4.2)$$

where m represents the mass of the optic foil, g is the acceleration due to gravity, equal to 9.81 m/s², and θ is the inclination with respect to gravity as shown in Figure 4-1. The moment of inertia is

$$I = \frac{Wt^3}{12}. \quad (4.3)$$

Combining these equations yields the relation

$$\delta_{\max} = \frac{\rho g \sin \theta L^4}{6.4Et^2} \quad (4.4)$$

Using this equation, the deformation for the two optic foil candidates and a reference material, aluminum, can be calculated as shown in Table 4.1. Since our goal is to manufacture the optic foils to a flatness of 0.5 μm , constraining the foils for measurement in this horizontal manner with pin boundary conditions at the foil edges will not be acceptable. The gravity-induced load can effectively be reduced by orienting

the foils vertically. If a hypothetical vertical misalignment of 2 mm at the top of a 140 mm foil exists, then the resulting angle of inclination, or pitch, of 0.82° inserted into Equation 4.4 yields deformations given the right column of Table 4.1.

Let us turn the analysis over to FEA to more accurately compute the deformation since the deformed foil shape is truly three-dimensional, and the analytical models only predict two-dimensional deformation. In addition, FEA can allow us to vary parameters more easily and evaluate deformation with more realistic boundary conditions. To validate the quality of the simulations, we compare the FEA-computed deformation to the simply supported beam as previously described. The FEA yields a maximum displacement of $1.87 \mu\text{m}$ for the glass with dimensions $140 \times 100 \times 0.4 \text{ mm}^3$, pitch of 0.82° , and pin boundary conditions of Figure 4-1. This value compares well with the $1.81 \mu\text{m}$ analytical beam bending result from Table 4.1.

Boundary conditions

To accurately simulate the real optic foil distortion from gravity, we first need to use more realistic boundary conditions. We have previously been assuming a pin joint that runs the length of the top and bottom of the foil as shown in Figure 4-2*a*. The assembly truss discussed in Chapter 2 instead uses a three-point contact to manipulate the foils. Indeed, to avoid overconstraint in practice, we should only contact the foil's edges at three locations. Therefore, to accurately model the assembly truss performance and serve as a baseline for additional constraint study (See Subsection 4.2.1), we adopt the boundary conditions as depicted in Figure 4-2*b*. In general, this triad of ball-socket joints will allow more foil sag due to gravity than the pin joint edges. A simple FEA simulation for glass reveals a maximum deformation of $2.14 \mu\text{m}$ as compared with the previous result of $1.87 \mu\text{m}$, respectively, for a foil with dimensions $140 \times 100 \times 0.4 \text{ mm}^3$ and pitch of 0.82° .

One last perturbation of the boundary conditions was considered. In reality, the upper foil constraint in Figure 4-2 (*a* and *b*) is not restricted from translation in the vertical direction. In other words, under large deformation, the top of the foil will slide down relative to that joint position. An FEA analysis revealed only angstrom

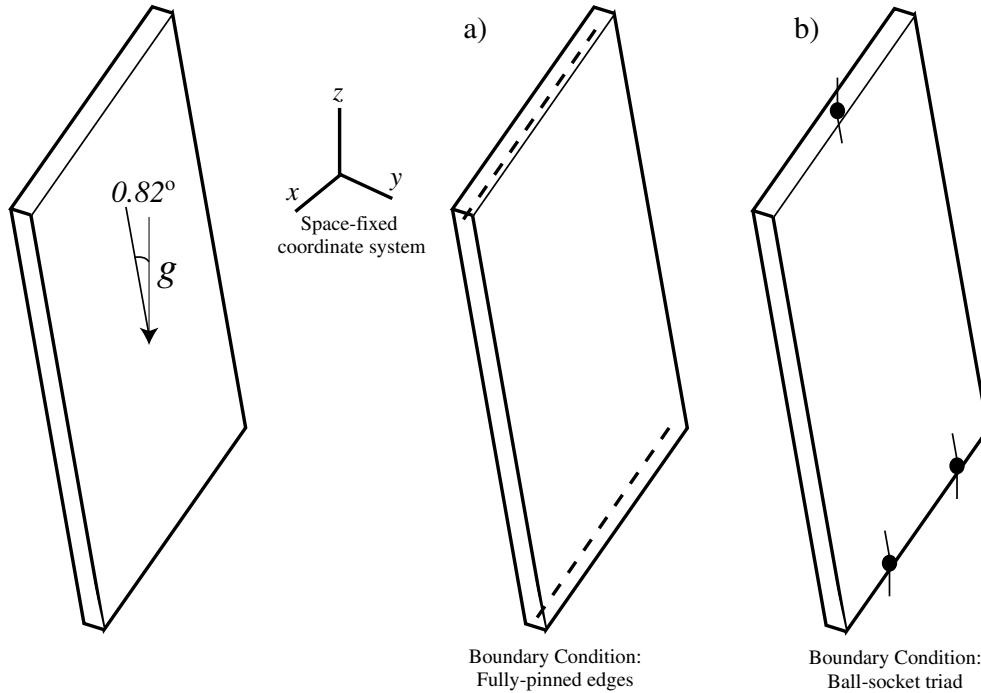


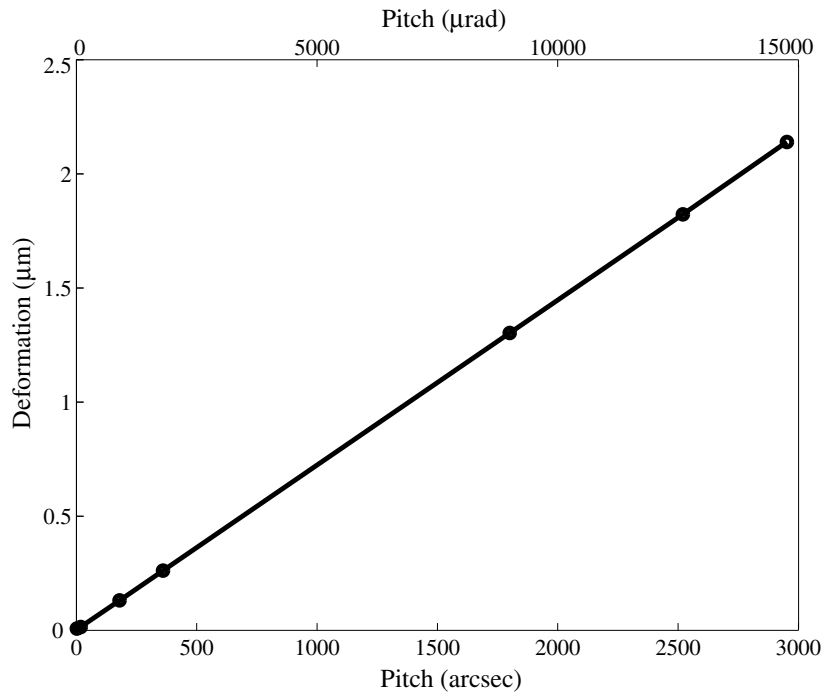
Figure 4-2: The pin joint constraint (a) allows rotation about the x -axis only, and no translation of the joint. The ball-socket triad (b) permits rotation about all three axes, and no translation.

magnitude differences in the maximum deformation with and without this variation. Subsequent analyses therefore assume the translation and rotation constraints as given in Figure 4-2b.

Gravity sag as a function of pitch angle

Now we are prepared to evaluate the foil deformation as a function of pitch angle. Given the boundary conditions from Figure 4-2b, this relationship is plotted in Figure 4-3. Equations to predict deformation corresponding to small angles are given in the figure as well. The proportionality relationship corresponds to the linear behavior of the sine function at small angles.

These results help to define the foil holder functional requirements. Specifically, if we allocate 15% of the allowable P-V error (500 nm) to the pitch angle repeatability, then the pitch angle repeatability should be at worst ~ 100 arcsec. The corresponding ~ 70 nm glass foil deformation due to repeatability error should not significantly



$$\frac{\delta_{max} (\mu\text{m})}{m} = \theta$$

arcsec	0.00072
μrad	0.00015
degree	2.60718

Figure 4-3: Maximum deformation of the glass foil as a function of pitch angle. Dimensions: $140 \times 100 \times 0.4 \text{ mm}^3$, Boundary conditions: ball-socket triad.

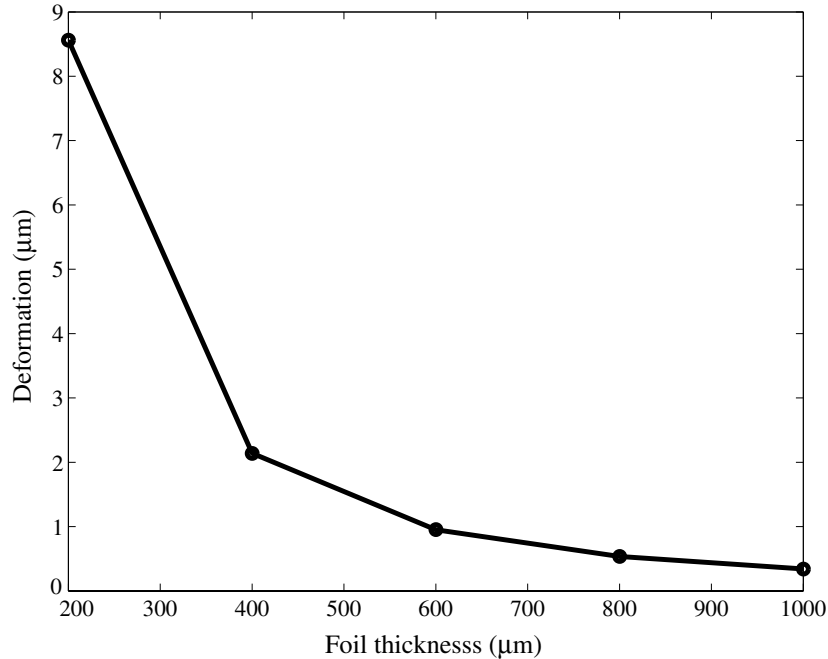


Figure 4-4: Maximum deformation of the glass foil as a function of thickness. Dimensions: $140 \times 100 \times t \text{ mm}^3$, Boundary conditions: ball-socket triad. Angle of inclination: 0.82° .

compromise assessment of the flattening process efficacy.

Gravity sag as a function of foil thickness

The thickness of the optic foil will affect how tolerant we can be of inclination errors. A unit analysis of Equation 4.4 reveals that the deformation is inversely proportional to the thickness squared. This dependency can also be determined from the parallel axis theorem, which indirectly reveals a design philosophy: the stiffness of a design goes with the square of the distance of the structural members from the neutral axis [59].

Indeed, a simple FEA analysis reveals not only this trend but also the magnitude of the displacements as a function of thickness. Holding the angle of inclination constant at 0.82° , we construct Figure 4-4. As in the previous analysis, we maintain the Figure 4-2*b* ball-socket triad.

The thickness choice of $400 \mu\text{m}$ for the optic foils balances the need for a relatively low mass telescope with the need to keep deformations small with stiff foils. Judging

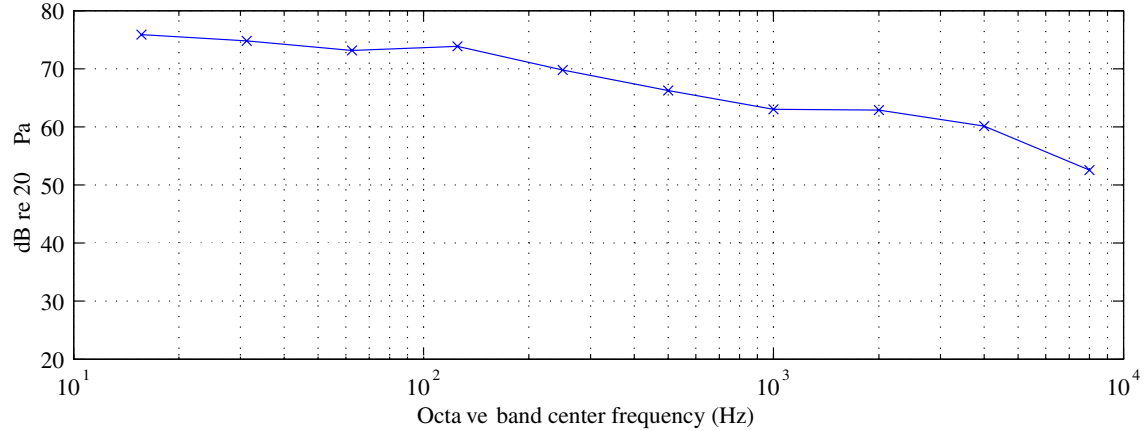


Figure 4-5: Acoustics measurements of the environment inside the MIT *Space Nanotechnology Laboratory*.

from Figure 4-4, the constraint challenge complexity appears to scale with the inverse of the thickness squared as well.

4.1.2 Vibration

Vibration induced excitation can come from the floor or from the “top-down.” The floor vibrations (“bottom-up”) are likely to be in the 1-10 μm amplitude regime and could span the frequency range from 5-500 Hz [60]. Top-down excitations are caused mainly by acoustics, with the 10-100 Hz range being of primary concern, and dominating over 50 Hz. The sound pressure levels have been measured in the MIT *Space Nanotechnology Laboratory* cleanroom [61] and are shown in Figure 4-5. These driving forces can be a problem for metrology and assembly since the first six optic foil vibration modes have been theoretically computed by Mongrard [1] to be 86 Hz, 136 Hz, 255 Hz, 316 Hz, 328 Hz, and 519 Hz for the $140 \times 100 \times 0.4 \text{ mm}^3$ glass foil.

Bottom-up vibration problems were avoided before they surfaced by selecting a vibration isolation table on which to build the setup. Although the Shack-Hartmann technology is relatively insensitive to vibration, the design does have more than three meters of optical path length. Additionally, averaging of successive images with the Shack-Hartmann software is most effective if vibrations are minimized.

A broadband passive damping system was selected as a relatively low cost solution

to the bottom-up vibration. This systems supports a breadboard using four pneumatic legs. They are designed to attenuate frequencies from 5-500 Hz. Broadband damping results in lower response at all frequencies as opposed to tuned damping, in which tuned vibration absorbers contribute to lower dynamic deflection at only the table’s fundamental modes. The broadband scheme remains effective regardless of changes of mass loading on the table or floor excitation frequencies.

For this work, top-down excitation was not addressed beyond measurement of the *Space Nanotechnology Laboratory* “white noise” acoustic characteristics. A baffling structure could be explored in more detail in future work if concerns persist. Additionally, the resonant frequencies of the mounting structures on the breadboard, somewhere in the teens of Hz, can excite modes in the foils.

4.1.3 Thermal considerations

Thermal expansion in the mounting device and optic foils could lead to undesirable deformation. Understanding the sources and magnitude of these effects must therefore be considered. First, symmetry can be a powerful design tool to minimize thermal errors [59]. In the design of the foil fixture, angular errors are reduced by the symmetric support of elements.

Thermal expansion mismatch between the foil optic and its holder could inhibit accurate metrology. Since aluminum is relatively cheap, available, and machinable, we shall consider this material for the foil holder in this first order analysis. The thermal expansion is governed by

$$\Delta L = L\alpha_{th}\Delta T \tag{4.5}$$

where L is the starting length, α_{th} is the thermal expansion coefficient, and ΔT is the uniform temperature change to which the material is subjected. A temperature change of 7°C (12.6°F) is possible in the span of several hours in the *Space Nanotechnology Laboratory’s* metrology room which does not have a temperature control system installed as of this writing. The thermal sources responsible for this tempera-

Equipment	Power (W)
Computers	$3 \times 350 = 1050$
Pwr Supply, Camera	200
Pwr Supply, Voltage	300
Pwr Supply, Arc Lamp	200
Pwr Supply, Autocollimator	10
Personnel	$3 \times 100 = 300$
Pwr Supply, Picomotors	10
Total	$2070 W$

Table 4.2: Heat sources in the MIT *Space Nanotechnology Laboratory* metrology room.

	ΔL (μm)
Aluminum	22.5
Glass	7.1
Silicon	3.6

Table 4.3: Linear thermal expansion of 140 mm long foil substrates and aluminum fixture in response to 7°C (12.6°F) environment temperature change.

ture change are shown in Table 4.2. With the characteristic foil length of 140 mm, the respective thermal expansions of the foil and holder candidate materials are shown in Table 4.3. These values are computed from the thermal expansion coefficients given in Table 2.1 and using Equation 4.5.

The resulting differential change in length of $\sim 15 \mu\text{m}$ between the aluminum and glass could change the foil shape and induce stress and deformation if the holder does not allow slip at the contact points. Figure 4-6 shows how this could occur. Assuming the distance between the folder holder clamps increases vertically by $15 \mu\text{m}$ due to thermal expansion for the 140 mm long foil, a conservative estimate of the reduction in foil warp is

$$h = \sqrt{\left(\frac{140 \text{ mm}}{2}\right)^2 - \left(\frac{140 \text{ mm} - 0.015 \text{ mm}}{2}\right)^2} = 1025 \mu\text{m} \quad (4.6)$$

from the Pythagorean theorem, where h is the reduction in warp. For a more accurate

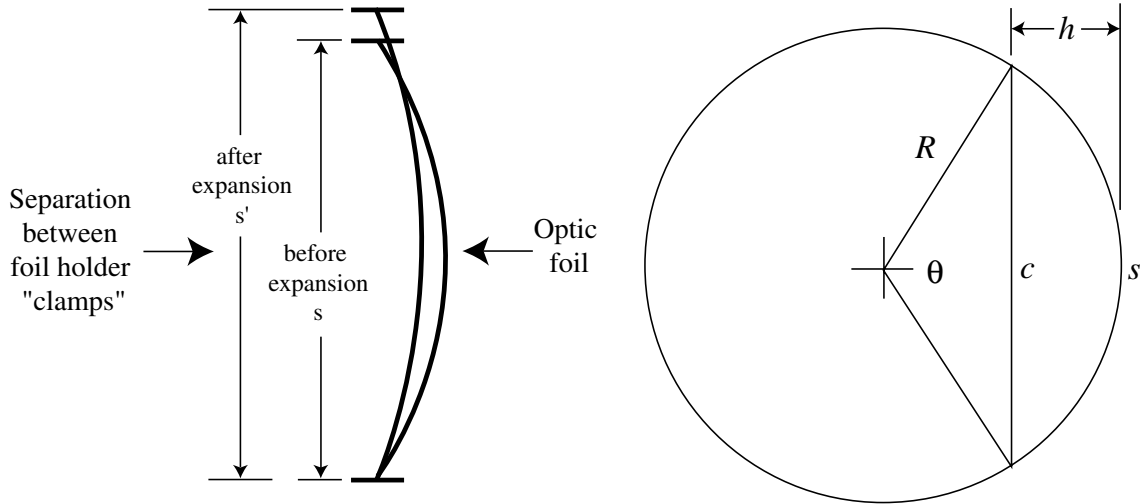


Figure 4-6: Thermal expansion mismatch causes the foil holder clamps to separate by $15 \mu\text{m}$ more than the foil length increases. This reduces the perceived warp if the boundary conditions do not allow slip (*left*). The circle geometry is used to calculate this reduction in warp (*right*).

estimate, the geometry of the circle in Figure 4-6 can be manipulated to show that

$$\frac{2s}{c} = \frac{\theta}{\sin \frac{\theta}{2}}. \quad (4.7)$$

Since $s = R\theta$, we can find R from the known s and c . Also from geometry,

$$h = R - R \cos \frac{\theta}{2}. \quad (4.8)$$

Using this equation for the same problem with $s = 140 \text{ mm}$ and $c = 139.985 \text{ mm}$, $h = 888 \mu\text{m}$. This is much larger than the $0.5 \mu\text{m}$ tolerance. Thus, a functional requirement of the fixture design becomes clear—the foil holder should permit sliding between the foil and its clamps if the materials and temperature changes are on the order described here. The functional requirements are outlined in subsection 4.3.1.

Temperature gradients caused by touching the glass with relatively hot fingers could cause local distortions on the order of tens of nanometers. The time constant of this distortion would be no more than one minute, as observed with interferometry of thicker glass substrates.

4.2 Mounting effects

Having considered the environmental factors, we now turn to the foil fixture itself. We first analyze the constraint locations to determine how many fixture/foil contact points we need and where to put them. Secondly, friction that occurs while placing the foil into the fixture will be studied to estimate whether the design should avoid or compensate for this potentially distorting force.

4.2.1 Constraint locations

The number and location of contact points between the foil and its holder will directly affect the foil's sag if it is not vertically aligned with gravity. In Subsection 4.1.1, we mentioned that the gravity sag for a glass foil of dimensions $140 \times 100 \times 0.4 \text{ mm}^3$ and inclined at 0.82° was $1.87 \text{ }\mu\text{m}$ for the pin joint edges in Figure 4-2*a* and $2.14 \text{ }\mu\text{m}$ for the ball-socket triad boundary conditions in Figure 4-2*b*. We now consider varying the number of constraining points, from just one on the top and bottom edge to infinite (pin joints). This analysis will reveal the function relating the boundary conditions.

In addition, we will also show the displacement of the glass foil as a function of the number of constraint points for a boundary condition in which rotation is not permitted. This analysis is useful as it relates to gluing the optic foil into the flight module as discussed in Subsection 2.6.3. Figure 4-7 shows the deformation for these two cases. From this plot, more contact points with the foil appear to be “better” by reducing the gravity deformation for a given angle of inclination. However, we must not overconstrain the foil during metrological inspection—this would induce the deformation we are trying to avoid! Therefore, we recommend the boundary condition using only three contact locations for the foil holder. During assembly of the optic foils, however, we can tolerate overconstraint when gluing the optic foils into the flight module. From the solid line in Figure 4-7 we can predict the deformation of these optics from the number of boundary conditions for an angle of inclination of 0.82° . Recall that we can safely extrapolate to other angles from Figure 4-3.

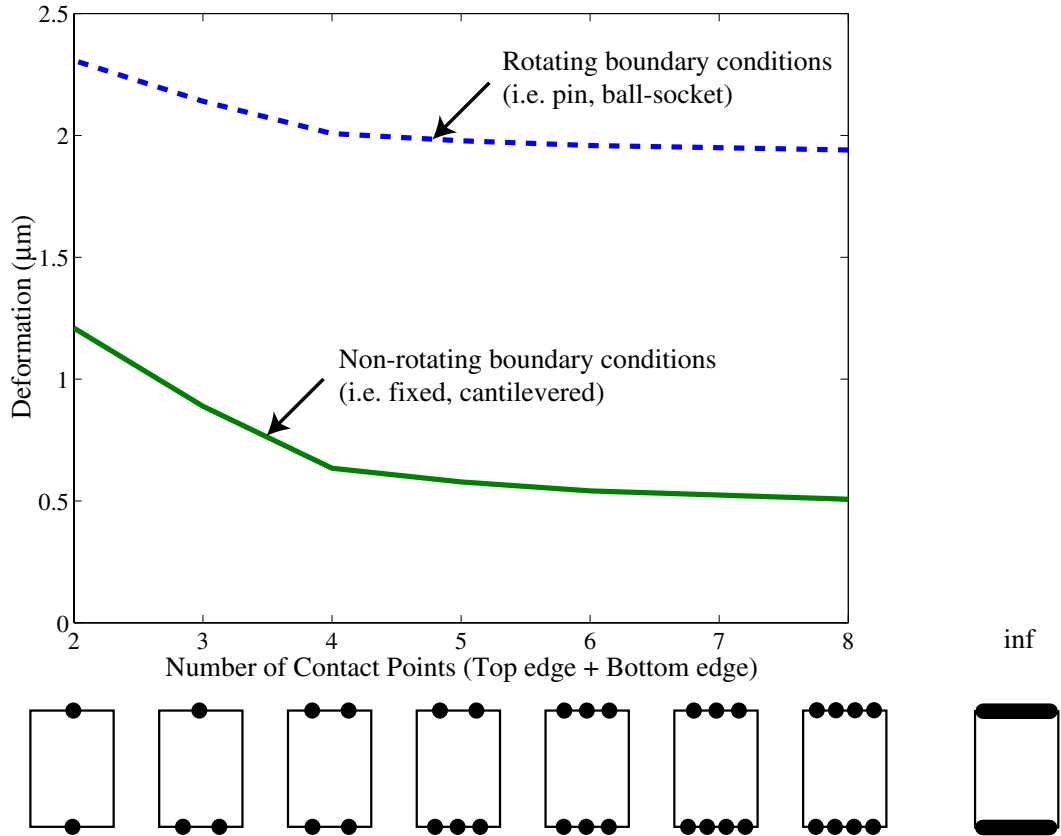


Figure 4-7: Deformation of the glass foil decreases as the number of constraint locations increases. The deformation asymptotically approaches $0.37 \mu\text{m}$ and $1.87 \mu\text{m}$ for the non-rotating and rotating boundary conditions, respectively, as the number of contact points goes to infinity (pin joints). Dimensions: $140 \times 100 \times 0.4 \text{ mm}^3$, Angle of inclination: 0.82° .

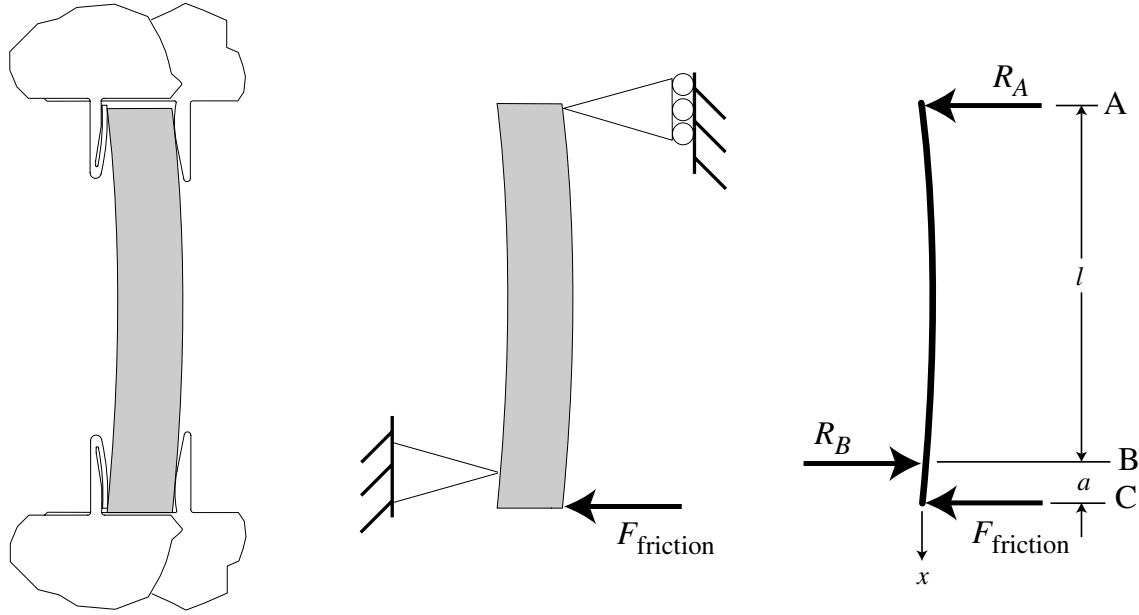


Figure 4-8: The actuation force of the spring comb combined with the friction force at the bottom of the foil can lead to distortion. Using pin joints and a 2-D beam bending analysis, we can estimate the magnitude.

4.2.2 Friction

Frictional forces can distort the optic foils beyond their manufacturing and assembly tolerances. In this analysis, we consider an assembly scenario where the foils are slid into an aligned position by the microcomb structures as in the assembly truss discussed in Chapter 2. The actuation force is provided by the microcomb tooth, and friction arises from contact between the optic foil and the microcomb base. This is depicted in Figure 4-8. For analytical study, consider pin joint boundary conditions that run the length of the top and bottom of the foil as shown in this figure. This crude approximation should get us in the ballpark, and pave the way for verification by FEA simulations later. To compute how much force the bottom microcomb tooth applies, we first consider the friction force at the bottom of the foil. This force is given by

$$F = \mu mg = (0.39)(14.1 \text{ g})(9.807 \text{ m/s}^2) = 0.054 \text{ N} \quad (4.9)$$

where μ , the coefficient of static friction, has been measured by Mongrard [1, pages 167-169]. The mass is computed for the glass sheet of dimensions $100 \times 140 \times 0.4 \text{ mm}^3$.

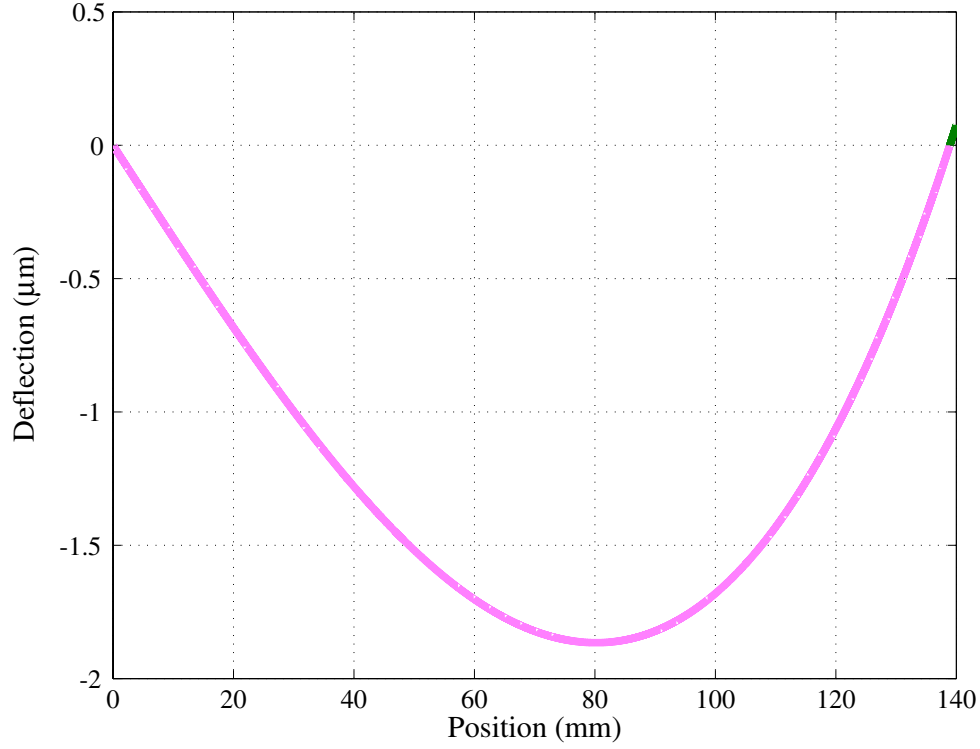


Figure 4-9: Analytical result for foil deformation due to friction.

The length a between the friction force location and the reaction force is the difference between the reference comb/spring comb height, 0.41 mm, and the spring comb tooth/base height, 1.5 mm. The total foil length, L , is 140 mm, so in Figure 4-8, $a = 1.09$ mm and $l = 138.91$ mm. From a static analysis, the reaction forces are

$$|R_A| = \frac{Fa}{l} = 0.0004 \text{ N} \quad (4.10)$$

$$|R_B| = \frac{F(l+a)}{l} = 0.0542 \text{ N}. \quad (4.11)$$

From these forces, the deflection of the “beam” is shown in Figure 4-9. The equations which govern this behavior are

$$\delta_{AB} = \frac{Fax(l^2 - x^2)}{6EI} \quad (4.12)$$

$$\delta_{BC} = \frac{F(x-l)}{6EI} [(x-l)^2 - a(3x-l)] \quad (4.13)$$

for the regions before and after B, respectively, and the maximum beam deflection is

$$\delta_{\max} = \frac{Fa^2(l+a)}{3EI} = 1.9 \mu\text{m} \quad (4.14)$$

which occurs at

$$x_{\max} = \sqrt{\frac{l^2}{3}} = 80.2 \text{ mm}. \quad (4.15)$$

This deformation is larger than tolerable and it occurs near the center of the foil. An FEA simulation was performed to more accurately analyze this effect. The boundary conditions were changed to the ball-socket triad as before, with the two bottom ball-socket joints positioned appropriately 1.09 mm from the bottom of the foil. The result of this simulation is a maximum deformation of 2.76 μm . Gravity is not a factor in these results. The FEA and analytical data compare well.

These results indicate that the force of friction can deform the foil beyond manufacturing and assembly tolerances. Some reassurance is possible, since the results were obtained for a conservative coefficient of friction [1, pages 167-169], and the friction force was a maximum (at the verge of slipping). Still, there should be additional FEA analysis performed and experimental validation before design changes are implemented in hardware. These design changes could include low friction coating on the microcombs and some method of stress relief for the bottom foil edge such as flexures or vibration.

4.3 Foil optic fixture design

4.3.1 Functional requirements

To design the foil fixture, a set of functional requirements was developed which consider the metrology system to be used, the foil candidates, and the preceding analyses. These requirements are the basis for the design to be presented in the next section and can serve as guidelines for a future generation of foil fixture. The functional requirements are as follows:

1. Support the foil for metrology to be performed on one face without substantial obstruction[†] and without overconstraint.
2. Allow control of degrees of freedom (coordinate system shown in Figure 4-2):
 - pitch (rotation about x -axis)—Sufficient to orient foil vertically with a repeatability of <100 arcsec. Resolution <30 arcsec (1/3 of repeatability). Vertical accuracy should be better than 100 arcsec to keep foil deformation well below the flatness tolerance. The allocation to the total deformation error budget of 500 nm for the pitch repeatability is 15%. We reserve the remaining 85% for the foil manufacturing process variation.
 - yaw (rotation about z -axis)—Sufficient to put foil optic in angular viewing range of metrology tool.[‡] Resolution <30 arcsec.
 - x -axis translation—Sufficient to put foil in metrology instrument lateral viewing range.[§] Resolution <1 mm. Range >12.7 mm. Repeatability <0.25 mm.
 - z -axis translation—Sufficient to put foil in metrology instrument vertical viewing range.[¶] Resolution <1 mm. Range >70 mm to keep different size foils centered within the metrology tool optical path (See #5). Repeatability <0.25 mm.
3. Permit human to insert and remove optic foil from device.
4. Accommodate thermal expansion mismatch between optic and fixture.
5. Allow for optic foils of rectangular dimensions $140 \times 100 \times 0.4$ mm³, $140 \times 100 \times 0.2$ mm³, or diameter 100 mm \times 0.4 mm thick and of materials silicon, borosilicate glass, and ultra-low-expansion glass.

[†]Obstructions should permit evaluation of P-V surface mapping over clear aperture (90%) of foil. Obstructions can be tolerated if localized since the foil could be repositioned within the instrument field of view to measure previously blocked region.

[‡]For the Shack Hartmann metrology system, the angular viewing range is 350 μ rad (72 arcsec). Note that for a not flat optic, the angular alignment of the fixture must be within the instrument range minus the maximum angular surface deviation.

[§]For the Shack Hartmann metrology system, the lateral viewing range is 142 mm.

[¶]For the Shack Hartmann metrology system, the vertical viewing range is 142 mm.

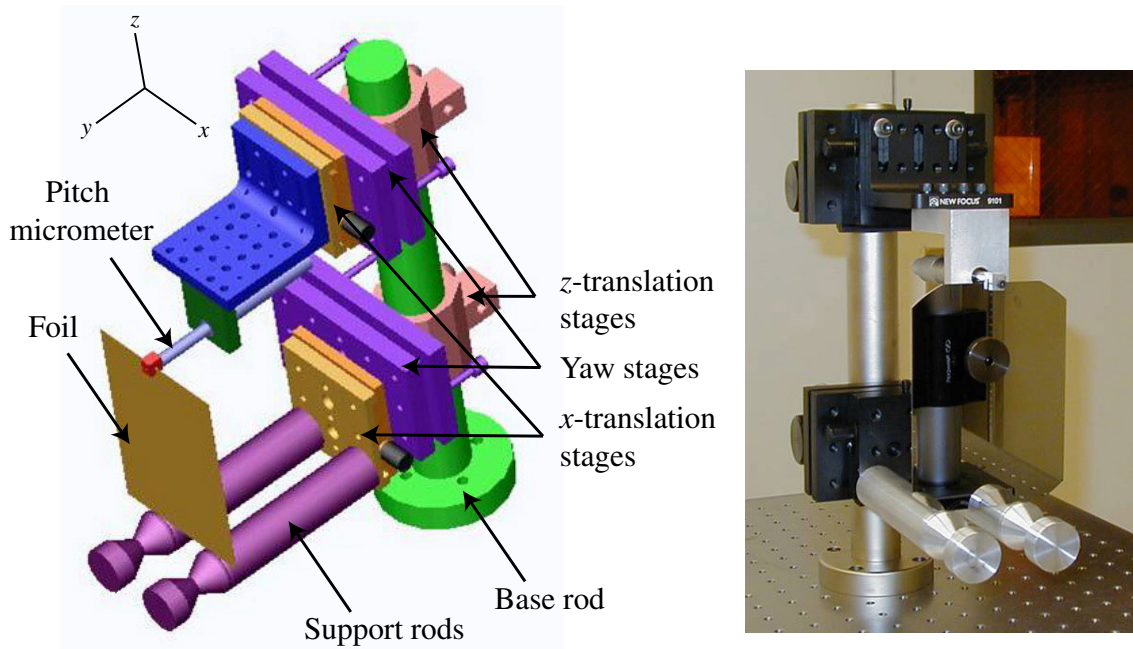


Figure 4-10: The foil holder allows two rotational and two translational degrees of freedom for the optic foil. The visible face of the foil can be mapped by a metrology tool.

From these requirements, concept generation progressed to the design and fabrication of the foil fixture.

4.3.2 Design

The fixture designed for thin foil metrology in the MIT *Space Nanotechnology Laboratory* is shown in Figure 4-10.

The performance of the system can be characterized by the range and resolution of control of the degrees of freedom as outlined in the previous section. These parameters are summarized in Table 4.4. To minimize overconstraint, three contact areas are used—one near the top and two along the bottom edge. The one at the top is a point contact between a sphere and the foil. Along the bottom, the foil edge rests in two vee-grooves. There is some overconstraint here which could cause local torques and deformation. This was determined acceptable for simplicity of foil loading by the operator, low cost, and quick fabrication of the device.

Degrees of freedom	Range	Sensitivity
pitch (140 mm tall foil)	± 18500 arcsec	1.5 arcsec
pitch (100 mm tall foil)	± 26000 arcsec	2 arcsec
yaw	± 50400 arcsec	11 arcsec
<i>x</i> -axis translation	± 12.7 mm	4 μm
<i>z</i> -axis translation	> 150 mm	< 1 mm

Table 4.4: Foil holder performance for four degrees of freedom.

4.4 Conclusions

To meet thin foil optic assembly and metrology challenges, we have presented how thin materials such as silicon wafers and glass sheets deform and how they can be constrained to minimize these effects. Both finite element analyses (FEA) and analytical calculations have been utilized to understand the effects of gravity on foil deformation while varying parameters such as foil thickness and pitch angle. Frictional forces imparted during foil manipulation have also been studied. Foil vibration amplitudes, sources, and mitigation were considered as well. Thermal expansion mismatch between the foil and constraint device was also evaluated.

These theoretical analyses formed the basis for a set of functional requirements for the design of a foil fixture—a device which can hold these thin, floppy foils with kinematic mounting and minimal deformation. We presented a quasi-kinematic foil constraint tool that utilizes a ball and two vee-grooves to position a foil with angular repeatability in pitch of less than 30 arcsec. This reduces the foil deformation repeatability due to gravity to less than 20 nm peak-valley (P-V) over a 140 mm length.

Appendix A

Assembly truss angle-to-linear displacement conversion

An autocollimator is used to measure the angles, pitch and yaw, of the planar optic surface in the assembly truss. To verify that the truss can align foils to sub-micron tolerance goals, these angles must be converted to linear displacements.

Here, the angle-to-displacement conversion originally formulated by Mongrard [1] is presented. Notable points are interjected, and of course, the final dimensioned results apply to the current assembly truss research.

A.1 Derivation

The Cartesian coordinate system orientation will be continued from the error budget analysis. The origin, however, will be located as shown with the optic foil in Figure A-1. The contact points between the foil and microcombs are given by P_i . From this figure, the three points of contact between the foil and microcomb teeth are defined in (x, y, z) coordinates as

$$P_1 = \begin{bmatrix} A/2 \\ \delta y_1 \\ B \end{bmatrix}, \quad P_2 = \begin{bmatrix} 0 \\ \delta y_2 \\ 0 \end{bmatrix}, \quad P_3 = \begin{bmatrix} A \\ \delta y_3 \\ 0 \end{bmatrix}.$$

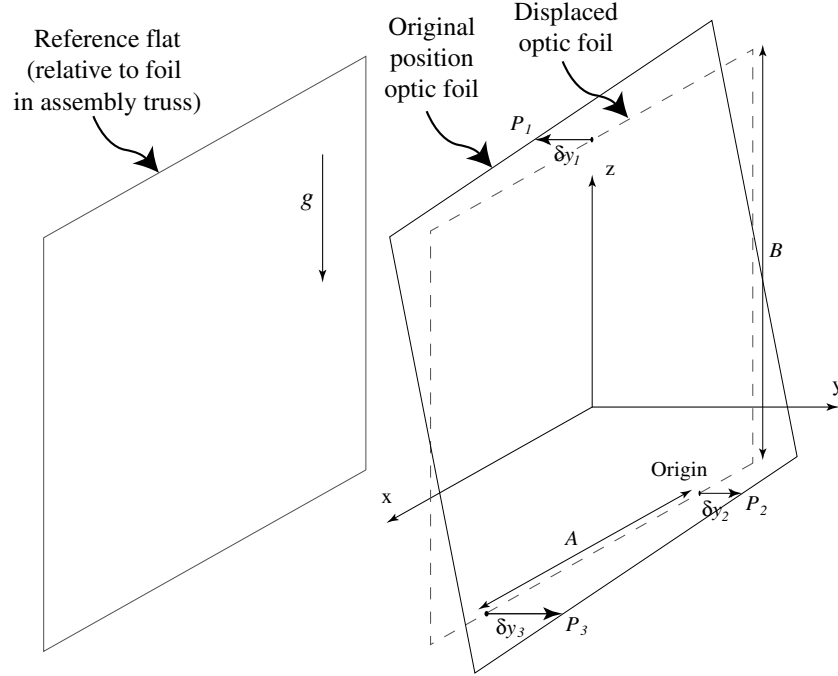


Figure A-1: The foil is shown with definitions to be used in the angle-to-displacement conversion derivation.

Notably, these contact points only translate along the y -axis as the sheet is rotated in pitch and yaw. Although the sheet itself undergoes rigid body rotation, the contact points translate along its surface so that their spatial separation in x and y remain constant. The relative linear displacement error between the two microcombs at the bottom, δy , and displacement error between the bottom and top microcombs, δp , are given by

$$\delta y = \delta y_3 - \delta y_2 \quad (\text{A.1})$$

$$\delta p = \delta y_1 - \frac{\delta y_2 + \delta y_3}{2}. \quad (\text{A.2})$$

As Mongrard [1] has previously noted, the three points P_i define a plane. The vector \vec{n} normal to this plane can be computed from the cross product of $P_1\vec{P}_2$ and $P_1\vec{P}_3$ as

$$\vec{n} = \begin{bmatrix} -A/2 \\ \delta y_2 - \delta y_1 \\ -B \end{bmatrix} \wedge \begin{bmatrix} A/2 \\ \delta y_3 - \delta y_1 \\ -B \end{bmatrix} = \begin{bmatrix} B \cdot (\delta y_3 - \delta y_2) \\ -A \cdot B \\ -A/2 \cdot (\delta y_3 + \delta y_2 - 2\delta y_1) \end{bmatrix} = \begin{bmatrix} B \cdot \delta y \\ -A \cdot B \\ A \cdot \delta p \end{bmatrix}.$$

The yaw and pitch of the optic foil with respect to the reference flat can be read on the autocollimator. The yaw reading is the angle between the y -axis and the projection of \vec{n} onto the (x, y) plane. Similarly, the pitch reading is the angle between the y -axis and the projection of \vec{n} onto the (y, z) plane. Therefore,

$$\tan(\text{yaw}) = n_x/n_y = -\delta y/A \quad (\text{A.3})$$

$$\tan(\text{pitch}) = n_z/n_y = -\delta p/B. \quad (\text{A.4})$$

Making the small angle approximation for the tangent (measurements are typically less than $200 \mu\text{rad}$) and substituting $A = 55 \text{ mm}$, $B = 140 \text{ mm}$ for the current design results in

$$\delta y (\mu\text{m}) = 0.06 \text{ yaw } (\mu\text{rad}) \quad (\text{A.5})$$

$$\delta p (\mu\text{m}) = 0.14 \text{ pitch } (\mu\text{rad}). \quad (\text{A.6})$$

Appendix B

Conceptual designs for the assembly truss

The conceptual design phase of the assembly truss project included many hand sketches and subsequent primitive solid models. This appendix includes only those ideas which were considered viable. Figure B-1 shows some initial ideas for constraining a foil's six degrees of freedom. Figures shown in pages 155 through 159 show more detailed solid models where various permutations of the moving parts were considered. In Figure B-2, all of the parts are built up vertically in a repeatable assembly around a stationary flight module containing the foils. Figure B-3 illustrates another possibility, where the assembly structure is rigid and stationary and the flight module is dropped in for alignment. Another possibility is shown in Figure B-4. In this "L-truss" design, the flight module is inserted into the vertex of the L and the remaining parts of the truss are slid around it. Figure B-5 shows how the reference flat and flight module could be stationary while both of the alignment members of the truss are positioned. This concept is rotated to a vertical configuration in Figure B-6. The design of the flight module was first explored with solid modeling in Figure B-7.

Figure captions provide additional details regarding the assembly procedure and design considerations.

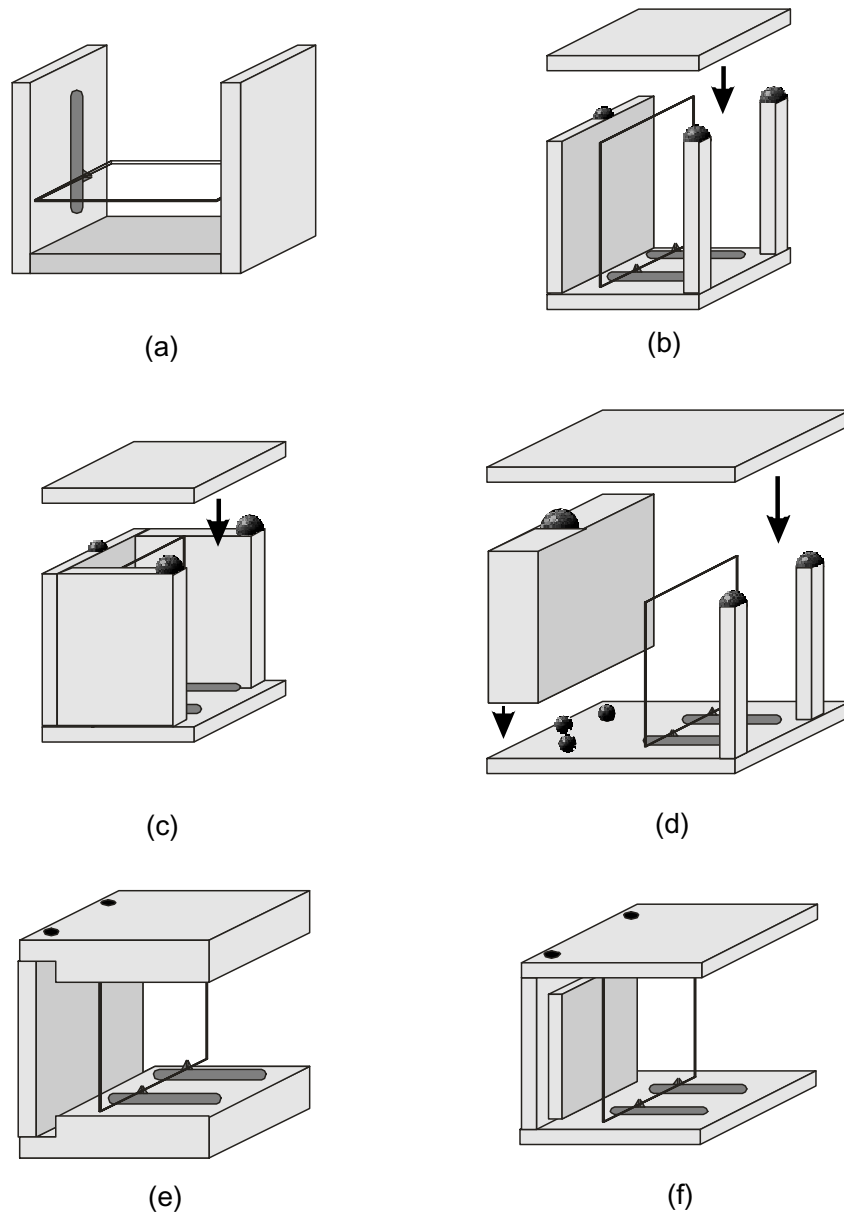


Figure B-1: Initial concepts illustrating some techniques for meeting the functional requirements for the design. The glass foil is shown as a transparent rectangle. The microcombs are depicted as gray bars. Design (a) was eliminated since the relatively large deformation of the thin foils due to gravity sag would be unacceptable. This problem of gravity deformation is explored in more detail in Chapter 4. Kinematic balls sketched in (b-d) permit repeatable assembly of the truss. Design (c) unnecessarily restricted user access to the microcombs. Design (e) is different from (f) in that the reference surface is not a structural member and is instead mounted kinematically to the vertical support.

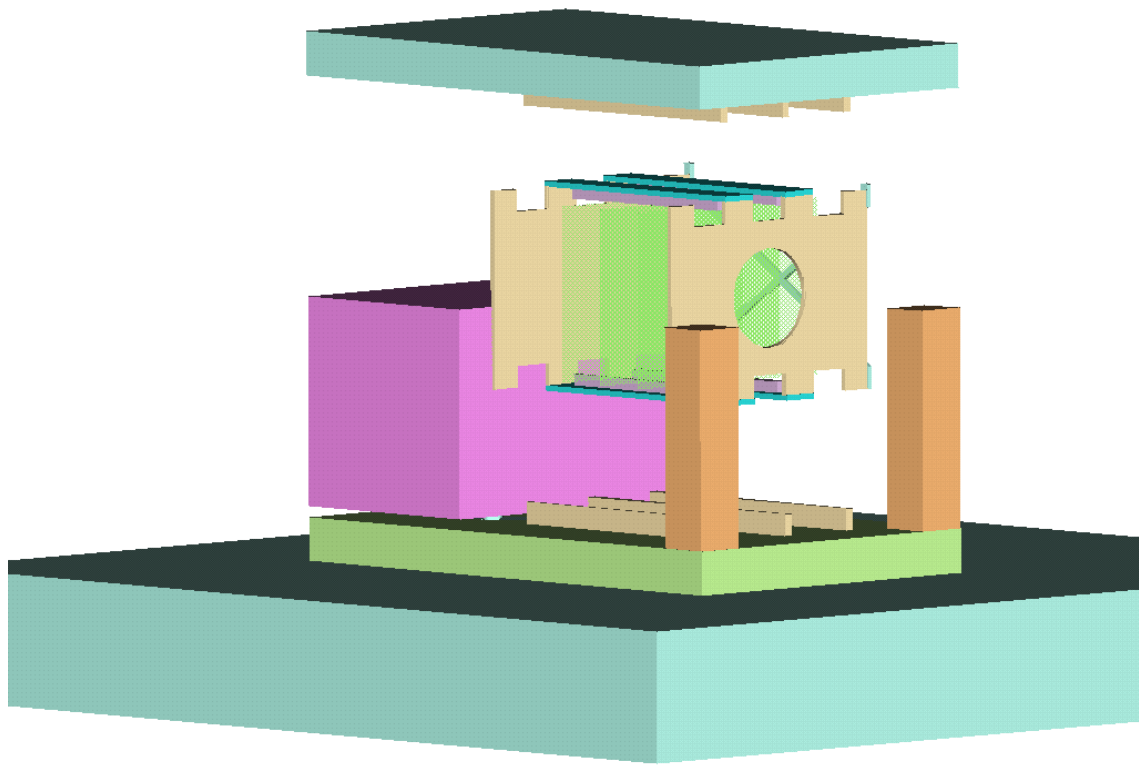


Figure B-2: In the “stack” concept, the flight module would be placed into the truss and the lid would be set on top. Kinematic couplings (not shown) at critical interfaces would ensure repeatable assembly. Gravity deflection of the lid and deformations of the reference flat were concerns.

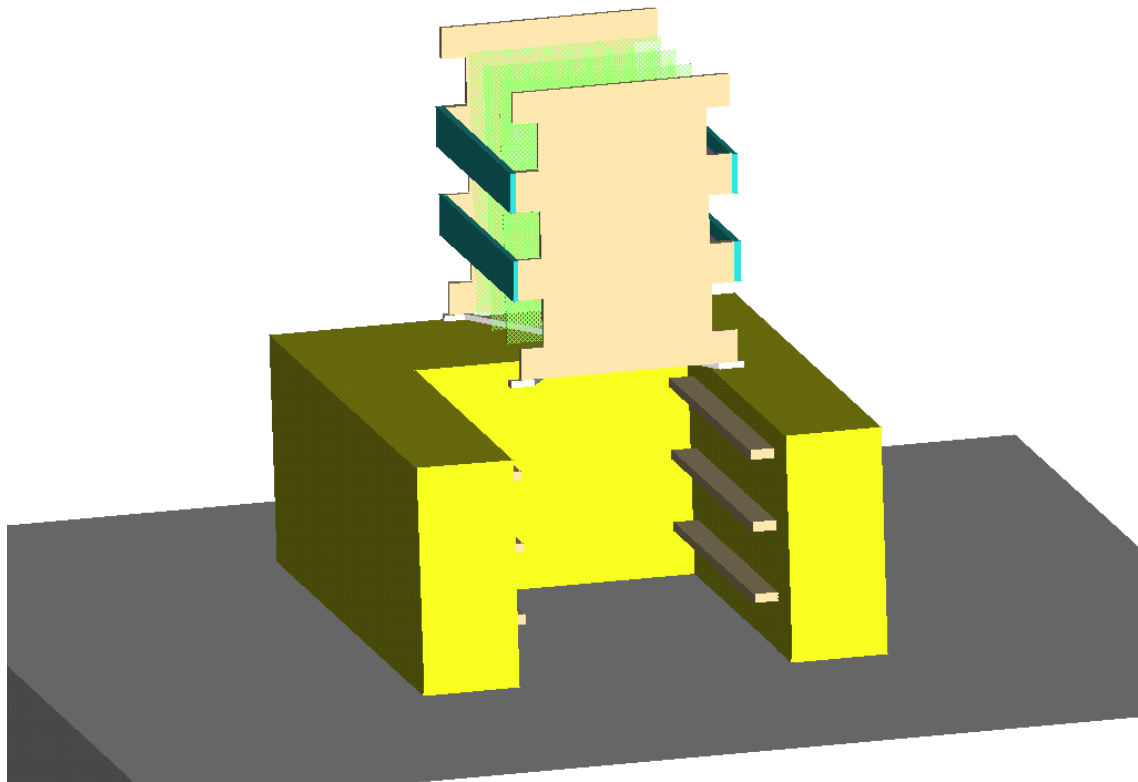


Figure B-3: The fixed truss concept would involve sliding the flight module down into a rigid truss on guide ways, rails, or by hand. A critical shortcoming in this design is part interference. Microcomb teeth may fracture during assembly.

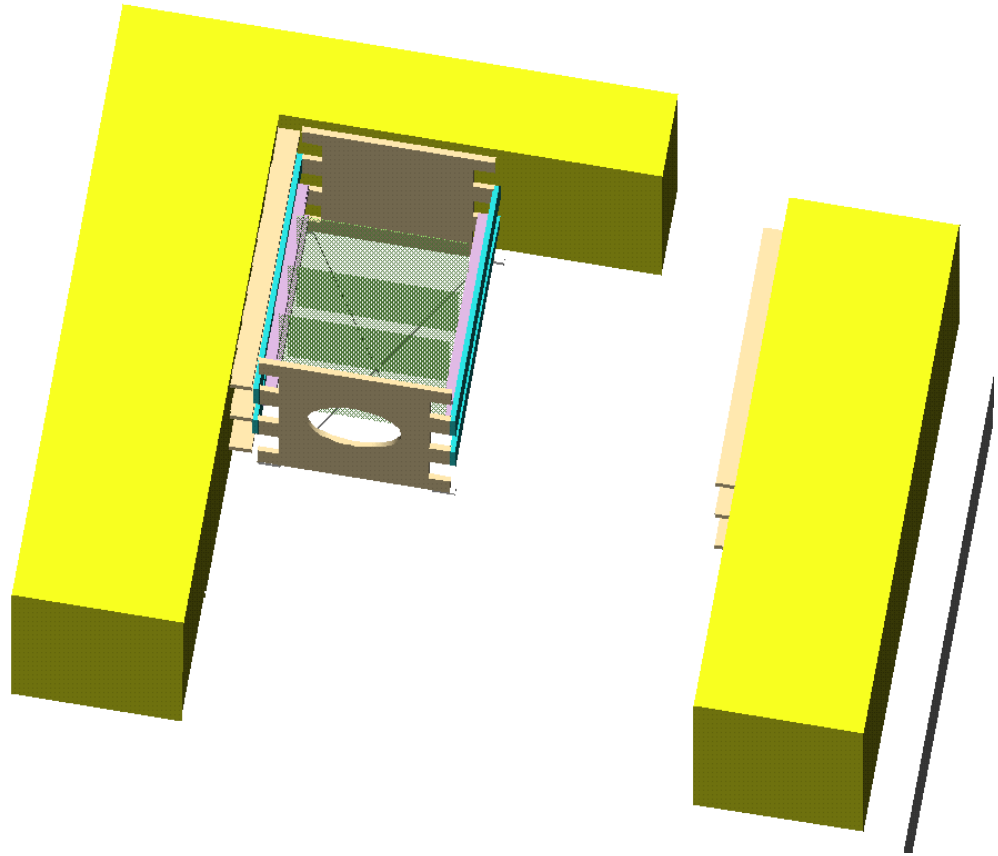


Figure B-4: In the “L-truss,” an air bearing table allows the flight module to be slid into place followed by the remaining half of the truss. Complexity and repeatability were key concerns.

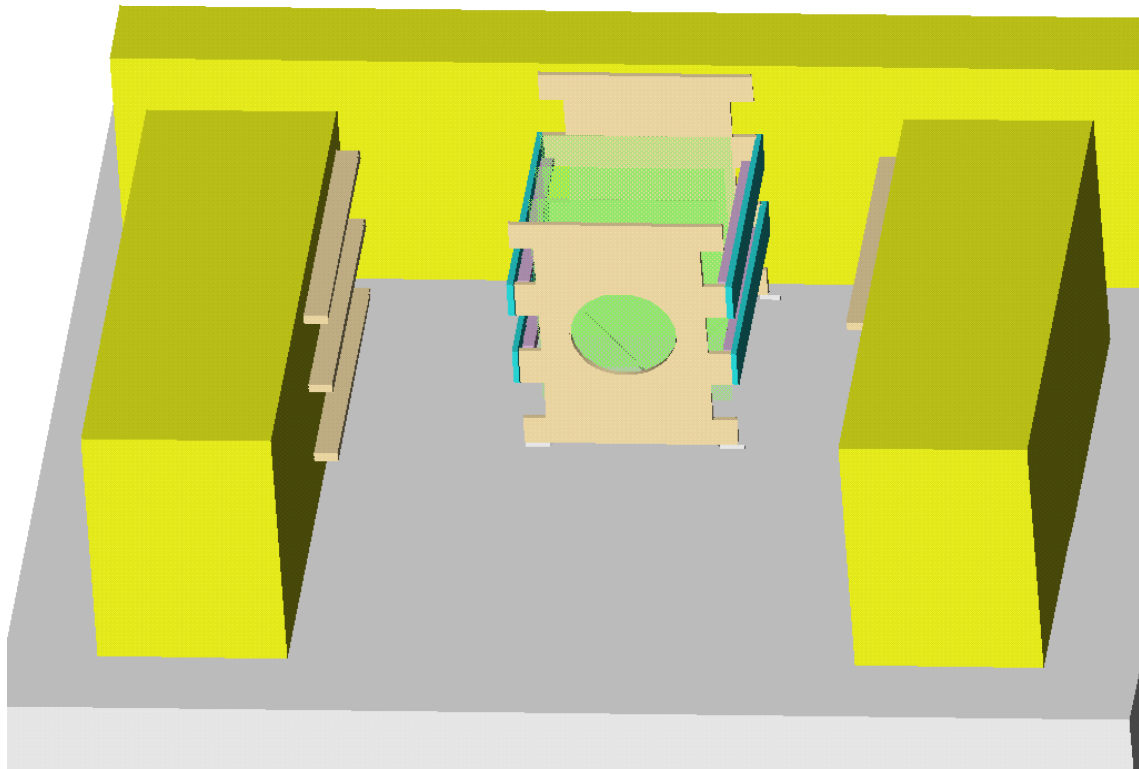


Figure B-5: The fixed reference flat acts as a surface from which the flight module and microcomb embedded walls are aligned. The flight module would be repeatably placed on kinematic couplings. Air bearings could provide a frictionless surface for sliding the walls with microcombs attached.

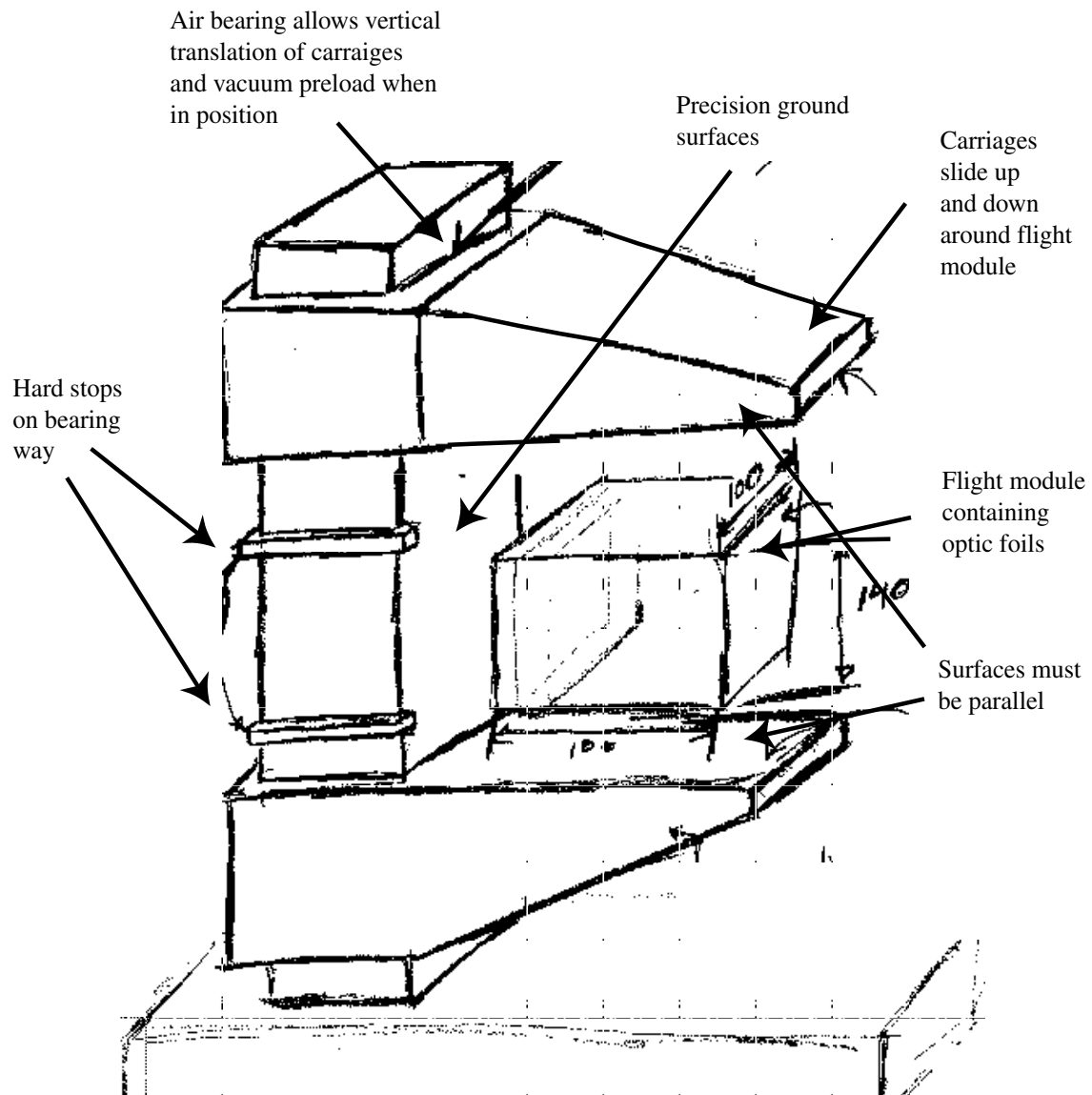


Figure B-6: The vertical air bearing concept repeatably places the microcombs with respect to the reference flat. The microcombs are glued to the carriages, which can then translate vertically or be locked in place with a vacuum preload on the bearings.

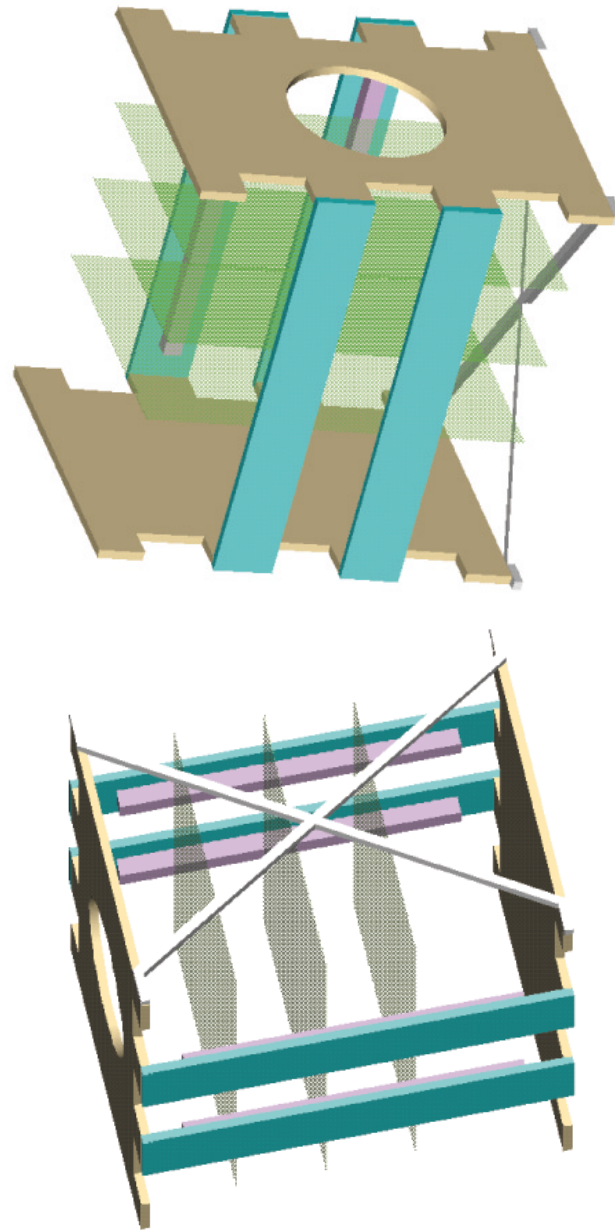


Figure B-7: An initial model of the flight module is shown from the side and top perspectives. Three optic foils are shown inserted. The flight module must allow measurement during assembly and permit the entrance and exit of x-rays during flight. Relatively low tolerances can be used since the assembly tool will do the high-accuracy alignment and the foils will then be fixed into place with an adhesive.

Appendix C

Assembly truss error budgets

Error budgets were useful in the concept design phase for choosing between competing designs and highlighting large error contributors. The detailed derivation of the error budget theory and preliminary error budget for the stack design is presented in Section 2.5.1 and Section 2.5.2, respectively. In this Appendix, we summarize the error budgets for the stack and air-bearing concepts, but spend the majority of time on the error budget for the final assembly truss design. This final design error budget is useful for predicting the assembly truss accuracy in aligning foils to the reference flat.

C.1 Preliminary error budgets for stack and air-bearing concepts

For the two conceptual designs, the derived angular and linear error contributions to the foil placement error for the structural loops are given in Figure C-1 and Figure C-2.

Lower left or right microcomb in Stack Design

Nominal coordinate totals	Sum Random Errors in the reference CS	RSS Random Errors in the reference CS	Average SUM & RSS random errors in the reference CS	Net Total Systematic Errors in the reference CS
X= 25.0000	X= 0.0436	X= 0.0431	X= 0.0434	X= 0.0000
Y= 120.0000	Y= 0.0021	Y= 0.0016	Y= 0.0019	Y= 0.0003
Z= -64.5000	Z= 0.0557	Z= 0.0556	Z= 0.0557	Z= 0.0000
	X (rad) = 0.0003	X (rad) = 0.0003	X (rad) = 0.0003	X (rad) = 0.0000
	Y (rad) = 0.0006	Y (rad) = 0.0005	Y (rad) = 0.0006	Y (rad) = 0.0000
	Z (rad) = 0.0006	Z (rad) = 0.0005	Z (rad) = 0.0006	Z (rad) = 0.0000

Enter numbers in BOLD Output is in RED

Number, N, of coordinate systems (not including the reference system) MAXIMUM OF 15	Systematic errors	
	systematic	dynamic
2	on	off

Dimensions are in mm

enter names of systematic errors for all axes

random errors are not signed, bidirectional and add as absolute values
systematic errors are signed and unidirectional

CS#	Description:	Actual dimensions	Random errors	systematic	thermal	dynamic	Error descriptions
2	All errors for this axis on/off					on	
X		0	0.0005	0.0000	0.0000	dynamic	
Y		120	0.0006	0.0000	0.0000	dynamic	waviness of the microcomb, thickness variation known to be .5um (manufacturer spec)
Z		5.5	0.00003	0.0000	0.0000	dynamic	Based on microcomb being manufactured with an error of +/- 0.5 mm/100mm+0.0 um Hertz for t
X (rad)		0	0.0000	0.0000	0.0000	dynamic	Based on microcomb being manufactured with an error of +/- 0.5 m/100mm
Y (rad)		0	0.0005	0.0000	0.0000	dynamic	accounted for in the mems manu tolerances
Z (rad)		0	0.0005	0.0000	0.0000	dynamic	due to wafer bow, the comb is curled 5um over 10mm

CS#	Description:	Actual dimensions	Random errors	systematic	thermal	dynamic	Error descriptions
1	All errors for this axis on/off					on	
X		25	0.0254	0.0000	0.0000	dynamic	based on milling machine tolerances (this estimate was later found to be a large underestimate)
Y		0	0.0001	0.0003	0.0000	dynamic	assumption that the plate is flat to 0.1um (Sun) + hertz deformation =0.3um
Z		-70	0.0254	0.0000	0.0000	dynamic	based on milling machine tolerances
X (rad)		0	0.0003	0.0000	0.0000	dynamic	RSS of machine tol prpndrcity of support bar to base (sin-1 of (.025/120mm) , 1:10000 for comb
Y (rad)		0	0.0001	0.0000	0.0000	dynamic	RSS of machine tol 1:10000 two times
Z (rad)		0	0.0001	0.0000	0.0000	dynamic	RSS of machine tol 1:10000 two times

Figure C-1: Preliminary error budget for the stack concept. The average sum and RSS random errors are 1.9 μm and the net total systematic errors are 0.3 μm.

Lower left or right microcomb in airbearing Design

Nominal coordinate totals	Sum Random Errors in the reference CS	RSS Random Errors in the reference CS	Average SUM & RSS random errors in the reference CS	Net Total Systematic Errors in the reference CS
X= 25.0000	X= 0.0384	X= 0.0380	X= 0.0382	X= 0.0000
Y= 120.0000	Y= 0.0020	Y= 0.0015	Y= 0.0018	Y= 0.0000
Z= -64.5000	Z= 0.0531	Z= 0.0531	Z= 0.0531	Z= 0.0000
	X (rad) = 0.0002	X (rad) = 0.0002	X (rad) = 0.0002	X (rad) = 0.0000
	Y (rad) = 0.0006	Y (rad) = 0.0005	Y (rad) = 0.0006	Y (rad) = 0.0000
	Z (rad) = 0.0006	Z (rad) = 0.0005	Z (rad) = 0.0006	Z (rad) = 0.0000

Enter numbers in BOLD Output is in RED

Number, N, of coordinate systems (not including the reference system) MAXIMUM OF 15

Systematic errors	Systematic errors	
	systematic	dynamic
	on	off

Dimensions are in mm

enter names of systematic errors for all axes

random errors are not signed, bidirectional and add as absolute values
systematic errors are signed and unidirectional

CS#	Description:	Actual dimensions	Random errors	systematic	thermal	dynamic	Error descriptions
2	All errors for this axis on/off						
	Contact point btwn comb and foil						
X		0	0.0005	0.0000	0.0000	0.0000	waviness of the microcomb, thickness variation known to be .5um (manufacturer spec)
Y		120	0.0006	0.0000	0.0000	0.0000	Based on microcomb being manufactured with an error of +/- 0.5 mm/100mm
Z		5.5	0.00003	0.0000	0.0000	0.0000	Based on microcomb being manufactured with an error of +/- 0.5 m/100mm
X (rad)		0	0.0000	0.0000	0.0000	0.0000	accounted for in the mems manu tolerances
Y (rad)		0	0.0005	0.0000	0.0000	0.0000	due to wafer bow, the comb is curled 5um over 10mm
Z (rad)		0	0.0005	0.0000	0.0000	0.0000	due to wafer bow, the comb is curled 5um over 10mm

CS#	Description:	Actual dimensions	Random errors	systematic	thermal	dynamic	Error descriptions
1	All errors for this axis on/off						
	Contact point btwn comb and reference flat						
X		25	0.0254	0.0000	0.0000	0.0000	based on milling machine tolerances (this estimate was later found to be a large underestimate)
Y		0	0.0001	0.0000	0.0000	0.0000	assumption that the plate is flat to 0.1um (yanxia)
Z		-70	0.0254	0.0000	0.0000	0.0000	based on milling machine tolerances
X (rad)		0	0.0002	0.0000	0.0000	0.0000	RSS of machine tol prpndrcity of support bar to base (sin-1 of (.025/120mm) , 1:10000 for comb
Y (rad)		0	0.0001	0.0000	0.0000	0.0000	based on error of 1:10000
Z (rad)		0	0.0001	0.0000	0.0000	0.0000	based on error of 1:10000

Figure C-2: Preliminary error budget for the air-bearing concept. The average sum and RSS random errors are 1.8 μm and the net total systematic errors are 0.0 μm .

C.2 Final design error budget

The final error budget for the assembly truss was evaluated to keep track of errors in individual parts in order to estimate the overall accuracy of the system. Similar to the approach taken to calculate the preliminary error budget in Section 2.5.2, we again consider the angular and linear errors for successive coordinate systems. A cross section of the final design revealing the structural loop and coordinate systems in 2-D is shown in Figure C-3. In this work, only the path from the reference frame to CS_2 is shown, since the other structural loop segments leading to other comb/foil contact points from the reference frame are nearly identical.

First, we estimate the three random translational and angular errors for CS_1 and tabulate its geometric location to the reference coordinate system. The translational errors are shown in Table C.1 and the angular errors are in Table C.2. A description of each error source is included in the table. The systematic error for this coordinate system occurs only in the Y direction as before. Description of this error is given on page 59.

Next, the errors at CS_2 are shown in Table C.3. The systematic error in CS_2 is described on page 61. The data from these three tables was inserted into the error propagation spreadsheets as before, shown in Figure C-4. From this figure, the expected accuracy of the assembly truss alignment is $0.5 \mu\text{m}$, assuming that systematic error can be recorded and compensated. The errors are nearly identical in the three microcombs due to the symmetric structure of the assembly truss.

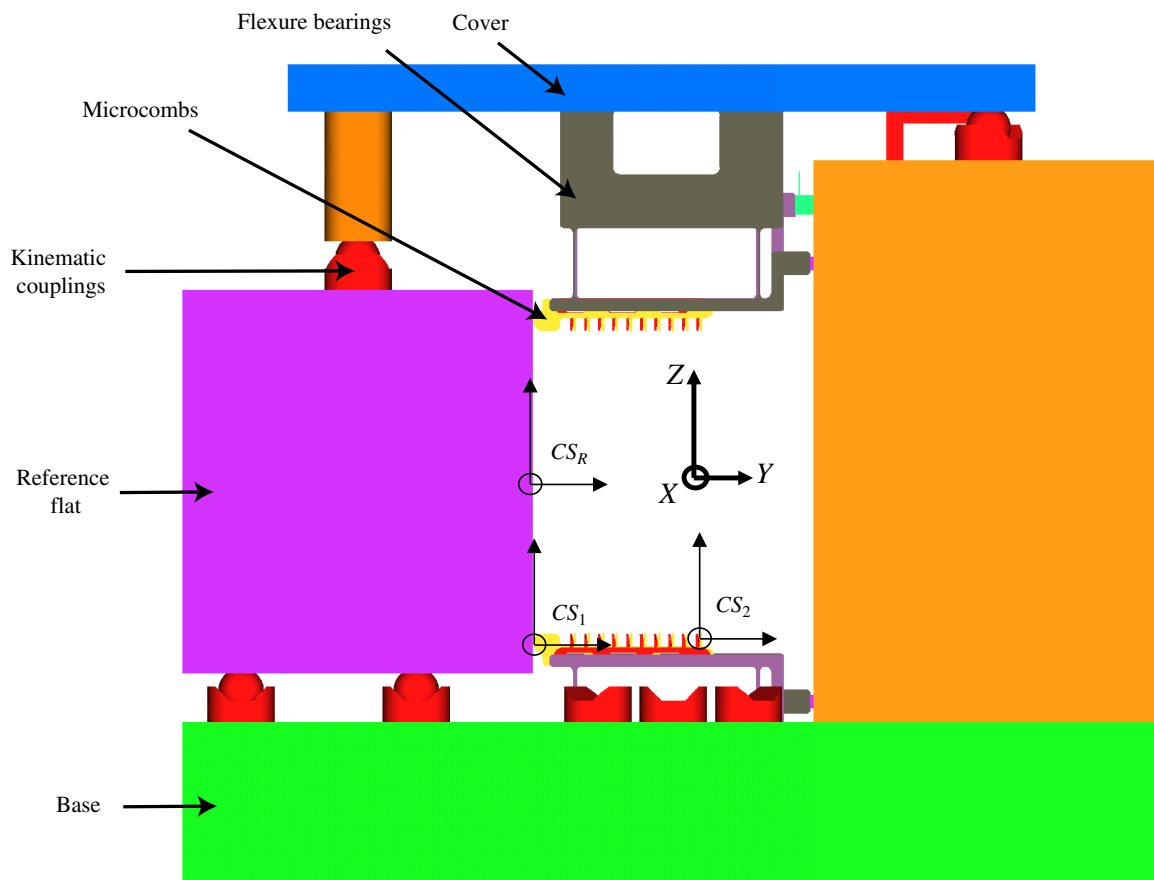


Figure C-3: Side view of the final assembly truss design with coordinate systems for error budgeting labeled. As before, the reference coordinate system is at the center of the reference flat face, CS_1 is located at the comb/flat interface, and CS_2 is located at the contact point between the reference comb and the optic foil.

Axes	Actual Dimensions	Random errors	Error description (Root-sum-square listed items)
X(mm)	28	0.0381	<ul style="list-style-type: none"> -Hole placement accuracy for kinematic coupling on bottom surface of reference flat = 0.0254 mm/2 -Hole placement accuracy on flexure bearings = 0.0254 mm -Thickness variation in milled flexure bearing = 0.0254 mm
Y(mm)	0	0.0010	<ul style="list-style-type: none"> -Flatness of reference flat = 0.001 mm (error by vendor in polishing, requested 0.0001 mm) -Deformation of reference flat due to compression forces from cover (FEA simulation results) = 0.000035 mm
Z(mm)	-74	0.0571	<ul style="list-style-type: none"> -Variation in height of kinematic couplings = 0.0254 mm -Tolerance between top of base and milled pocket in base for flexure mounting = 0.0254 mm -Height variation in milled flexure bearing = 0.0254 mm -Error in placement of microcomb on flexure bearing = 0.0254 mm

Table C.1: Random translational errors in the final assembly truss CS_1 . Multiple error sources have been root-sum-squared to get the random error contribution.

Axes	Actual Dimensions	Random errors	Error description (Root-sum-square listed items)
$\theta_X(\text{rad})$	0	0.0004	<ul style="list-style-type: none"> -Perpendicularity of the reference flat to its bottom = 1/10000 -Pitch error of the flexure bearings when combs are in contact with flat = 1×10^{-7} -Error due to kinematic coupling height (computed from kinematic coupling analysis spreadsheet [17]) = 0.000184 -Flatness of the top of the base = 1/10000 -Parallelism between top of base and milled pocket in base for flexure mounting = 1/100000 -Flatness of flexure bearing = 0.0254 mm/98 mm = 2.59×10^{-4} -Error in placement of microcomb on flexure bearing = 1/10000
$\theta_Y(\text{rad})$	0	0.0040	<ul style="list-style-type: none"> -Flatness of the top of the base = 1/10000 -Parallelism between top of base and milled pocket in base for flexure mounting = 1/100000 -Flatness of flexure bearing = 0.0254 mm/6.35 mm = 0.004
$\theta_Z(\text{rad})$	0	0.0010	<ul style="list-style-type: none"> -Hole placement accuracy on flexure bearings = 0.0254/26 = 0.0010 mm

Table C.2: Random angular errors in the final assembly truss CS_1 . Multiple error sources have been root-sum-squared to get the random error contribution.

Axes	Actual Dimensions	Random errors	Error description (Root-sum-square listed items)
$X(\text{mm})$	0	0.0005	–Variation in thickness of microcomb. The manufacturer specification for the wafer thickness is $475 \pm 0.25 \mu\text{m}$
$Y(\text{mm})$	70	0.0004	–Tolerances on microcomb manufacturing estimated to be $0.5 \mu\text{m}$ per 100mm of length. The microcomb length to be used is 70 mm. –Variation in Hertz contact deformation estimate = 0.0002
$Z(\text{mm})$	0	0	The microcomb manufacturing tolerances of $0.5 \mu\text{m}$ per 100mm of length are applicable. However, the contact point between the flat/comb is collinear with the contact point between the comb/foil, so this effect is negated.
$\theta_X(\text{rad})$	0	0.0000	Microcomb angular errors in this direction are accounted for in the Z direction manufacturing tolerances.
$\theta_Y(\text{rad})$	0	0.0005	Microcomb intrinsic angular errors would be caused by wafer bow that causes a curling of the final combs. The worst wafer flatness measured using a Hartmann metrology tool was $5 \mu\text{m}$ over the its length a 10 mm half period. The angular error is therefore $\left(\frac{5 \times 10^{-3}}{10}\right)$.
$\theta_Z(\text{rad})$	0	0.0005	Same description as $\theta_{Y\text{random}}$

Table C.3: Random translational and angular errors in the final assembly truss CS_2 . Multiple error sources have been root-sum-squared to get the random error contribution.

Left Lower Microcomb, Final Design

Nominal coordinate totals X= 28.0000 Y= 70.0000 Z= -74.0000	Sum Random Errors in the reference CS X= 0.1072 Y= 0.0006 Z= 0.0761 X (rad) = 0.0004 Y (rad) = 0.0045 Z (rad) = 0.0015	RSS Random Errors in the reference CS X= 0.1067 Y= 0.0004 Z= 0.0761 X (rad) = 0.0004 Y (rad) = 0.0040 Z (rad) = 0.0011	Average SUM & RSS random errors in the reference CS X= 0.1070 Y= 0.0005 Z= 0.0761 X (rad) = 0.0004 Y (rad) = 0.0043 Z (rad) = 0.0013	Net Total Systematic Errors in the reference CS X= 0.0000 Y= 0.0003 Z= 0.0000 X (rad) = 0.0000 Y (rad) = 0.0000 Z (rad) = 0.0000
---	--	--	--	--

Enter numbers in BOLD Output is in RED

Number, N, of coordinate systems (not including the reference system) MAXIMUM OF 15	Systematic errors
2	thermal dynamic
	on off

Dimensions are in mm
enter names of systematic errors for all axes

random errors are not signed, bidirectional and add as absolute values
systematic errors are signed and unidirectional

CS #	Description:	Actual dimensions	Random errors	systematic	thermal	dynamic	Error descriptions
2	All errors for this axis on/off						
	Contact point btwn comb and foil						
X	0	0.0005	0.0000	0.0000	0.0000	0.0000	
Y	70	0.0004	0.0000	0.0000	0.0000	0.0000	
Z	0	0.0000	0.0000	0.0000	0.0000	0.0000	
X (rad)	0	0.0000	0.0000	0.0000	0.0000	0.0000	
Y (rad)	0	0.0005	0.0000	0.0000	0.0000	0.0000	
Z (rad)	0	0.0005	0.0000	0.0000	0.0000	0.0000	

CS #	Description:	Actual dimensions	Random errors	systematic	thermal	dynamic	Error descriptions
1	All errors for this axis on/off						
	Contact point btwn comb and reference flat						
X	28	0.0381	0.0000	0.0000	0.0000	0.0000	
Y	0	0.0001	0.0003	0.0000	0.0000	0.0000	
Z	-74	0.0508	0.0000	0.0000	0.0000	0.0000	
X (rad)	0	0.0004	0.0000	0.0000	0.0000	0.0000	
Y (rad)	0	0.0040	0.0000	0.0000	0.0000	0.0000	
Z (rad)	0	0.0010	0.0000	0.0000	0.0000	0.0000	

Figure C-4: Final error budget for the assembly truss. The average sum and RSS random errors are 0.5 μm and the net total systematic errors are 0.3 μm .

Appendix D

Force sensor calibration curves

The linear correlation between force and voltage was measured using known force standards for two different force sensors (Honeywell, sold by Cooper Instruments, model LPM 560, LPM 562). The results are plotted in Figure D-1. These calibration lines permitted measurement of force data in the assembly truss from the sensor voltage output.

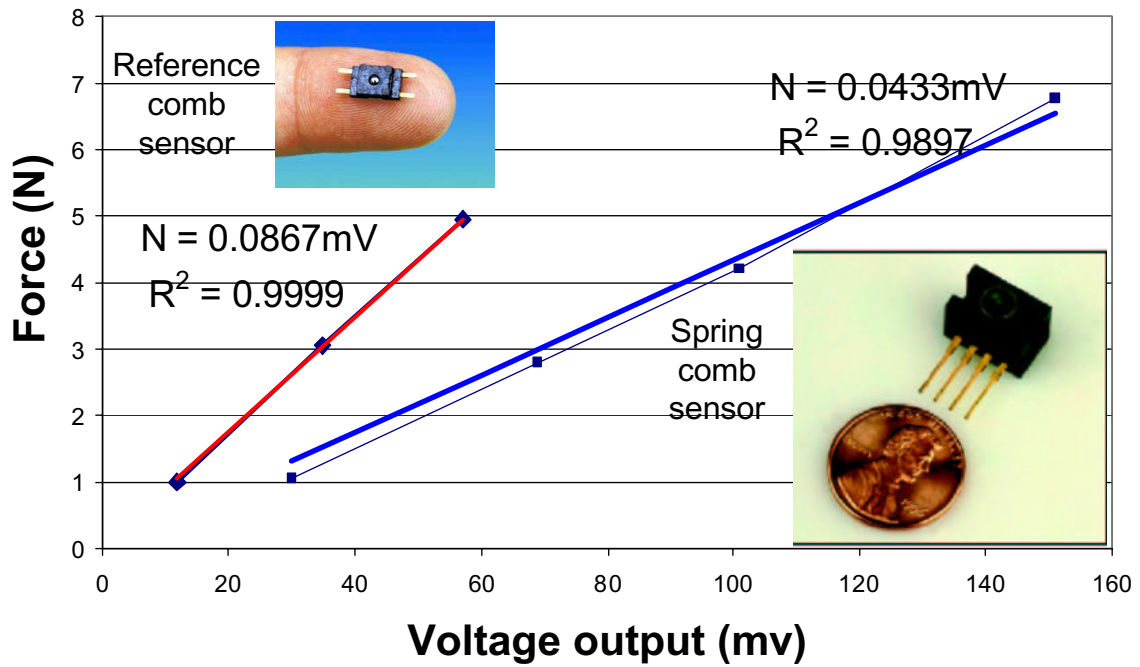


Figure D-1: Force sensor calibration data is shown along with sensor photographs. Linear regression fits were performed for each sensor to extract the proportionality value. Statistically, the high R^2 values indicate that the proportionality value is constant over the range.

Bibliography

- [1] O. Mongrard. High accuracy foil optics for x-ray astronomy. Master's thesis, Massachusetts Institute of Technology, Department of Aeronautics and Astronautics, September 2001.

- [2] C. G. Chen. Microcomb fabrication for high accuracy foil x-ray telescope assembly and vector gaussian beam modeling. Master's thesis, Massachusetts Institute of Technology, Department of Electrical Engineering and Computer Science, September 2000.

- [3] J. L. Culhane. X-ray astronomy in the future. In *Proc. XV ESLAB symposium*, 1981.

- [4] R. Giacconi. *X-ray astronomy beyond AXAF and XMM*, pages 15–38. Imaging X-ray Astronomy. 1990.

- [5] A. Franke. *Fabrication of extremely smooth nanostructures using anisotropic etching*. PhD dissertation, Massachusetts Institute of Technology, Department of Electrical Engineering and Computer Science, May 1997.

- [6] C. H. Chang, J. Carter, E. Murphy, M. L. Schattenburg, T. C. Bailey, R. D. Frankel, and R. Voisin. Fabrication of saw-tooth diffraction gratings using nanoimprint lithography. In *47th International Conference on Electron, Ion and Photon Beam Technology and Nanofabrication*, May 2003.

- [7] C. G. Chen, R. K. Heilmann, P. T. Konkola, O. Mongrard, G. P. Monnelly, and M. L. Schattenburg. Microcomb design and fabrication for high accuracy optical assembly. *J. Vac. Sci. Technol. B*, 18:3272–3276, 2000.
- [8] K. T. Turner and S. M. Spearing. Modeling of direct wafer bonding: Effect of wafer bow and etch patterns. *J. Applied Physics*, 92(12):7658–7666, 2002.
- [9] SCHOTT Corporation. 3 Odell Plaza, Yonkers, NY 10701 USA.
- [10] R. K. Heilmann, G. P. Monnelly, O. Mongrard, N. Butler, C. G. Chen, L. M. Cohen, C. C. Cook, L. M. Goldman, P. T. Konkola, M. McGuirk, G. R. Ricker, and M. L. Schattenburg. Novel methods for shaping thin-foil optics for x-ray astronomy. In *Proc. SPIE*, number 4496, pages 62–72, 2002.
- [11] C. R. Forest, M. L. Schattenburg, C. G. Chen, R. K. Heilmann, P. Konkola, J. Przbylowski, Y. Sun, J. You, S. M. Kahn, and D. Golini. Precision shaping, assembly and metrology of foil optics for x-ray reflection gratings. In *Proc. SPIE*, number 4851, 2002.
- [12] J. C. Greenwood. Silicon in mechanical sensors. *J. Phys. E, Sci. Instrum.*, 21:1114–1128, 1988.
- [13] G. P. Monnelly, O. Mongrard, D. Breslau, N. Butler, C. G. Chen, L. Cohen, W. Gu, R. K. Heilmann, P. T. Konkola, G. R. Ricker, and M. L. Schattenburg. High-accuracy x-ray foil optic assembly. In *Proc. SPIE*, number 4138, pages 164–173, San Diego, July 2000.
- [14] NASA Goddard Space Flight Center. Fall 2001. Personal communication: M.L. Schattenburg.
- [15] Y. Sun, C. R. Forest, M. J. Spenko, R. K. Heilmann, C. G. Chen, and M. L. Schattenburg. Precision microcomb design and fabrication for constellation-x soft x-ray telescope segmented optic assembly. In *17th Annual Meeting of the American Society of Precision Engineering*, October 2002.

- [16] Y. Sun, R. K. Heilmann, C. G. Chen, M. J. Spenko, C. R. Forest, and M. L. Schattenburg. Precision microcomb design and fabrication for x-ray optics. In *47th International Conference on Electron, Ion and Photon Beam Technology and Nanofabrication*, May 2003.
- [17] A. H. Slocum. *Precision Machine Design*. Society of Manufacturing Engineers, originally published by Prentice-Hall, Dearborn, Michigan, 1992.
- [18] R. Donaldson. Error budgets. In Robert J. Hocken, editor, *Technology of Machine Tools*, number 5 in Machine Tool Accuracy. Machine Tool Task Force.
- [19] A. H. Slocum. Error gain spreadsheet resource for machine tool design. <http://pergatory.mit.edu/2.75/>.
- [20] R. Cortesi. An easy to manufacture non-contact precision linear motion system and its applications. Master's thesis, Massachusetts Institute of Technology, Department of Mechanical Engineering, August 2000.
- [21] M. L. Culpepper, A. H. Slocum, and F. Z. Shaikh. Compliant kinematic couplings for use in manufacturing and assembly. In *International Mechanical Engineering Congress and Exposition*, Anaheim, CA, November 1998.
- [22] Y. Muranaka, M. Inaba, T. Asano, and E. Furukawa. Parasitic rotations in parallel spring movements. *Int. J. Japan Society of Precision Engineering*, 25(3):208–213, September 1991.
- [23] M. Madou. *Fundamentals of Microfabrication*. CRC Press, Boca Raton, Florida, 1997.
- [24] N. E. Dowling. *Mechanical Behavior of Materials*. Prentice-Hall, Upper Saddle River, New Jersey, 1999.
- [25] O. Mongrard, N. Butler, C. G. Chen, R. K. Heilmann, P. T. Konkola, M. McQuirk, G. P. Monnelly, G. S. Pati, G. R. Ricker, M. L. Schattenburg, and L. M. Cohen. High precision assembly and metrology of x-ray foil optics. In

16th Annual Meeting of the American Society of Precision Engineering, Crystal City, Virginia, November 2001.

- [26] J. E. Greivenkamp, D. G. Smith, R. O. Gappinger, and G. A. Williby. Optical testing using Shack-Hartmann wavefront sensors. In *Proc. SPIE*, number 4416, pages 260–263, Boston, 2001.
- [27] ADE Phase-Shift. 3470 E. Universal Way, Tucson, AZ 85706 USA.
- [28] J. Schwider. White-light fizeau interferometer. *Applied Optics*, 36(7):1433–1437, March 1997.
- [29] K. Takada, I. Yokohama, K. Chida, and J. Noda. New measurement system for fault location in optical waveguide devices based on an interferometric technique. *Applied Optics*, 26:1603–1606, 1987.
- [30] C. Hitzenberger. Measurement of cornea thickness by low-coherence interferometry. *Applied Optics*, 31:6637–6642, 1992.
- [31] R. Dandliker, E. Zimmermann, and G. Frosio. Electronically scanned white-light interferometry: a novel noise-resistant signal processing. *Opt. Lett.*, 17:679–681, 1992.
- [32] K. Okada and J. Tsujiuchi. Wavelength scanning interferometry for the measurement of both surface shapes and refractive index inhomogeneity. In *Proc. SPIE*, number 1162, pages 395–401, 1989.
- [33] K. Okada, H. Sakuta, T. Ose, and J. Tsujiuchi. Separate measurements of surface shapes and refractive index inhomogeneity of an optical element using tunable-source phase shifting interferometry. *Applied Optics*, 29:3280–3285, 1990.
- [34] P. de Groot. Measurement of transparent plates with wavelength-tuned phase-shifting interferometry. *Applied Optics*, 39(16):2658–2663, June 2000.
- [35] P. de Groot, R. Smythe, and L. Deck. Laser diodes map surface flatness of complex parts. *Laser Focus World*, pages 95–98, February 1994.

- [36] C. J. Evans, R. E. Parks, L. Z. Shao, T. Schmitz, and A. Davies. Interferometric testing of photomask substrate flatness. In *Proc. SPIE*, number 4344, pages 844–851, 2001.
- [37] P. G. Dewa and A. W. Kulawiec. Grazing incidence interferometry for measuring transparent plane-parallel plates. U.S. patent 5,923,425, July 1999.
- [38] P. de Groot, L. Deck, and X. Colonna de Lega. Adjustable coherence depth in a geometrically-desensitized interferometer. In *Proc. SPIE*, number 3479, pages 14–23, San Diego, July 1998.
- [39] P. de Groot. Grating interferometer for metrology of transparent flats. *Optical Fabrication and Testing*, 6:28–30, 1996. OSA Technical Digest Series Optical Society of America, Washington, D.C., 1996.
- [40] C. Ai. Multimode laser fizeau interferometer for measuring the surface of a thin transparent plate. *Applied Optics*, 36(31):8135–8138, November 1997.
- [41] G. Schulz. Zweistrahlinterferenz in planspiegelanordnungen. *Opt. Acta*, 11:43–60, 89–99, 131–143, 1964.
- [42] L. Deck. Multiple surface phase shifting interferometry. In *Proc. SPIE*, number 4451, pages 424–431, 2001.
- [43] B. C. Platt and R. Shack. History and principles of Shack-Hartmann wavefront sensing. *Journal of Refractive Surgery*, 17:573–577, 2001.
- [44] J. A. Koch, R. W. Presta, R. A. Sacks, R. A. Zacharias, E. S. Bliss, M. J. Daily, M. Feldman, A. A. Grey, F. R. Holdener, J. T. Salmon, L. G. Seppala, J. S. Toeppen, L. V. Atta, B. M. Van Wouterghem, W. T. Whistler, S. E. Winters, and B. W. Woods. Experimental comparison of a Shack-Hartmann sensor and a phase-shifting interferometer for large-optics metrology applications. *Applied Optics*, 39(25):4540–4546, September 2000.
- [45] D. Malacara. *Optical Shop Testing*. Wiley, New York, second edition, 1992.

- [46] C. Koliopolis. Simultaneous phase shift interferometer. In *Proc. SPIE*, number 1531, pages 119–127, 1991.
- [47] B. M. Welsh, B. L. Ellerbroek, M. C. Roggemann, and T. L. Pennington. Fundamental performance comparison of a Hartmann and a shearing interferometer wavefront sensor. *Applied Optics*, 34:4186–4195, 1995.
- [48] Oriel Instruments, 150 Long Beach Blvd., Stratford, CT 06615 USA. *The Book of Photon Tools*, 2001.
- [49] Acton Research Corporation. 15 Discovery Way, Acton, MA 01720 USA.
- [50] Omega Optical, Inc. 210 Main Street, Brattleboro, VT 05301 USA.
- [51] Seishin Trading Co., LTD. 2-1, 1-chome Sannomiya-cho, Chuo-ku, Kobe, 650-0021 Japan.
- [52] OptoSigma. 2001 Deere Avenue, Santa Ana, California 92705 USA.
- [53] Space Optics Research Labs. 7 Stuart Road, Chelmsford, MA 01824 USA.
- [54] Web Elements. Silicon properties. <http://www.webelements.com/>.
- [55] Lambda Research Optics, Inc. 1695 W. MacArthur Blvd., Costa Mesa, CA 92626 USA.
- [56] JML Optical Industries, Inc. 690 Portland Avenue, Rochester, NY 14621 USA.
- [57] WaveFront Sciences, Inc. 14810 Central Ave. SE, Albuquerque, New Mexico 87123-3905 USA.
- [58] Spectral Instruments. 420 North Bonita Avenue, Tucson, Arizona 85745 USA.
- [59] A. H. Slocum. Topic 3 fundamental principles. 2.007 Class Notes, September 2001.
- [60] Technical Manufacturing Corporation (TMC). *Resource Guide 2002*, 2002.

- [61] P. T. Konkola. *Design and analysis of a Scanning Beam Interference Lithography system for patterning gratings with nanometer-level distortions*. PhD dissertation, Massachusetts Institute of Technology, Department of Mechanical Engineering, May 2003.